Delft University of Technology

Spin dynamics with the interplay of elasticity and radiation in hybrid systems

Zhang, Xiang

Important note
To cite this publication, please use the final published version (if applicable).
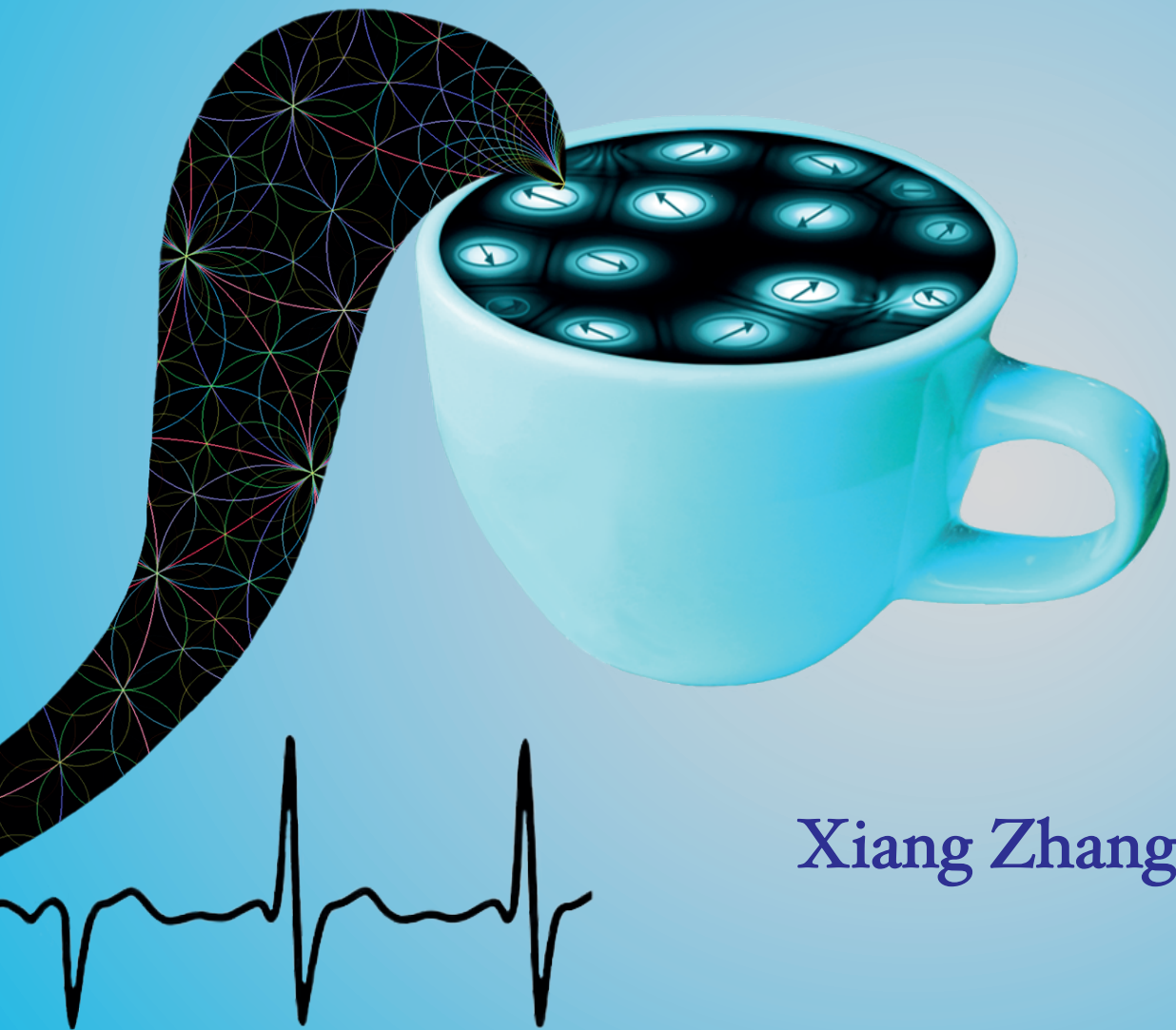Please check the document version above.

Spin dynamics with the interplay of elasticity and radiation in hybrid systems

Xiang Zhang

Spin dynamics with the interplay of elasticity and radiation in hybrid systems

Spin dynamics with the interplay of elasticity and radiation in hybrid systems

Proefschrift

door

Xiang ZHANG

Master of Science in Physics,
Katholieke Universiteit Leuven, België,
geboren te Poyang, China.

Dit proefschrift is goedgekeurd door de

promotor: Prof.dr. Y.M. Blanter
copromotor: Dr. M. Blaauboer

Samenstelling promotiecommissie:

Rector Magnificus,	voorzitter
Prof.dr. Y.M. Blanter	Technische Universiteit Delft, promoter
Dr. M. Blaauboer	Technische Universiteit Delft, copromoter

Onafhankelijke leden:

Prof.dr. G.A. Steele	Technische Universiteit Delft
Prof.dr. P.G. Steeneken	Technische Universiteit Delft
Dr. M.H. Ansari	Forschungszentrum Juelich and RWTH Aachen
Dr. M. Titov	Radboud University Nijmegen
Prof.dr. G.E.W. Bauer	TU Delft and Tohoku University

Dedicated to my grandpa Mr. Xiaoling Cheng,
and those who have helped me through all the way to the journey of physics.

Contents

List of Figures

Summary

Originated from the electron's intrinsic angular momentum, magnetism has endowed various manipulations in both macroscopic and microscopic setups with another degree of freedom. Beyond the traditionally developed usage such as storage and sensors, there are enormous applications based on engineering and integrating magnetism into heterostructures and their susceptibility to external stimuli. The emergent fields of nano-level spintronics and spin caloritronics with novel properties have been intensively studied both theoretically and experimentally. Within those developments, the interaction of atomic spins with electromagnetic waves (photons) and elastic dynamics (phonons) are of fundamental importance. This thesis is devoted to investigating the interplay of magnetism with electrodynamics and lattice elasticity in several hybrid systems.

In Chapter 2 I study the chiral pumping of surface acoustic wave (SAW) by the ferromagnetic resonance (FMR) of a yttrium iron garnet (YIG) nanowire mounted on top of an acoustic substrate. The linear magnetoelastic coupling for small perturbation has been utilized and the second quantization formalism has been developed. The magnetic dynamics in single nanowire pumps SAWs with opposite angular momenta into opposite directions, thus generates a phonon spin current. I further predict the two parallel nanowires forms a phononic cavity which at geometrical resonances pumps an unidirectional SAW into half of the surface plane.

While Chapter 2 studies the magnetically ordered state far below the critical temperature, Chapter 3 continues to discuss the magnetoelastic coupling but with the extension into a broader temperature range where the spin ordering breaks. I present a theoretical scheme of incorporating the exchange magnetoelastic interaction into the thermal elastic dynamics for thin membranes of 2D antiferromagnetic (AFM) material with restricted geometry. Here, I generalize the elastic Grüneisen relation into an effective version which includes the magnetic counterpart to the volume change of internal energy. Based on the specific heat and thermal conductivity from elastic and magnetic origins I demonstrate the temperature dependence for experimental observables over a wide range, even beyond the phase transition temperature. This model of analysis as been validated by applying it to the case of a $FePS_3$ flake resonator and the theoretical predictions fit well with the reported experiment data.

Chapter 4 and 5 turn to investigate the interaction of spins with the electromagnetic degree of freedom in waveguide and cavity setups. In Chapter 4 I discuss the inter-excitations between multiple millimeter-sized ferromagnetic spheres mediated by waveguide photons. By adjusting the position of the magnets in the waveguide, the magnon-photon coupling can be tuned to be chiral, i.e., magnons only couple with photons propagating in one direction, leading to an asymmetric transfer of angular momentum and energy between the magnets. I demonstrate for a chain consisting of a large number of magnetic spheres, the concentration of the magnon's population can be achieved at the chain edge and super/sub-radiant states can be realized for selected

waveguide photon frequencies.

In Chapter 5 I propose an optical method to manipulate the spin flipping process which serves as an energy exchange protocol between charging environment (cavity photons) and the storage element (an array of spins). This system is modeled by the Dicke Hamiltonian in which the collective spins dynamics can be interpreted into a harmonic oscillator-like behaviour. Compared to the separate charging protocol the collective spins flipping speed can be enhanced proportionally to the square root of the spin numbers. Unlike previous studies, I point out that such speedup effect does not originate from entanglement but is due to the coherent cooperative interactions among the spins.

Chiral couplings discussed in this thesis are based on the effect of spin-momentum locking. Although it emerges in selected modes of propagating photons in the waveguide shown in Chapter 4, it is difficult to excite an unidirectional acoustic wave for a single nanowire as in Chapter 2. Further design of sophisticated structures shall be considered for realizing the intrinsic chiral magnon-phonon interaction. Furthermore, the generic model of analysis for magnetism-based thermal dynamics of thin membranes developed in Chapter 3 can be extended to study other materials. Knowledge for the detailed lattice layout and anisotropy helps to improve the prediction accuracy. Focus on the speedup effect for the spin flip may also be incorporated into researching more complex models such as the one with superradiance. Overall, I hope the works presented in this thesis will motivate and serve as a foundation for future studies.

Samenvatting

Ontstaan uit het intrinsieke impulsmoment van het elektron, heeft magnetisme diverse manipulaties in zowel macroscopische als microscopische opstellingen van een extra graad van vrijheid voorzien. Naast de traditioneel ontwikkelde toepassingen zoals opslag en sensoren, zijn er enorme toepassingen op basis van engineering en integratie van magnetisme in heterostructuren en hun gevoeligheid voor externe stimuli. De opkomende gebieden van de spintronica op nanoniveau en de spin caloritronica met nieuwe eigenschappen zijn zowel theoretisch als experimenteel intensief bestudeerd. Binnen deze ontwikkelingen is de interactie van atomaire spins met elektromagnetische golven (fotonen) en elastische dynamica (fononen) van fundamenteel belang. Dit proefschrift is gewijd aan het onderzoeken van de wisselwerking van magnetisme met elektrodynamica en roosterelasticiteit in verschillende hybride systemen.

In hoofdstuk 2 bestudeer ik het chiraal pompen van oppervlakte akoestische golven (SAW) door de ferromagnetische resonantie (FMR) van een yttrium ijzer granaat (YIG) nanodraad gemonteerd bovenop een akoestisch substraat. De lineaire magnetoelastische koppeling voor kleine verstoringen is gebruikt en het tweede kwantiseringsformalisme is ontwikkeld. De magnetische dynamica in een enkele nanodraad pompt SAWs met tegengesteld impulsmoment in tegengestelde richtingen en genereert zo een fononspinstroom. Ik voorspel verder dat twee parallelle nanodraden een fononische holte vormen die bij geometrische resonanties een unidirectionele SAW in de helft van het oppervlaktevlak pompt.

Terwijl hoofdstuk 2 de magnetisch geordende toestand ver onder de kritische temperatuur bestudeert, gaat hoofdstuk 3 verder met de bespreking van de magnetoelastische koppeling, maar met de uitbreiding naar een breder temperatuurgebied waar de spinordening breekt. Ik presenteer een theoretisch schema om de magnetoelastische wisselwerking op te nemen in de thermo-elastische dynamica voor dunne membranen van 2D antiferromagnetisch (AFM) materiaal met beperkte geometrie. Hier veralgemeent ik de elastische Grüneisen relatie tot een effectieve versie die de magnetische tegenhanger van de volumeverandering van de inwendige energie omvat. Gebaseerd op de specifieke warmte en warmtegeleidingscoëfficiënt van elastische en magnetische oorsprong toon ik de temperatuurafhankelijkheid aan voor experimentele waarnemingen over een breed gebied, zelfs voorbij de faseovergangstemperatuur. Dit analysemodel is gevalideerd door het toe te passen op het geval van een FePS$_3$ flake resonator en de theoretische voorspellingen komen goed overeen met de gerapporteerde experimentele gegevens.

Hoofdstuk 4 en 5 onderzoeken de interactie van spins met de elektromagnetische vrijheidsgraad in golfgeleider- en holteopstellingen. In hoofdstuk 4 bespreek ik de interexcitaties tussen meerdere ferromagnetische bollen van millimetergrootte, gemedieerd door golfgeleiderfotonen. Door de positie van de magneten in de golfgeleider aan te passen, kan de koppeling tussen magnonen en fotonen chiraal worden ingesteld, d.w.z. dat

magnonen alleen koppelen met fotonen die zich in één richting voortplanten, wat leidt tot een asymmetrische overdracht van impulsmoment en energie tussen de magneten. Ik demonstreer voor een keten bestaande uit een groot aantal magnetische bollen, dat de concentratie van de magnonpopulatie kan worden bereikt aan de rand van de keten en dat super/sub-stralingstoestanden kunnen worden gerealiseerd voor geselecteerde golfgeleider fotonfrequenties.

In hoofdstuk 5 stel ik een optische methode voor om het spin flipping proces te manipuleren dat dient als een energie-uitwisselingsprotocol tussen de oplaadomgeving (holte fotonen) en het opslagelement (een array van spins). Dit systeem wordt gemodelleerd door de Dicke Hamiltoniaan waarin de dynamica van de collectieve spins kan worden geïnterpreteerd in een harmonische oscillator-achtig gedrag. Vergeleken met het afzonderlijke oplaadprotocol kan de flipsnelheid van de collectieve spins evenredig worden verhoogd met de vierkantswortel van het aantal spins. In tegenstelling tot eerdere studies, wijs ik erop dat een dergelijk versnellingseffect niet voortkomt uit verstrengeling, maar te wijten is aan de coherente coöperatieve interacties tussen de spins.

Chirale koppelingen die in dit proefschrift worden besproken zijn gebaseerd op het effect van spin-momentum locking. Hoewel dit effect optreedt in geselecteerde modi van voortplantende fotonen in de golfgeleider die in hoofdstuk 4 wordt getoond, is het moeilijk om een unidirectionele akoestische golf te exciteren voor een enkele nanodraad zoals in hoofdstuk 2. Verder ontwerp van verfijnde structuren zal worden overwogen voor het realiseren van de intrinsieke chirale magnon-fonon interactie. Verder kan het generieke analysemodel voor magnetisme-gebaseerde thermische dynamica van dunne membranen, ontwikkeld in Hoofdstuk 3, worden uitgebreid om andere materialen te bestuderen. Kennis voor de gedetailleerde rooster layout en anisotropie helpt om de nauwkeurigheid van de voorspelling te verbeteren. Focus op het versnellingseffect voor de spin flip kan ook worden meegenomen in het onderzoek naar complexere modellen, zoals die met superradiantie. Al met al hoop ik dat de in dit proefschrift gepresenteerde werken zullen motiveren en als basis zullen dienen voor toekomstige studies.

1

Introduction

道可道，非恒道；名可名，非恒名。
无，名天地之始；有，名万物之母。
故，常无，欲以观其妙；常有，欲以观其微。
此两者，同出而异名，同谓之玄。玄之又玄，众妙之门。

道德经

The Tao that can be told is not the Absolute Tao;
the existence that can be named is not Absolute Existence.
The nameless void is the origin of universe;
the named interaction is the mother of all particular things.
Therefore.
To the void, you feel the secret elegance;
to the ubiquitous interaction, you see various manifestations.
Yet secret and manifestations arise from the same source;
they may both be called the cosmic mystery.
Reaching from the mystery into the deeper mystery is the gate to the secret of all forms.

Tao Te Ching

1

1.1. Magnetism

The elementary quantity in solid-state magnetism is the magnetic moment $\boldsymbol{m}$. On an atomic scale, intrinsic magnetic moments are associated with the spin of each electron and a further contribution is associated with its orbital motion around the nucleus. The spin $\boldsymbol{S}$ and orbital moments $\boldsymbol{L}$ of the atomic electrons add in ways governed by the laws of quantum mechanics given the total spin $\boldsymbol{J} = \boldsymbol{S} + \boldsymbol{L}$. The proportionality between magnetic momentum and orbit angular momentum is given by the Bohr magneton μ_B such that $\boldsymbol{m} = -\mu_B \boldsymbol{L}$. However, for the electron spin momentum this proportionality reads $\boldsymbol{m} = -2\mu_B \boldsymbol{S}$ such that the proportionality associated with the total atomic spin is $\boldsymbol{m} = -g\mu_B \boldsymbol{J} \equiv -\gamma \boldsymbol{J}$ with the g-factor and γ (referred to the gyromagnetic ratio) varies for different materials [1, 2]. In some cutting-edge researches this g-factor can be even tuned by external gate controls and has application in spin-qubit manipulations [3]. For simplicity, in this thesis, the notation of S is used to replace J as the total spin momentum of magnetic atom.

Thus the local magnetic momentum $\boldsymbol{m}$ is a discrete quantity varying rapidly from atom to atom. But viewing in mesoscopically, it can be averaged over a distance of order of few nanometers and nanoseconds. The magnetization density of a solid $\boldsymbol{M}$, which is defined as

$$\boldsymbol{M} = \sum_{i=1}^{N} \boldsymbol{m_i} \tag{1.1}$$

with N the number of spins per unit volume, varies smoothly on a mesoscopic scale. This is the so-called continuous medium approximation. At temperatures above a certain critical value T_c, the ground state of local magnet $\boldsymbol{m}$ points to all the directions in real space, possessing the full symmetries of the Hamiltonian. Such high symmetry phase in magnetism is mentioned as the paramagnetic phase and the long-range (macroscopic) order parameter $\boldsymbol{M}$ which is the average of the fully-filled order space of $\boldsymbol{m}$ (Eq. 1.1) equals zero. Breaking from high symmetry phase into the low symmetry phase means the order space is partially filled and the accompanying establishment of order parameter [2, 4]. This is a fundamental phenomenon in condensed matter physics, and in the language of magnetism this means the transition from para-phase into ferro- or antiferro-phase in which the long-range order $\boldsymbol{M}$ or $\boldsymbol{L}$ acquires non-vanishing values. Thus the symmetry breaking goes along with the decrease of entropy and in the limiting case of the very low temperature the symmetry is broken into a single point in the order space. In ferromagnetism this means all the atomic spins point to the same direction and the magnet becomes saturated and rigid so that to be responsive to the external perturbations. Elementary excitation in rigidity is to excite the single point in order space to a limited range, such that the entropy increases from zero to a small amount. The excitation energy ω proportional to ΔS is low, and in the real space the order parameter varies slowly leading to the long wavelength modulation [5]. Specifically, the energy required for elementary excitations depends on the interactions between the participants. Needless to say the spin wave for magnetic rigidity and elastic wave for elastic rigidity depends on the lattice structures.

Based on the fact that macroscopical order parameter is nonzero in low symmetry phase and zero in the high symmetry phase, Landau suggested that the basic features
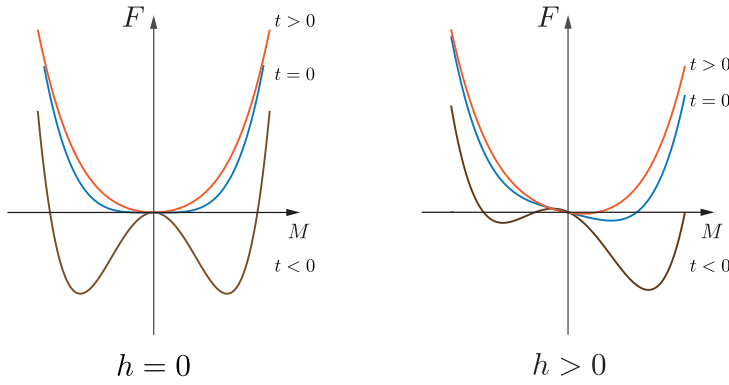
Figure 1.1: The plot of Landau free energy as function of order parameter M with or without the external field showing the spontaneous symmetry breaking as the temperature decreases blow the critical value T_c. Here $t = (T - T_c)/T_c$.

of the critical behavior near the transition for a given system may be determined by expanding its free energy in powers of these order parameters [2]. Since the magnetic phase transition is of second order, in the sense that the second derivative of the free energy is divergence while the first derivative is continuous at critical point, the Landau free energy near phase transition has the form [6]

$$F(T) = F_0(T) + a_0 t M^2 + b_0 M^4 - hM, \quad t = (T - T_c)/T_c \text{ and } |t| \ll 1. \tag{1.2}$$

Here h stands for the external field and parameters $a_0, b_0 > 0$, F_0 is the energy of non-magnetic parts. These coefficients (a_0, b_0, T_c) are determined by external observations so that Landau's expansion is a phenomenological theory. The plot of free energy as function of order parameter with or without the external field h is shown in Fig. 1.1. We see that indeed there is gradual emergence of spontaneous magnetization as $t < 0$ and the external field tilts the concave shape along with its direction. Through minimization of F one can derive the critical exponents of magnetization M and specific heat C_m by such a simple expansion expression. In spite of the success of Landau's theory, one should note that it is still a mean-field theory (or zero-order approximation) in which all spins are assumed to 'feel' an identical average molecular field and completely ignores the correlations and fluctuations. One obvious drawback is that as $T > T_c$ the long-range order $M = 0$ which leads to a vanishing magnetic energy and thus the specific heat collapses to zero just after the phase transition. For realistic materials this is not the case because the short-range order still persists in the system even above T_c which results in a non-vanishing energy and specific heat [7]. Thus in Chapter 3 when we study the heat conduction problem of 2D Ising material it is essential to apply the Onsager's result instead of the Landau's mean field approximation.

The energy for a ferro- or antiferro-magnetic body can be categorised into two parts [1, 2]. The first is the magnetostatic energy which involves the Zeeman term describing the interaction of the magnet with external magnetic field $\boldsymbol{H}_0$, as well as the self-energy for the interaction with the internal magnetic field generated by itself. The Zeeman energy

derived from the torque on magnet acquires the simple form

$$H_{zm} = -\mu_0 \boldsymbol{H}_0 \cdot \boldsymbol{M}, \tag{1.3}$$

with μ_0 is the vacuum permeability. Apart from H_0, the spins inside a magnet feel the dipolar field created by other spins (dipolar anisotropy) and also the demagnetizing field $\boldsymbol{H}_d$ which originates from the magnetic discontinuity on the body surface. The field $\boldsymbol{H}_d$ is opposite to $\boldsymbol{M}$ with phenomenological expression $\boldsymbol{H}_d = -\overleftrightarrow{\boldsymbol{N}}\boldsymbol{M}$, and in this sense the name 'demagnetizing'. Thus the demagnetization energy is

$$H_{dm} = \frac{1}{2}\mu_0 \sum_{ij} N_{ij} M_i M_j, \tag{1.4}$$

with the tensor element N_{ij} provided according to the body shape. The second part is the electrostatic energy including the exchange interaction and single-ion anisotropy. Written as the summation between neighbouring spins, the exchange Hamiltonian [8]

$$H_{ex} = -2J \sum_{\langle i,j \rangle} \boldsymbol{S}_i \cdot \boldsymbol{S}_j \tag{1.5}$$

is an effective Hamiltonian in that it uses the spin representation to effectively describe the Coulomb repulsion of two nearby electrons, sitting on neighbouring atoms. So the strength J is an effective parameter representing all the influences on orbital dimensions such as the external magnetic field, electric field, the distance between lattice sites, and etc. The tuning of J between coupled semiconductor quantum dots is the cutting-edge development in recent quantum gate mechanism [9, 10]. It can be proven that for $S = 1/2$ the two-spin's singlet and triplet states are eigenstates of the exchange Hamiltonian with eigenvalues $3J/2$ and $-J/2$ respectively. Thus the energy difference between the parallel and antiparallel state is $\epsilon_{\uparrow\uparrow} - \epsilon_{\uparrow\downarrow} = -J$. If $J > 0$ the state $\uparrow\uparrow$ is energetically favored leading to the ferromagnetism while as the opposite if $J < 0$ the state $\uparrow\downarrow$ is more preferred which shall result in antiferromagnetism.

The single-ion anisotropy originates from the electrostatic interaction between the orbit and crystalline field which tends to stabilize a particular orbit. Due to the spin-orbit coupling the magnetic moment is then inclined to a specific direction. In ferro- and antiferromagnetic crystals, the single-ion anisotropy and dipolar anisotropy are summed to produce a phenomenological energy term of various forms for different materials. For example in antiferromagnetic MnF2 the easy-axis anisotropy along the [001] direction is described by $H_{an} = -A\sum_i (S_i^z)^2$ [11] and for the RbMnF3 the anisotropy along [111] crystallographic axes is described by $H_{an} = -A\sum_i [(S_i^x)^2(S_i^y)^2 + c.p.]$ [12], with $c.p.$ denotes the cyclic permutation of indices (x, y, z). Overall, the general Hamiltonian for magnetism includes the above terms

$$H_m = H_{zm} + H_{ex} + H_{dm} + H_{an}, \tag{1.6}$$

and it is the exchange interaction as the main contribution which dominates various magnet properties. The anisotropy energy works as a bias term tuning the equilibrium magnetic direction and spin wave dispersion relations. Usually in bulk materials, the demagnetizing energy can be neglected and other contributions may be added according to specific considerations.

1.1.1. Macrospin precession and quantization

The equation of motion for magnetism can be obtained by simply considering the conservation of angular momentum, leading to the well known Landau-Lifshitz (LL) equation [13]

$$-\frac{1}{\gamma}\frac{d\boldsymbol{M}}{dt} = \mu_0\boldsymbol{M}\times\boldsymbol{H}_{eff}, \quad \gamma > 0, \tag{1.7}$$

with the effective field H_{eff} provided by the minus of derivative of the free energy in magnetism,

$$\mu_0 H_{eff} = -\frac{\partial F}{\partial \boldsymbol{M}}. \tag{1.8}$$

Thus various properties about magnetic precession can be derived by given the free energy expression. According to the previous analysis, the ferro- and antiferromagnetic free energy is dominated by the exchange interaction and accompanied by several bias terms. Expressed in the macroscopic magnetization $\boldsymbol{M}$, the exchange interaction (Eq. 1.5) leads to the energy density per unit volume

$$F_{ex} = -\frac{2J}{N\gamma^2}\boldsymbol{M}_i \cdot \sum_j \boldsymbol{M}_j, \tag{1.9}$$

and in the case of Kittel mode, i.e. all spins evolves simultaneously ($\boldsymbol{k} = 0$), it can be even simplified into the form

$$F_{ex} = -\frac{2Jz}{N\gamma^2}\boldsymbol{M_1}\cdot\boldsymbol{M_2} \equiv -\mu_0\frac{H_E}{M_s}\boldsymbol{M_1}\cdot\boldsymbol{M_2}, \tag{1.10}$$

in which the $\boldsymbol{M}_{1,2}$ stands for the uniform magnetizations in (sub) lattices of 1 and 2 respectively, and $M_s = N\gamma S$ is the saturated magnetization. The same applies for uniaxial anisotropy, for example, $H_{an} = -A\sum_i (S_i^z)^2$ rephrased as $H_{an} = -A/(N\gamma)^2\sum_i (M_i^z)^2$ leading to the energy density in Kittel mode

$$F_{an} = -\frac{A}{N\gamma^2}[(M_1^z)^2 + (M_2^z)^2] \equiv -\mu_0\frac{H_A}{2M_s}[(M_1^z)^2 + (M_2^z)^2]. \tag{1.11}$$

The effective exchange and anisotropy field in this example then becomes

$$H_E = \frac{2|J|zS}{\gamma\mu_0}, \quad H_A = \frac{2|A|S}{\gamma\mu_0}, \tag{1.12}$$

with direction oriented to the $\pm z$ axis for spin up and spin down respectively.

We solve the EOM for antiferromagnetism as an example to illustrate the general feature of magnetic precession. Departing the time-dependent varying part from the equilibrium constant, the magnetization can be written into $\boldsymbol{M}_1(t) = M_s\hat{z} + \boldsymbol{\xi}(t)$ and $\boldsymbol{M}_2(t) = -M_s\hat{z} + \boldsymbol{\eta}(t)$. The equations of motion are linearized by assuming small shear deviation, i.e. $\sqrt{|\boldsymbol{\xi}|^2 + |\boldsymbol{\eta}|^2}/M_s \ll 1$. Consider the contribution from exchange and anisotropy, the Kittel eigen frequency $\sim e^{i\omega t}$ and amplitudes can be derived from this eigen-equation

$$\frac{i\omega}{\gamma}\begin{pmatrix}\xi_x \\ \xi_y \\ \eta_x \\ \eta_y\end{pmatrix} = \begin{pmatrix} 0 & H_A + H_E & 0 & H_E \\ -H_A - H_E & 0 & -H_E & 0 \\ 0 & -H_E & 0 & -H_A - H_E \\ H_E & 0 & H_A + H_E & 0 \end{pmatrix}\begin{pmatrix}\xi_x \\ \xi_y \\ \eta_x \\ \eta_y\end{pmatrix}. \tag{1.13}$$

One can find the degenerate eigenvalue $\omega = \gamma\mu_0\sqrt{H_A^2 + 2H_A H_E}$ with the eigenvectors

$$\begin{pmatrix} \xi_x \\ \xi_y \\ \eta_x \\ \eta_y \end{pmatrix} = \begin{pmatrix} a \\ ia \\ b \\ ib \end{pmatrix}, \qquad \begin{pmatrix} \xi_x \\ \xi_y \\ \eta_x \\ \eta_y \end{pmatrix} = \begin{pmatrix} a \\ -ia \\ b \\ -ib \end{pmatrix}. \tag{1.14}$$

Thus in antiferromagnetic precession, there are two eigenstates with opposite chirality which are usually referred to as the *two-mode* of the AFMR.

Beyond classical approach, the magnetism dynamics can be viewed from quantum mechanical viewpoints. The Holstein-Primakoff (H-P) transformation is the standard way of associating the local spin operators S_i with the deviation operator a_i. From the usual expression of raising and lowing spin operator

$$S_i^\pm |S, S_z\rangle = \sqrt{(S \mp S_z)(S \pm S_z + 1)} |S, S_z \pm 1\rangle \tag{1.15}$$

we define the derivation number $n = S - S_z$ and identify the state $|S, S_z\rangle \equiv |n\rangle$. Then the previous relation can be rephrased into $S_i^- |n\rangle = \sqrt{2S}\sqrt{1 - n/2S} \cdot \sqrt{n+1}|n+1\rangle$ and $S_i^+ |n\rangle = \sqrt{2S}\sqrt{1 - (n-1)/2S} \cdot \sqrt{n}|n-1\rangle$, which is strikingly similar to the harmonic oscillator $a_i^\dagger |n\rangle = \sqrt{n+1}|n+1\rangle$ and $a_i |n\rangle = \sqrt{n}|n-1\rangle$. Thus we make the operator associations for the upward spin

$$S_i^- = \sqrt{2S}\, a_i^\dagger \sqrt{1 - \frac{a_i^\dagger a_i}{2S}}, \quad S_i^+ = \sqrt{2S}\sqrt{1 - \frac{a_i^\dagger a_i}{2S}}\, a_i, \quad S_i^z = S - a_i^\dagger a_i. \tag{1.16}$$

The similar association applies for the downward spins but with the interchange of S_i^+ and S_i^-, and reverse the sign of S_i^z.

In order to study the properties of collective vibrations, i.e. the magnons, one needs a further transformation of shifting from the local deviation operators $(a_i, a_i^\dagger)$ to the *on-the-fly* deviation operators $(a_{\boldsymbol{k}}, a_{\boldsymbol{k}}^\dagger)$. This can be done by the Fourier transformation such that

$$a_i = \frac{1}{\sqrt{N}} \sum_{\boldsymbol{k}} e^{i\boldsymbol{k}\cdot\boldsymbol{r}_i} a_{\boldsymbol{k}}, \tag{1.17}$$

with the orthonormality condition

$$\frac{1}{N} \sum_n e^{i(\boldsymbol{k}-\boldsymbol{k}')\cdot\boldsymbol{r}_n} = \delta(\boldsymbol{k} - \boldsymbol{k}') \tag{1.18}$$

so as to maintain the canonical bosonic commutation relations. One can also prove that the equality $\sum_i a_i^\dagger a_i = \sum_{\boldsymbol{k}} a_{\boldsymbol{k}}^\dagger a_{\boldsymbol{k}}$ holds due to this orthonormality.

As an example, we quantize the antiferromagnetic Hamiltonian of a 3D crystal material with the simplified two-sublattice model. We consider the spins of two sublattices pointing to the directions $\pm z$ in equilibrium. The Hamiltonian including external field H_0, exchange interaction and the single-ion easy-axis anisotropy reads [11, 14]

$$H = -\gamma\mu_0 \sum_{i,j} \boldsymbol{H}_0 \cdot \boldsymbol{S}_{i,j} - \sum_{i \neq j} J(S_i^+ S_j^- + S_i^- S_j^+ + 2S_i^z S_j^z) - A\sum_i (S_i^z)^2, \tag{1.19}$$

where the sub-indices i and j refer to sites in the sublattice of spin-up and spin-down respectively. For the spin-up sublattice, the lowering spin operator corresponds to the creation of spin deviation $a_i^\dagger$, while for the spin-down sublattice it is the raising spin operator corresponds to the creation of spin deviation $d_j^\dagger$ [11]. Taking the H-P and Fourier transformations, the Hamiltonian Eq. 1.19 can be written into the form of $H = E_0 + H^{(2)} + H^{(4)} + \cdots$, with each term contains an even number of bosonic operators about the on-the-fly deviations. To the low-temperature or spin-wave approximation it corresponds to taking $f_i(S) = \sqrt{1 - a_i^\dagger a_i / 2S} \approx 1$, which results in the quadratic Hamiltonian, while the non-linear effect which is important for thermal and magnon transport properties is elucidated by the higher order expansion of the factor $f_i(S)$. Now focusing on the spin-wave approximation and assuming the external field $\boldsymbol{H}_0$ applied along the z-direction, the quadratic form reads

$$H^{(2)} = \gamma\mu_0 \sum_{\boldsymbol{k}} (H_E + H_A + H_0) a_{\boldsymbol{k}}^\dagger a_{\boldsymbol{k}} + (H_E + H_A - H_0) d_{-\boldsymbol{k}}^\dagger d_{-\boldsymbol{k}} + \gamma_{\boldsymbol{k}} H_E (a_{\boldsymbol{k}} d_{-\boldsymbol{k}} + a_{\boldsymbol{k}}^\dagger d_{-\boldsymbol{k}}^\dagger),$$

$$(1.20)$$

where

$$H_E = \frac{2Sz|J|}{\mu_0\gamma}, \quad H_A = \frac{2SA}{\mu_0\gamma}, \quad (1.21)$$

are the effective exchange and anisotropy field respectively, and z is the lattice coordinate number. $\gamma_{\boldsymbol{k}}$ is the structure factor defined by $\gamma_{\boldsymbol{k}} = (1/z) \sum_{\boldsymbol{\delta}} e^{i\boldsymbol{k}\cdot\boldsymbol{\delta}}$, in which $\boldsymbol{\delta}$ is the vector connecting the z nearest neighbouring spins of opposite orientations. Diagonalizing this Hamiltonian requires a general treatment called para-unitary transformation which is illustrated in the next subsection.

1.1.2. Para-unitary transformation

In order to make clear the diagonalization of this typical quadratic Hamiltonian, which shall be used frequently in the following chapters, we introduce here a general treatment of solving this problem. The treatment which provides us with a systematic procedure in practice is mentioned as the para-unitary transformation [15, 16]. The general Hamiltonian has the form,

$$H = \sum_{r',r=1}^{m} \alpha_{r'}^\dagger \Delta_{1r'r} \alpha_r + \alpha_{r'}^\dagger \Delta_{2r'r} \alpha_{m+r}^\dagger + \alpha_{m+r'} \Delta_{3r'r} \alpha_r + \alpha_{m+r'} \Delta_{4r'r} \alpha_{m+r}^\dagger$$

$$= \begin{pmatrix} \alpha^\dagger & \alpha_m \end{pmatrix} \begin{pmatrix} \Delta_1 & \Delta_2 \\ \Delta_3 & \Delta_4 \end{pmatrix} \begin{pmatrix} \alpha \\ \alpha_m^\dagger \end{pmatrix}, \qquad (1.22)$$

where the $\alpha = (\alpha_1, \ldots, \alpha_m)^T$ and $\alpha_m^\dagger = (\alpha_{m+1}^\dagger, \ldots, \alpha_{2m}^\dagger)^T$ should be understood as column vectors of operators. Such Hamiltonian does not contains terms such as α^2, and is called bilinear Hamiltonian or Bogoliubov Hamiltonian. It often shows up in condensed matter physics e.g. all operators with index $'r'$ correspond to the same wave vector $\boldsymbol{k}$, while those with $'m + r'$ to $-\boldsymbol{k}$, and $'m'$ denotes the number of degrees of freedom within the unit cell [16]. Diagonalizing the matrix $\mathcal{H}$ amounts to a linear transformation (mixing)

1

of the annihilation α and creation $\alpha_m^\dagger$ operators into γ and γ_m such that,

$$H = \begin{pmatrix} \alpha^\dagger & \alpha_m \end{pmatrix} \mathcal{H} \begin{pmatrix} \alpha \\ \alpha_m^\dagger \end{pmatrix} = \begin{pmatrix} \gamma^\dagger & \gamma_m \end{pmatrix} \mathcal{S}^\dagger \mathcal{H} \mathcal{S} \begin{pmatrix} \gamma \\ \gamma_m^\dagger \end{pmatrix} = \begin{pmatrix} \gamma^\dagger & \gamma_m \end{pmatrix} \mathcal{E} \begin{pmatrix} \gamma \\ \gamma_m^\dagger \end{pmatrix}$$

$$= \omega \gamma^\dagger \gamma + \omega' \gamma_m^\dagger \gamma_m.$$
(1.23)

One should note that here the mixing of creation operators and annihilation operators is *not that of Bogoliubov*. The pure Bogoliubov transformation mixes the creation and annihilation operators of the same mode. But for the diagonalization of Eq. 1.22, the mixing of operators of different modes makes the column vectors of transforming matrix $\mathcal{S}$ still the eigenvector of $\mathcal{H}$, although such eigenvectors do not concur with the unitary understanding but to the so-called para-unitary concepts.

To begin with, we firstly introduces the definition of para-unit matrix $\tilde{\mathcal{I}}_{2m \times 2m}$ with $\tilde{\mathcal{I}}_{\rho\rho} = 1$ ($1 \leqslant \rho \leqslant m$), $\tilde{\mathcal{I}}_{\rho\rho} = -1$ ($m+1 \leqslant \rho \leqslant 2m$), and $\tilde{\mathcal{I}}_{\rho\rho'} = 0$ ($\rho' \neq \rho$). Any para-unitary matrix $\mathcal{S}$ satisfies the relation $\mathcal{S}^\dagger \tilde{\mathcal{I}} \mathcal{S} = \tilde{\mathcal{I}}$ and $\mathcal{S} \tilde{\mathcal{I}} \mathcal{S}^\dagger = \tilde{\mathcal{I}}$. We claim that the Hermit matrix $\mathcal{H}$ can be diagonalized by the para-unitary matrix $\mathcal{S}$ such that $\mathcal{S}^\dagger \mathcal{H} \mathcal{S} = \mathcal{E}$ if and only if matrix $\mathcal{H}$ is positive definite. The proof is to find such para-unitary matrix $\mathcal{S}$. Since $\mathcal{H}$ is positive definite, it can be written as $\mathcal{H} = \mathcal{D}^\dagger \mathcal{D}$ with $\mathcal{D}$ is invertible. We construct the unitary diagonalization for the matrix $\mathcal{D}\tilde{\mathcal{I}}\mathcal{D}^\dagger$ such that $\mathcal{U}^\dagger (\mathcal{D}\tilde{\mathcal{I}}\mathcal{D}^\dagger)\mathcal{U} = \Lambda$, and construct the positive diagonal matrix $\mathcal{E} = \tilde{\mathcal{I}}\Lambda$. Then it can be proved that the transforming matrix $\mathcal{S} = \mathcal{D}^{-1}\mathcal{U}\mathcal{E}^{1/2}$ is para-unitary and it indeed diagonalizes the Hamiltonian $\mathcal{H}$ such that $\mathcal{S}^\dagger \mathcal{H} \mathcal{S} = \mathcal{E}$. Note here that due to the Sylvester's law of inertia, the diagonal matrix Λ contains m number of positive elements and m number of negative elements (sorted), and the eigen-matrix $\mathcal{E}$ is positive definite like $\mathcal{H}$ itself. From another view of point, $\mathcal{S}^\dagger \mathcal{H} \mathcal{S} = \mathcal{E}$ equals to the fact that $\mathcal{H}\mathcal{S} = \tilde{\mathcal{I}}\mathcal{S}\Lambda$. So as $\mathcal{H}|w_\rho\rangle = \lambda_\rho \tilde{\mathcal{I}}|w_\rho\rangle$, the column vector of $\mathcal{S}$ is the para-eigenvector for matrix $\mathcal{H}$. Under the definition of inner product with metric $\tilde{\mathcal{I}}$, i.e. $\langle v_\rho | v_{\rho'} \rangle_{\tilde{\mathcal{I}}} \equiv \langle v_\rho | \tilde{\mathcal{I}} | v_{\rho'} \rangle$, the paraunitary matrix $\mathcal{S}$ is orthonormal as $\langle w_\rho | w_{\rho'} \rangle_{\tilde{\mathcal{I}}} = \tilde{\delta}_{\rho\rho'} = \pm 1$ and $\langle w_\rho | \mathcal{H} | w_{\rho'} \rangle_{\tilde{\mathcal{I}}} = \epsilon_\rho \delta_{\rho\rho'}$.

Such column vector of $\mathcal{S}$ as paraunitary eigenvector has an important interpretation that it can be viewed as the wavefunction of the original excitation expanded in the basis of elementary excitations. For simplicity, we illustrate this by taking the case that there are 2 degrees of freedom within the unit cell such as the spin-up and spin-down sublattice in the case of AFM. The transformation looks like

$$\begin{pmatrix} \alpha_u \\ \alpha_d^\dagger \end{pmatrix} = \begin{pmatrix} s_1 & s_3 \\ s_2 & s_4 \end{pmatrix} \begin{pmatrix} \gamma_1 \\ \gamma_2^\dagger \end{pmatrix}.$$
(1.24)

If we only excite the mode of γ_1, that is $\left(\langle \gamma_1 \rangle, \langle \gamma_2 \rangle \right)^T = (1, 0)^T$, then the local spin deviation can be deduced that $(\langle \alpha_u \rangle, \langle \alpha_d \rangle)^T \sim (s_1, s_2)^T$ and the relative strength of precession for spin-up and spin-down sublattice is $|s_1/s_2|^2$. It also should be noted that the canonical commutation relation for bosonic αs and γs is preserved by the para-unitarity $\mathcal{S}^\dagger \tilde{\mathcal{I}} \mathcal{S} = \tilde{\mathcal{I}}$ and $\mathcal{S} \tilde{\mathcal{I}} \mathcal{S}^\dagger = \tilde{\mathcal{I}}$.

As an example, we derive the dispersion relation for the antiferromagnetic magnons

based on the Hamiltonian (Eq. 1.20). The paraunitary transformation has the form

$$H^{(2)} = \gamma\mu_0 \sum_{\boldsymbol{k}} \begin{pmatrix} \alpha_{\boldsymbol{k}}^\dagger & \beta_{-\boldsymbol{k}} \end{pmatrix} \begin{pmatrix} u_k & v_k \\ v_k & u_k \end{pmatrix}^\dagger \begin{pmatrix} H_E + H_A + H_0 & \gamma_{\boldsymbol{k}} H_E \\ \gamma_{\boldsymbol{k}} H_E & H_E + H_A - H_0 \end{pmatrix} \begin{pmatrix} u_k & v_k \\ v_k & u_k \end{pmatrix} \begin{pmatrix} \alpha_{\boldsymbol{k}} \\ \beta_{-\boldsymbol{k}}^\dagger \end{pmatrix}$$

$$= \sum_{\boldsymbol{k}} \omega_\alpha \alpha_{\boldsymbol{k}}^\dagger \alpha_{\boldsymbol{k}} + \omega_\beta \beta_{-\boldsymbol{k}}^\dagger \beta_{-\boldsymbol{k}}.$$

$$(1.25)$$

It can be proven that the column vector of transforming matrix $\mathscr{S}$ is

$$u_k = \sqrt{\frac{\gamma\mu_0 H_E + \gamma\mu_0 H_A + \omega_k}{2\omega_k}}, \quad v_k = -\sqrt{\frac{\gamma\mu_0 H_E + \gamma\mu_0 H_A - \omega_k}{2\omega_k}}.$$

and one can check it is indeed a para-unitary matrix. The dispersion relation is given by

$$\omega_{\alpha,\beta} = \omega_{\boldsymbol{k}} \pm \gamma\mu_0 H_0, \quad \omega_{\boldsymbol{k}} = \gamma\mu_0 \sqrt{H_A^2 + 2H_E H_A + H_E^2(1 - \psi_{\boldsymbol{k}}^2)}. \tag{1.26}$$

For cubic lattice, the structure factor is

$$\psi_{\boldsymbol{k}} = \cos(k_x a/2)\cos(k_y b/2)\cos(k_z c/2), \tag{1.27}$$

where (a, b, c) are the lattice constants of the $(\hat{x}, \hat{y}, \hat{z})$ direction. In the case of AFMR, $\boldsymbol{k} = 0$ so that the resonant frequency without external field results in

$$\omega_{\text{AFMR}} \approx \gamma\mu_0 \sqrt{2H_E H_A}, \tag{1.28}$$

with the assumed week anisotropy $H_A \ll H_E$. Compared to the AFMR frequency solved in the previous subsection, one can see that the process of diagonalization is equivalent to solving the equation of motion under the same Hamiltonian.

1.2.   Elastic degree of freedom
1.2.1.   Strain, stress, and the elasticity
In a solid elastic material, a point $\boldsymbol{r}$ is displaced by externally applied stress into another point $\boldsymbol{r} + \boldsymbol{u}$. Here $\boldsymbol{r}$ is the point coordinate before deformation and $\boldsymbol{u}$ is the displacement vector. Consider a line element dl in the material between two points and after the deformation it becomes dl'. Suppose the deformation is small, it is easy to show that the change of line element is essentially captured by the elastic strain tensor ϵ_{ij} as

$$dl'^2 = dl^2 + 2\epsilon_{ij} dx_i dx_j, \tag{1.29}$$

with $\epsilon_{ij} = 1/2(\partial_i u_j + \partial_j u_i)$ as defined. Thus the fractal change of length can be calculated

$$\frac{\delta l}{l} = \frac{dl' - dl}{dl} = \epsilon_{ij}\eta_i\eta_j \tag{1.30}$$

with (η_1, η_2, η_3) are the unit vector of length $\hat{\boldsymbol{l}}$. Furthermore, to the first order of ϵ_{ij}, the volume change due to the deformation is $dV' = dV(1 + \epsilon_i^i)$ with

$$\epsilon_i^i = \epsilon_{ij}\delta^{ji} \equiv \sum_i \epsilon_{ii} \tag{1.31}$$

is a Penrose notation where the summation over dummy indices is assumed. The strain tensor is symmetric and the diagonal terms $\epsilon_{ii} = \partial_i u_i$ are associated with longitudinal deformation and off-diagonal terms are associated with shear (transverse) deformation. It is only the longitudinal strain that contributes to a change in volume, $\delta V/V = \epsilon_i^i$.

The stress tensor σ_{ij} stands for the force in the i-th direction applied onto the unit area of the j-th surface. Thus for a volume element inside the elastic bulk, the total force along i-th direction is $F_i = \partial\sigma_{ij}/\partial x_j$ (where the summation among dummy indices is assumed). It follows that the net force on an internal volume part of ΔV is

$$\int_{\Delta V} F_i dV = \int_{\Delta V} \frac{\partial \sigma_{ij}}{\partial x_j} dV = \int \sigma_{ij} dS_j, \tag{1.32}$$

where dS_j is the surface element vector directed along the outward normal. This means the internal force on the volume is applied through surface contact with the neighbouring portions and thus the equation of motion for the displacement field is

$$\rho \frac{\partial^2 u_i}{\partial t^2} = \frac{\partial \sigma_{ij}}{\partial x_j}. \tag{1.33}$$

The virtual work due to the internal force $\boldsymbol{F}$ onto the virtual displacement $\delta\boldsymbol{u}$ is $\delta R = F_i \delta u_i$ so that in the volume bulk the loss of potential energy reads

$$\int \delta R dV = \int \delta u_i \frac{\partial \sigma_{ij}}{\partial x_j} dV = \int \sigma_{ij} \delta u_i dS_j - \int \sigma_{ij} \delta \frac{\partial u_i}{\partial x_j} dV. \tag{1.34}$$

For simplicity, stress on the material surface is neglected thus we have $dR = -\sigma_{ij} d\epsilon_{ij}$. Accordingly, the change of free energy reads $dF = -TdS + \sigma_{ij} d\epsilon_{ij}$ and the relation

$$\sigma_{ij} = \frac{\partial F}{\partial \epsilon_{ij}} \tag{1.35}$$

can be understood. For isotropic bulk material the elastic free energy density acquires the following form [17]

$$F_{\text{el}} = \frac{1}{2}\lambda \left(\epsilon_i^i\right)^2 + \mu \sum_{ij} \epsilon_{ij}^2, \tag{1.36}$$

where λ and μ are the Lamé constants. Thus we have the relation between stress and the strain for isotropic material

$$\sigma_{ij} = 2\mu\epsilon_{ij} + \lambda \left(\epsilon_i^i\right) \delta_{ij}, \tag{1.37}$$

which is consistent with the general elasticity tensor relation

$$\sigma_{ij} = \sum_{kl} C_{ijkl} \epsilon_{kl}, \tag{1.38}$$

whose stiffness elements read $C_{1111} = \lambda + 2\mu$, $C_{1133} = \lambda$, $C_{1313} = 2\mu$, $C_{1113} = 0$, and other elements are acquired based on the symmetry [18]. We see typically the coefficient C_{1111} relates σ_{ii} to longitudinal strain ϵ_{ii} while the C_{1313} relates $\sigma_{i \neq j}$ to shear strain $\epsilon_{i \neq j}$, and

the C_{1133} depicts the transverse deformation ϵ_{jj} due to the stress σ_{ii} of the orthogonal direction ($\vec{i} \perp \vec{j}$).

Based on the elasticity tensor relation we have $\sigma_i^i = 3K_T \epsilon_i^i$ with $K_T = \lambda + 2\mu/3$, such that for homogeneous compression $\sigma_{ii} = -p$ the fractal change of volume is $\delta V/V = \epsilon_i^i = -p/K_T$ and thus we define the compressibility for isotropic material

$$\beta_T = K_T^{-1} = -\frac{1}{V}\frac{\partial V}{\partial p}. \tag{1.39}$$

Then the elastic free energy can be rephrased into the part combination of longitudinal and shear deformations

$$F_{\text{el}} = \frac{1}{2}K_T\left(\epsilon_i^i\right)^2 + \mu\sum_{ij}\left(\epsilon_{ij} - \frac{1}{3}\epsilon_i^i\delta_{ij}\right)^2, \tag{1.40}$$

To the uniaxial stretching, for example only $\sigma_{zz} \neq 0$, one can calculate the static deformation as $\epsilon_{zz} = \sigma_{zz}/3\,(1/\mu + 1/3K_T)$, $\epsilon_{xx} = \epsilon_{yy} = -\sigma_{zz}/3\,(1/2\mu - 1/3K_T)$, and others zero. We define the Young's modulus as the linear relation for longitudinal stretching $\sigma_{zz} = Y\epsilon_{zz}$ and Poisson ratio as the accompanying transverse compression $\epsilon_{xx} = \epsilon_{yy} = -\sigma\epsilon_{zz}$. Their relation with the Lamé coefficients are

$$\lambda = \frac{Y\sigma}{(1+\sigma)(1-2\sigma)}, \quad \mu = \frac{Y}{2(1+\sigma)}, \quad K_T = \frac{Y}{3(1-2\sigma)}. \tag{1.41}$$

The longitudinal acoustic velocity is $v_L = \sqrt{(\lambda + 2\mu)/\rho}$ while the shear acoustic velocity is $v_S = \sqrt{\mu/\rho}$. For isotropic material the averaged velocity by fitting to the Debye's temperature is [19]

$$\bar{v} = \left[\frac{1}{3}\left(\frac{1}{v_L^3} + \frac{2}{v_S^3}\right)\right]^{-\frac{1}{3}}. \tag{1.42}$$

1.2.2. Thermodynamic properties

The lattices vibration is accompanied by the change of temperature within the body either due to the internal friction or external temperature gradient. The thermal elastic coupling is made through the thermal-expansion coefficient α such that the free energy at temperature T is [17]

$$F(T) = F_0(T) - K_T\alpha\,(T - T_0)\,\epsilon_i^i + \frac{1}{2}K_T\left(\epsilon_i^i\right)^2 + \mu\sum_{ij}\left(\epsilon_{ij} - \frac{1}{3}\epsilon_i^i\delta_{ij}\right)^2, \tag{1.43}$$

with F_0 is the thermodynamic part and T_0 is the equilibrium temperature at the initial time. Since $S = -\partial F/\partial T$ we understand the entropy increase can be divided into two part:

$$\Delta S(T) = \Delta S_0(T) + K_T\alpha\epsilon_i^i. \tag{1.44}$$

The ΔS_0 denotes the thermal entropy increase without deformation

$$\Delta S_0 = \int_{T_0}^{T} C_V\,dT/T \approx C_V\frac{T - T_0}{T_0}. \tag{1.45}$$

1

This means that the absorption of heat $\Delta Q = T\Delta S$ leads not only to the increase of thermal phonon intensity, but also to the volume expansion $\epsilon_i^i = \delta V / V$. In practice, the elastic vibration can be classified into two extreme cases. One is called the *isothermal process*, which means the deformation is slow enough such that there is abundant heat exchange between the elastic body and the environment. So the body temperature is kept the same as the environment and is homogeneous within the body. For example, in the free expansion of the elastic block as environment temperature slowly increases from T_0 to T, the corresponding volume change is $\epsilon_i^i = \alpha(T - T_0)$. Thus the coupling strength α is the isothermal expansion coefficient $\alpha = \frac{1}{V} \frac{\partial V}{\partial T}\big|_p$. Another extreme situation is called *adiabatic process*, in which the deformation is changed fast enough that there is no heat exchange with the environment nor within the body itself. During this vibration, there is an accompanying temperature field entwined with the local volume expansion $C_V(T - T_0)/T_0 = -K_T \alpha \epsilon_i^i$. Thus without heat exchange, the contraction of elastic body would lead to an internal temperature increase. Combing thermal resistance with adiabatic compression, a new bulk modulus K_{ad} can be derived from thermodynamic formula

$$\frac{1}{K_{\text{ad}}} = \frac{1}{K_T} - \frac{T\alpha^2}{C_V}, \tag{1.46}$$

and the thermal-incorporated elastic free energy is

$$F = F_0 + \frac{1}{2} K_{\text{ad}} \left(\epsilon_i^i \right)^2 + \mu \sum_{ij} \left(\epsilon_{ij} - \frac{1}{3} \epsilon_i^i \delta_{ij} \right)^2 \tag{1.47}$$

From Eq. 1.44 we see the specific heat at constant pressure is $C_P = TdS/dT = C_V + TK_T\alpha^2$, and thus leads to the equality

$$\frac{C_P}{C_V} = \frac{K_{\text{ad}}}{K_T}, \tag{1.48}$$

within the first order approximation.

Since the specific heat $C_V = dE/dT$ is defined as the change of energy per unit of temperature increase and α denotes the volume expansion as for temperature increase, these two moduli should be somehow related. Therefore it yields that $\alpha K_T = -\frac{\partial V}{\partial T}\big|_p \frac{\partial P}{\partial V}\big|_T = \frac{\partial P}{\partial T}\big|_V$ meaning the pressure required to prevent thermal expansion at fixed volume. It equals to $\frac{\partial S_0}{\partial V}\big|_T$ because of the thermal dynamics potential relation. From another point of view, thermal entropy S_0 is related to the volume due to the fact that the phonon frequency is volume dependent. The Boltzmann entropy is $S_0 = -k_B \sum_n p_n \log p_n$ with $p_n = \frac{e^{\beta\hbar\omega}-1}{e^{\beta\hbar\omega}} e^{-\beta\hbar\omega n}$ stands for the probability of n number of phonons of energy $\hbar\omega$ inside the solid bulk. With the phonon's specific heat $C_V = \frac{\partial}{\partial T} \sum_n p_n \hbar\omega n$, it can be proven that the relation $\frac{\partial S_0}{\partial V}\big|_T = -\frac{1}{\omega} \frac{\partial \omega}{\partial V} C_V$ holds, and defining the elastic Grüneisen parameter $\gamma_E = -\partial \log \omega / \partial \log V$ we arrive at the Grüneisen relation [20]

$$\gamma_E = \alpha K_T V / C_V \quad \longleftrightarrow \quad \alpha = \beta_T \gamma_E \rho C_V. \tag{1.49}$$

The central point is that thermal and elastic properties are controlled by the same inter-atomic forces and it is the Grüneisen parameter that gives them a theoretical connection. For isotropic materials the elastic Grüneisen parameter can be calculated from the Poisson ratio [21, 22]

$$\gamma_E = \frac{3}{2}\left(\frac{1+\sigma}{2-3\sigma}\right). \tag{1.50}$$

1.2.3. Magnetoelastic coupling

The magnetoelastic coupling (MEC) in magnetic insulator mainly comes from two origins. One is the crystal field applied to the spin has dependency on the elastic deformation and the second comes from the dipolar interaction between the spins which also depends on the distance between such spins. To the lowest order expression, the phenomenological Hamiltonian density for MEC is given by [23]

$$\begin{aligned}
H_{MEC} &= B_1[(\alpha_1^2 + \beta_1^2)\epsilon_{11} + c.p.] + B_2[(\alpha_1\alpha_2 + \beta_1\beta_2)\epsilon_{12} + c.p.] \\
&+ B_3[\alpha_1\beta_1\epsilon_{11} + c.p.] + B_4[(\alpha_1\beta_2 + \alpha_2\beta_1)\epsilon_{12} + c.p.],
\end{aligned} \tag{1.51}$$

where $\alpha_i = M_i^1/M_s$ and $\beta_i = M_i^2/M_s$ stand for the cosine of angle of the magnetization with respect to the crystallographic axis, and $c.p.$ denotes cyclic permutation. We see that the B_1 and B_2 represent the MEC strength of one-ion and B_3 and B_4 of the two-ions respectively. For antiferromagnetic case one should usually discern the $\boldsymbol{\alpha}$ and $\boldsymbol{\beta}$ because the two spins of the sub-lattice are often not anti-parallel to each other unless for very small external field. However, for the case of ferromagnet, there is no sub-lattice and $\boldsymbol{\alpha} = \boldsymbol{\beta}$, thus Eq. 1.51 can be simplified into

$$\begin{aligned}
H_{MEC} &= B_{\parallel}\left(\alpha_1^2\epsilon_{11} + c.p.\right) + B_{\perp}\left(\alpha_1\alpha_2\epsilon_{12} + c.p.\right) \\
&= \frac{B_{\parallel}}{M_s^2}\left(M_1^2\epsilon_{11} + c.p.\right) + \frac{B_{\perp}}{M_s^2}\left(M_1 M_2\epsilon_{12} + c.p.\right).
\end{aligned} \tag{1.52}$$

These MEC strengths can be determined through the magnetostriction experiment in which the magnetization orientation can be tuned by an external field while the static volume change $\delta V/V$ or fractal change of length $\delta l/l$ can be measured. Together with the elastic free energy H_E (Eq. 1.40) the static strain can be derived by differentiating the total Hamiltonian $\partial(H_E + H_{MEC})/\partial\epsilon_{ij} = 0$ and the link between magnetization and static (equilibrium) strain is thus established.

In many applications, the elastic deformation could be considered as static compared to the high magnetic precession frequency. Then the magnetoelastic coupling can be treated as an effective anisotropy which is a function of strain $\mu_0 \boldsymbol{H}_A^{MEC} = -\partial H_{MEC}/\partial\boldsymbol{M}$. Due to the fact that the AFMR frequency is largely affected by the anisotropy field (Eq. 1.28) such stress-dependent MEC effects are much more accentuated in antiferromagnets than in ferromagnets and play an important role in studying the spin waves of Heisenberg antiferromagnetic models [24].

One should keep in mind that the MEC described by Eq. 1.51 is valid only for the case of small external field and the magnet stays in the low symmetry phase. If the external field is larger than the spin-flop limit or the temperature is close to the phase transition then the spins within magnet cannot keep parallel (or anti-parallel for AFM) so that the

coupling energy becomes lattice dependent. This regime is referred to as the exchange magnetoelastic effect and the volume change is related to the change in the static two-spin correlation function between nearest neighbours [23]

$$\frac{\delta V}{V} = -N z \beta_T J \gamma_M \frac{\delta \langle \mathbf{S}_i \cdot \mathbf{S}_j \rangle}{V}, \tag{1.53}$$

with N the number of spins per unit volume, z the lattice coordinate number, J the coupling strength before the additional deformation, and β_T is the compressibility as noted in previous section. $\gamma_M = -\partial \log J / \partial \log V$ is the magnetic Gruneisen constant which depicts the dependence of J on elastic deformation [25]. Similar to the elastic Gruneisen relation (Eq. 1.49), we see that the Eq. 1.53 can be rephrased into $\alpha_M = \beta_T \gamma_M \rho C_M$ with the magnetic specific heat due to the exchange coupling when temperature close to T_c is

$$C_M = -N z J \frac{\partial \langle \mathbf{S}_i \cdot \mathbf{S}_j \rangle}{\partial T}. \tag{1.54}$$

1.3.   The electromagnetic modes in waveguide

In this section we describe the TE and TM mode of electromagnetic (EM) waves in a hollow waveguide of uniform cross section. Classically the electrodynamics is described by the Maxwell equations in vacuum and by assuming sinusoidal time dependence $e^{-i\omega t}$ the equations take the form [26]

$$\begin{aligned} \nabla \times \mathbf{E} = i\mu_0 \omega \mathbf{H} && \nabla \cdot \mathbf{H} = 0 \\ \nabla \times \mathbf{H} = -i\epsilon_0 \omega \mathbf{E} && \nabla \cdot \mathbf{E} = 0. \end{aligned} \tag{1.55}$$

Applying the cross product twice to $\mathbf{E}$ and $\mathbf{H}$ in Eq. 1.55 and using the relation $\nabla \times (\nabla \times \mathbf{A}) = \nabla(\nabla \cdot A) - \nabla^2 A$, the electromagnetic wave equation of motion has the formula

$$\left(\nabla^2 + \mu_0 \epsilon_0 \omega^2\right) \begin{Bmatrix} \mathbf{E} \\ \mathbf{H} \end{Bmatrix} = 0. \tag{1.56}$$

Assuming the cylindrical waveguide having its longitudinal direction point along the z-axis, we can exclude the travelling wave dependence on z as e^{ikz} so that $\mathbf{E} = \mathcal{E}(x, y)e^{i(kz-\omega t)}$ and $\mathbf{H} = \mathcal{H}(x, y)e^{i(kz-\omega t)}$. The equation of motion reduced to the dimension of transverse plane (x, y) becomes an eigenvalue problem

$$\left[\nabla_t^2 + \left(\mu_0 \epsilon_0 \omega^2 - k^2\right)\right] \begin{Bmatrix} \mathcal{E} \\ \mathcal{H} \end{Bmatrix} = 0, \tag{1.57}$$

which can be solved together with the proper boundary conditions. Assume the waveguide is made of perfectly conducting material so that there is no EM field inside, then the boundary conditions on the cylinder's inner surface are $\mathbf{n} \times \mathcal{E} = 0$ and $\mathbf{n} \cdot \mathcal{H} = 0$.

   By separating the transverse components from the longitudinal part, the Maxwell's equation can be rephrased into the relation [27]

$$\mathcal{E}_t = \frac{i}{(\mu_0 \epsilon_0 \omega^2 - k^2)} \left[k\nabla_t \mathcal{E}_z - \mu_0 \omega \hat{z} \times \nabla_t \mathcal{H}_z \right] \tag{1.58}$$

$$\mathcal{H}_t = \frac{i}{(\mu_0 \epsilon_0 \omega^2 - k^2)} \left[k\nabla_t \mathcal{H}_z + \epsilon_0 \omega \hat{z} \times \nabla_t \mathcal{E}_z \right]. \tag{1.59}$$

We see the transverse components can be determined if $\mathscr{E}_z$ and $\mathscr{H}_z$ have been solved from the eigenvalue problem (Eq. 1.57). It turns out that the low-energy branches of EM modes in the waveguide have the property that either $\mathscr{E}_z = 0$ or $\mathscr{H}_z = 0$ and they are referred to as transverse electric (TE) mode and transverse magnetic (TM) mode respectively. For solving the eigenvalue equation of each modes the boundary condition shall be written in more detail. In specific the surface boundary condition for the TE mode is $\frac{\partial \mathscr{H}_z}{\partial n}\big|_S = 0$ and for the TM mode it is required $\mathscr{E}_z\big|_S = 0$. Thus the profile of electromagnetic wave can be determined by solving the scalar equation [27]

$$\left(\nabla_t^2 + \gamma^2\right)\psi = 0, \qquad \gamma^2 = \mu_0\epsilon_0\omega^2 - k^2, \tag{1.60}$$

subjecting to the boundary conditions on the waveguide surface,

$$\psi\big|_S = 0 \qquad \text{or} \qquad \frac{\partial \psi}{\partial n}\Big|_S = 0. \tag{1.61}$$

We see the contracting nature in the (x, y) plane shall lead to a standing wave profile for the field ψ and the discrete branching modes in the dispersion relation, i.e. the γ_λ and $\omega_\lambda(k)$, should be expected. One should also note that for either TM or TE modes the transverse electric and magnetic fields are related by

$$\mathcal{H}_t = \frac{1}{Z}\hat{z} \times \mathcal{E}_t, \tag{1.62}$$

with $Z = k/(\epsilon_0\omega)$ or $Z = \mu_0\omega/k$ are called the impedances for the TM and TE mode respectively.

As an example which will be used in Chapter 4, we consider the rectangular waveguide with inner dimension (a, b, L) and assume the length $L \gg a > b$. For the TE mode, the profile equation is $(\partial^2/\partial x^2 + \partial^2/\partial y^2 + \gamma^2)\mathscr{H}_z = 0$ with boundary condition $\partial \mathscr{H}_z/\partial x = 0$ at $x = 0, a$ and $\partial \mathscr{H}_z/\partial y = 0$ at $y = 0, b$. The solution is therefore

$$
\begin{aligned}
\mathscr{H}_z &= B_0 \cos\left(\frac{n\pi x}{a}\right)\cos\left(\frac{m\pi y}{b}\right) \\
\mathscr{H}_x &= -\frac{ikB_0}{(\omega_\lambda/c)^2 - k^2}\left(\frac{n\pi}{a}\right)\sin\left(\frac{n\pi x}{a}\right)\cos\left(\frac{m\pi y}{b}\right) \\
\mathscr{H}_y &= -\frac{ikB_0}{(\omega_\lambda/c)^2 - k^2}\left(\frac{m\pi}{b}\right)\cos\left(\frac{n\pi x}{a}\right)\sin\left(\frac{m\pi y}{b}\right),
\end{aligned}
\tag{1.63}
$$

with dispersion relation

$$\omega_\lambda(k) = c\sqrt{\gamma_\lambda^2 + k^2}, \tag{1.64}$$

in which $c = \frac{1}{\sqrt{\mu_0\epsilon_0}}$ is the speed of light in vacuum and

$$\gamma_\lambda = \sqrt{\gamma_x^2 + \gamma_y^2} = \sqrt{n^2\pi^2/a^2 + m^2\pi^2/b^2} \tag{1.65}$$

stands for the cut-off frequency. λ represents the mode structure (including the polarization), noted such as $\lambda = \{1, 0, \text{TE}\}$. The chirality of transverse magnetic field flips sign
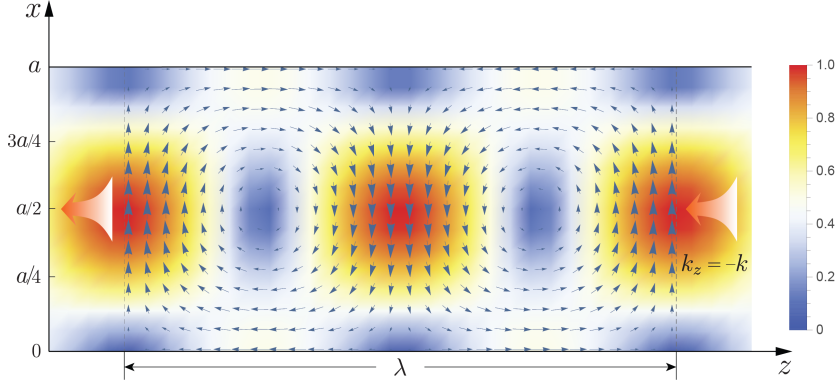
Figure 1.2: The spatial distribution of magnetic field $\boldsymbol{H}$ for the TE_{10} mode which has lowest dispersion band in the rectangular waveguide. The arrows shows the direction of $\boldsymbol{H}$ field and the color shading indicates its relative magnitude.

for the reversed propagation and in general we have

$$
\begin{aligned}
\boldsymbol{\mathcal{E}}_\lambda(k) &= \boldsymbol{\mathcal{E}}_{t,\lambda}(k) + \mathscr{E}_{z,\lambda}(k)\hat{z} \\
\boldsymbol{\mathcal{H}}_\lambda(k) &= \boldsymbol{\mathcal{H}}_{t,\lambda}(k) + \mathscr{H}_{z,\lambda}(k)\hat{z} \\
\boldsymbol{\mathcal{E}}_\lambda(-k) &= \boldsymbol{\mathcal{E}}_{t,\lambda}(k) - \mathscr{E}_{z,\lambda}(k)\hat{z} \\
\boldsymbol{\mathcal{H}}_\lambda(-k) &= -\boldsymbol{\mathcal{H}}_{t,\lambda}(k) + \mathscr{H}_{z,\lambda}(k)\hat{z}.
\end{aligned}
\tag{1.66}
$$

Since the TM_{10} mode does not exist, the TE_{10} mode has the lowest cutoff frequency $\omega_{10} = c\pi/a$ and therefore is the one used in most practices [28]. A snapshot of the oscillating magnetic field $\boldsymbol{H}$ is shown in Fig 1.2.

Quantum mechanically the $\boldsymbol{E}$ and $\boldsymbol{H}$ fields can be expanded into the combination of eigen-profile distribution multiplied by time-dependent photon operator,

$$
\begin{aligned}
\boldsymbol{E} &= \sum_{k,\lambda} \boldsymbol{\mathcal{E}}_\lambda(k) e^{ikz}\hat{p}_{k,\lambda} + \bar{\boldsymbol{\mathcal{E}}}_\lambda(k) e^{-ikz}\hat{p}_{k,\lambda}^\dagger \\
\boldsymbol{H} &= \sum_{k,\lambda} \boldsymbol{\mathcal{H}}_\lambda(k) e^{ikz}\hat{p}_{k,\lambda} + \bar{\boldsymbol{\mathcal{H}}}_\lambda(k) e^{-ikz}\hat{p}_{k,\lambda}^\dagger.
\end{aligned}
\tag{1.67}
$$

Since the profile distributions are solved from the eigen equation different modes should be orthogonal to each other. Thus by proper normalization one can rewrite the EM Hamiltonian into the independent harmonic oscillator form. It turns out for the TE and TM mode, the proper orthonormal conditions are

$$
\begin{aligned}
\int \boldsymbol{\mathcal{E}}_{t,\lambda}(k) \cdot \boldsymbol{\mathcal{E}}_{t,\mu}(k)\, dA &= \xi_W \delta_{\lambda\mu} & \int \mathscr{E}_{z,\lambda}(k)\mathscr{E}_{z,\mu}(k)\, dA &= -\xi_W \frac{\gamma_\lambda^2}{k^2}\delta_{\lambda\mu} \\
\int \boldsymbol{\mathcal{H}}_{t,\lambda}(k) \cdot \boldsymbol{\mathcal{H}}_{t,\mu}(k)\, dA &= \xi_W \frac{1}{Z_k^2}\delta_{\lambda\mu} & \int \mathscr{H}_{z,\lambda}(k)\mathscr{H}_{z,\mu}(k)\, dA &= -\xi_W \frac{\gamma_\lambda^2}{k^2 Z_k^2}\delta_{\lambda\mu},
\end{aligned}
\tag{1.68}
$$

where the factor $\xi_W = \hbar\omega_k/\epsilon_0$ and Z_k is the waveguide impedance for TE and TM mode.

Inserting these component relations into the electromagnetic energy we have the photon Hamiltonian per unit length of waveguide reading as

$$
\begin{aligned}
\hat{H}_{em} &= \int d\boldsymbol{r} \frac{\epsilon_0}{2}\hat{\boldsymbol{E}}^2 + \frac{\mu_0}{2}\hat{\boldsymbol{H}}^2 \\
&= \sum_{k,\lambda} \int dxdy \left[\epsilon_0 \boldsymbol{\mathcal{E}}_\lambda(k) \cdot \bar{\boldsymbol{\mathcal{E}}}_\lambda(k)\,\hat{p}^\dagger_{k,\lambda}\hat{p}_{k,\lambda} + \mu_0 \boldsymbol{\mathcal{H}}_\lambda(k) \cdot \bar{\boldsymbol{\mathcal{H}}}_\lambda(k)\,\hat{p}^\dagger_{k,\lambda}\hat{p}_{k,\lambda} \right] \quad (1.69) \\
&= \hbar \sum_{k,\lambda} \omega_k^\lambda \hat{p}^\dagger_{k,\lambda}\hat{p}_{k,\lambda}.
\end{aligned}
$$

Note that during the derivation, the terms $\hat{p}_{k,\lambda}\hat{p}_{-k,\lambda}$ cancel out by the summation of $\boldsymbol{\mathcal{E}}_\lambda(k) \cdot \boldsymbol{\mathcal{E}}_\lambda(-k) + \boldsymbol{\mathcal{H}}_\lambda(k) \cdot \boldsymbol{\mathcal{H}}_\lambda(-k)$.

1.4. Thesis outline

In this thesis we study the interplay of magnetism with the elastic and electrodynamics degree of freedom in several hybrid systems. As first part of this thesis, Chapter 2 and 3 have been devoted to investigate the magnetoelastic coupling in specially designed nanostructures. In Chapter 2 we worked on the chiral pumping of surface acoustic wave by the ferromagnetic resonance of YIG nanowire mounted on top of an acoustic substrate. The linear magnetoelastic coupling for small perturbation has been applied and the magnet stays in ordered state far below the critical temperature. In Chapter 3 we extended the analysis into a broader temperature range even over the phase transition. We discussed a theoretical scheme of incorporating the exchange magnetoelastic interaction into the thermal elastic dynamics for the thin membranes of 2D antiferromagnetic material with restricted geometry. This model has been validated by predicting the temperature dependency of observables and followed by comparison with the experiment measured curves for the FePS$_3$ flake resonator.

The second part of this thesis turns to investigate the interaction of spins with microwaves in the waveguide and cavity setups. Chapter 4 discusses the inter-excitations between multiple millimeter-sized ferromagnets mediated by waveguide photons. The magnon-photon couplings are found to be chiral by tuning the magnet's position inside the waveguide and super/sub-radiant states can be realized for selected frequencies. In Chapter 5 we study an optical method to manipulate the spins flipping process which serves as an energy exchange protocol between charger (photons) and the storage element (spins). We demonstrated the enhancement of collective spin flipping speed inside a single mode photon cavity which can be modeled by the Dicke Hamiltonian. This speedup effect is found to originate from the cooperative interactions among the spins instead of the quantum entanglement.

References

[1] J. M. D. Coey, *Magnetism and Magnetic Materials* (Cambridge University Press, 2010).

[2] S. Blundell, *Magnetism in Condensed Matter*, Oxford Master Series in Condensed Matter Physics (OUP Oxford, 2001).

1

[3] G. Salis, Y. Kato, K. Ensslin, D. C. Driscoll, A. C. Gossard, and D. D. Awschalom, *Electrical control of spin coherence in semiconductor nanostructures,* Nature **414**, 619 (2001).

[4] J. P. Sethna, *Order parameter, broken symmetry, and topology,* (2009), arXiv:cond-mat/9204009 .

[5] J. Goldstone, A. Salam, and S. Weinberg, *Broken symmetries,* Phys. Rev. **127**, 965 (1962).

[6] L.-P. Levy, *Magnetism and Superconductivity* (Springer-Verlag Berlin Heidelberg, 2000).

[7] R. Pathria and P. D. Beale, *Statistical Mechnics* (Elsevier, 2011).

[8] W. Nolting and A. Ramakanth, *Quantum theory of magnetism* (Springer-Verlag Berlin Heidelberg, 2009).

[9] G. Burkard, D. Loss, and D. P. DiVincenzo, *Coupled quantum dots as quantum gates,* Phys. Rev. B **59**, 2070 (1999).

[10] R. Brunner, Y.-S. Shin, T. Obata, M. Pioro-Ladrière, T. Kubo, K. Yoshida, T. Taniyama, Y. Tokura, and S. Tarucha, *Two-qubit gate of combined single-spin rotation and interdot spin exchange in a double quantum dot,* Phys. Rev. Lett. **107**, 146801 (2011).

[11] S. M. Rezende, A. Azevedo, and R. L. Rodríguez-Suárez, *Introduction to antiferromagnetic magnons,* Journal of Applied Physics **126**, 151101 (2019).

[12] J. C. López Ortiz, G. A. Fonseca Guerra, F. L. A. Machado, and S. M. Rezende, *Magnetic anisotropy of antiferromagnetic* $RbMnf_3$, Phys. Rev. B **90**, 054402 (2014).

[13] L. D. Landau and E. M. Lifshitz, *Electrodynamics of Continuous Media* (Butterworth-Heinemann, 1984).

[14] D. Lançon, H. C. Walker, E. Ressouche, B. Ouladdiaf, K. C. Rule, G. J. McIntyre, T. J. Hicks, H. M. Rønnow, and A. R. Wildes, *Magnetic structure and magnon dynamics of the quasi-two-dimensional antiferromagnet* $FePS_3$, Phys. Rev. B **94**, 214407 (2016).

[15] J. H. P. Colpa, *Diagonalization of the quadratic boson hamiltonian,* Physica A: Statistical Mechanics and its Applications **93**, 327 (1978).

[16] K. Shen, *Finite temperature magnon spectra in yttrium iron garnet from a mean field approach in a tight-binding model,* New Journal of Physics **20**, 043025 (2018).

[17] L. D. Landau, L. P. Pitaevskii, A. M. Kosevich, and E. M. Lifshitz, *Theory of Elasticity* (Butterworth-Heinemann, 1986).

[18] G. S. Kino, *Acoustic waves: devices, imaging, and analog signal processing* (Prentice-Hall, 1987).

[19] O. L. Anderson, *A simplified method for calculating the debye temperature from elastic constants,* Journal of Physics and Chemistry of Solids **24**, 909 (1963).

[20] F. D. Stacey and J. H. Hodgkinson, *Thermodynamics with the grüneisen parameter: Fundamentals and applications to high pressure physics and geophysics,* Physics of the Earth and Planetary Interiors **286**, 42 (2019).

[21] V. N. Belomestnykh and E. P. Tesleva, *Interrelation between anharmonicity and lateral strain in quasi-isotropic polycrystalline solids,* Tech. Phys. **49**, 1098–1100 (2004).

[22] D. S. Sanditov and V. N. Belomestnykh, *Relation between the parameters of the elasticity theory and averaged bulk modulus of solids,* Tech. Phys. **56**, 1619–1623 (2011).

[23] Y. Shapira and N. F. Oliveira, *Magnetostriction, magnetoelastic coupling, and the magnetic grüneisen constant in the antiferromagnet RbMnF3,* Phys. Rev. B **18**, 1425 (1978).

[24] D. E. Eastman, *Magneto-elastic coupling in RbMnF3,* Phys. Rev. **156**, 645 (1967).

[25] G. O. Gomes, L. Squillante, A. C. Seridonio, A. Ney, R. E. Lagos, and M. de Souza, *Magnetic grüneisen parameter for model systems,* Phys. Rev. B **100**, 054446 (2019).

[26] D. J. Griffiths, *Introduction to Electrodynamics*, 4th ed. (Cambridge University Press, 2017).

[27] J. D. Jackson, *Classical Electrodynamics, 3rd Edition* (Wiley, 1998).

[28] E. F. Kuester, *Theory of Waveguides and Transmission Lines* (CRC, 2020).

2

Nonreciprocal pumping of phonon spin by magnetization dynamics

The first step to achieve your goal is to make this goal your dream.

Lao-tzu

In this chapter we propose a theory of chiral pumping of surface acoustic waves (SAWs) by magnetic nanowires on top of a dielectric film. The magnetic dynamics in a single nanowire pumps SAWs with opposite angular momenta into opposite directions, thus generates a phonon spin current. Two parallel nanowires forms an phononic cavity that at geometrical resonances it pumps an unidirectional SAW current into half of the surface plane. This mechanism paves the way to control surface-phonon transport by magnetization dynamics.

2.1. Introduction

Surface acoustic waves (SAWs) on the surface of high-quality piezoelectric crystals are frequently employed for traditional signal processing [2], but are also excellent mediators for coherent information exchange between distant quantum systems such as superconducting qubits and/or nitrogen-vacancy centers [3–5]. Piezoelectrically excited coherent SAWs drive the ferromagnetic resonance (FMR) by magnetostriction [6–11], excite spin waves parametrically [12], and generate electron spin currents by the rotation-spin coupling [13, 14]. Conventional insulators often have good acoustic quality but only small piezoelectric effects, rendering the direct excitation, manipulation, and detection of the coherent SAWs challenging. The phonon pumping [15], i.e., the excitation of bulk sound waves in a high-quality acoustic insulator by the dynamics of a proximity magnetic layer via the magnetoelastic coupling [16, 17], may be useful here. Bulk phonons in the insulator gadolinium gallium garnet (GGG) can couple two yttrium iron garnet (YIG) magnetic layers over millimeters [18, 19].

Here we address the coherent excitation and manipulation of Rayleigh SAWs by magnetization dynamics, which is possible in a lateral planar configuration with ferromagnetic nanowires on top of a high-quality nonmagnetic insulator, as illustrated in F2.1. Similar configurations on magnetic substrates led to the electrical detection of diffuse magnon transport [20, 21] and discovery of nonreciprocal magnon propagation [22], i.e., the generation of a unidirectional spin current in half space. Magnetic stray fields of the magnetization dynamics also generate chiral electron and waveguide photon transport. The unidirectional excitation of SAWs is important for acoustic device applications, which conventionally is achieved by metal electrodes on a piezoelectric crystal such that reflected SAWs constructively interfere with the source. This is a pure geometrical effect that is efficient at sub-GHz frequencies and sample dimensions that match the SAW wavelength [23].

We focus on the unidirectional excitation of SAWs via magnetic nanostructures on top of a dielectric substrate that are brought into FMR by external microwaves. We predict effects that are very different from the reported nonreciprocity, i.e., a sound velocity that depends on direction [10, 24], which is enhanced in magnetic multilayers on top of a piezoelectric substrate [25, 26]. The magnetic order of, e.g., a wire on top of a dielectric, does not couple nonreciprocally to the surface phonons in the configuration in Fig. 1, but excites both left- and right propagating phonons, even though the angular momentum current has a direction because of the momentum-rotation coupling of Rayleigh SAWs. However, we predict robust unidirectional excitation of SAW phonons in a phononic cavity formed by two parallel wires. The SAWs actuated by the first wire interact with the second one (which does not see the microwaves) and excite its magnetization, which in turn emits phonons. The phonons from both sources interfere destructively on half of the surface and the net phonon pumping becomes unidirectional. Constructive interference between the two nanowires induces standing SAWs as in a Fabry-Pérot cavity. Conventional unidirectional electric transducer [23] operate by a pure geometrical interference effect that works only for a fixed sub-GHz frequency. Our magnetic unidirectional transducer operates by a dynamical phase shift and provides new functionalities, such as robust high frequency tunability and switchability.

We firstly introduce the derivation of surface acoustic wave profile in section 2.2
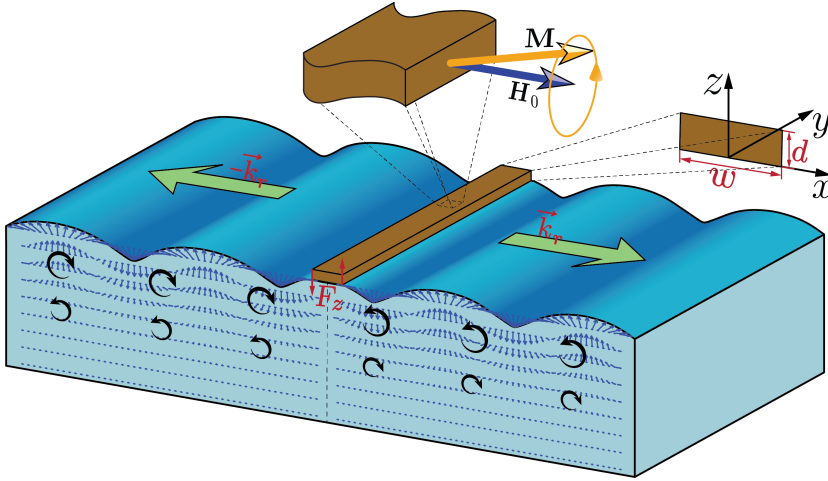
Figure 2.1: Surface-phonon pumping by one magnetic nanowire (brown) on top of the acoustic insulator (blue). A static magnetic field $\boldsymbol{H}_0$ applied in the $\vec{x}$ direction saturates the magnetization. The pumped Rayleigh SAWs by the nanowire FMR propagate and rotate in opposite directions at the two sides of the nanowire as indicated by the green and black arrows, respectively.

based on which the quantization into SAW phonons are presented in the following section 2.3. The quantization of the hybrid system, namely the magnetic FMR and its coupling to the SAW phonons are derived in details. In section 2.4 we derives explicitly the SAW pumping driven by the FMR on single magnetic nanowire. The unidirectional angular momentum flux of surface acoustic wave has been derived. We clarifies the coherent reflection of SAW phonon by introducing a second nanowire in section 2.5. The standing wave profile is shown and the photon transmission is plotted. We conclude with a short discussion in Sec. 2.6.

2.2.   Surface acoustic wave

We start our discussion by providing the necessary formalism about the Rayleigh surface acoustic wave which shall be often cited in the following sections. We only consider the Rayleigh SAW on the surface of solid, isotropic, perfectly elastic plane and the main contents are referred to the book [27] with some notation adjustments.

We first introduce the scalar potential φ and vector potential $\vec{A}$ for the displacements field so that it can be written in the form,

$$\boldsymbol{u} = \nabla\varphi + \nabla \times \boldsymbol{A}. \tag{2.1}$$

For Rayleigh SAW only component of the vector potential along y axis will have nonzero magnitude so that $\boldsymbol{A}l = A_y \vec{y}$. In this case, the φ and A_y are called the potentials of longitudinal and shear waves, respectively. Thus the displacement is further expressed in the potential formalism,

$$\boldsymbol{u} = \nabla\varphi + \nabla \times \boldsymbol{A} = \left(\frac{\partial\varphi}{\partial x} - \frac{\partial A_y}{\partial z}\right)\vec{x} + \left(\frac{\partial\varphi}{\partial z} + \frac{\partial A_y}{\partial x}\right)\vec{z}. \tag{2.2}$$

2

Since there is no displacement along y axis, only the strain tensors $\epsilon_{xx}, \epsilon_{zz}, \epsilon_{xz}$ have none vanishing magnitudes, which can be expression in the potential fields

$$
\begin{aligned}
\epsilon_{xx} &= \frac{\partial^2 \varphi}{\partial x^2} - \frac{\partial^2 A_y}{\partial x \partial z}, \\
\epsilon_{zz} &= \frac{\partial^2 \varphi}{\partial z^2} + \frac{\partial^2 A_y}{\partial x \partial z}, \\
\epsilon_{xz} &= \frac{\partial^2 \varphi}{\partial x \partial z} + \frac{1}{2}\left(\frac{\partial^2 A_y}{\partial x^2} - \frac{\partial^2 A_y}{\partial z^2} \right).
\end{aligned}
\tag{2.3}
$$

Based on the elasticity tensor relation $\sigma_{ij} = \sum_{kl} C_{ijkl}\epsilon_{kl}$ and stiffness coefficient C_{ijkl} (Eq. 1.38), the strain tensors then read

$$
\begin{aligned}
\sigma_{xx} &= \lambda \left(\frac{\partial^2 \varphi}{\partial x^2} + \frac{\partial^2 \varphi}{\partial z^2} \right) + 2\mu \left(\frac{\partial^2 \varphi}{\partial x^2} - \frac{\partial^2 A_y}{\partial x \partial z} \right), \\
\sigma_{zz} &= \lambda \left(\frac{\partial^2 \varphi}{\partial x^2} + \frac{\partial^2 \varphi}{\partial z^2} \right) + 2\mu \left(\frac{\partial^2 \varphi}{\partial z^2} + \frac{\partial^2 A_y}{\partial x \partial z} \right), \\
\sigma_{xz} &= \mu \left(2\frac{\partial^2 \varphi}{\partial x \partial z} + \frac{\partial^2 A_y}{\partial x^2} - \frac{\partial^2 A_y}{\partial z^2} \right).
\end{aligned}
\tag{2.4}
$$

Putting the stress and displacement expression (Eq. 2.4 and Eq. 2.2) into the elastic equation of motion

$$
\rho \frac{\partial^2 u_i}{\partial t^2} = \sum_j \frac{\partial \sigma_{ij}}{\partial x_j},
\tag{2.5}
$$

we can derive the wave equations for longitudinal and shear potential respectively:

$$
\begin{aligned}
\frac{\partial^2 \varphi}{\partial x^2} + \frac{\partial^2 \varphi}{\partial z^2} &= \frac{\rho}{\lambda + 2\mu} \frac{\partial^2 \varphi}{\partial t^2}, \\
\frac{\partial^2 A_y}{\partial x^2} + \frac{\partial^2 A_y}{\partial z^2} &= \frac{\rho}{\mu} \frac{\partial^2 A_y}{\partial t^2}.
\end{aligned}
\tag{2.6}
$$

Next we assume the plane wave solution, letting $\varphi(\boldsymbol{r}, t) = \varphi(z)e^{i(kx-\omega t)}$ and $A_y(\boldsymbol{r}, t) = A_y(z)e^{i(kx-\omega t)}$ and defining $\omega = k_l\sqrt{(\lambda+2\mu)/\rho} = k_t\sqrt{\mu/\rho}$, the potential wave equation can be simplified as

$$
\begin{aligned}
\frac{\partial^2 \varphi}{\partial x^2} + \frac{\partial^2 \varphi}{\partial z^2} + k_l^2 \varphi &= 0, \\
\frac{\partial^2 A_y}{\partial x^2} + \frac{\partial^2 A_y}{\partial z^2} + k_t^2 A_y &= 0.
\end{aligned}
\tag{2.7}
$$

We clearly see that the potential φ represents the longitudinal vibration and $\boldsymbol{A}$ for the shear one (henceforth referred to as the longitudinal and shear potential). Further solve this equation of motion we get

$$
\begin{aligned}
\varphi &= \varphi_k e^{\sqrt{k^2-k_l^2}\, z} \cdot e^{i(kx-\omega t)}, \\
A_y &= A_k e^{\sqrt{k^2-k_t^2}\, z} \cdot e^{i(kx-\omega t)}.
\end{aligned}
\tag{2.8}
$$

We note the reader that z takes negative values inside the acoustic substrate and thus it decays out into the depth.

The boundary condition is that there is no stress along the z axis on the surface, that is, $\sigma_{zz}|_{z=0} = 0$, $\sigma_{xz}|_{z=0} = 0$. Based on these requirements we insert the solution Eq. 2.8 back into the stress expression (Eq. 2.4) to derive the relation between φ_0 and A_0 and also the dispersion relation $\omega(k)$ that:

$$A_k = \frac{i2k\sqrt{k^2 - k_l^2}}{k_t^2 - 2k^2}\varphi_k = -\frac{i2kq}{k^2 + s^2}\varphi_k, \qquad (2.9)$$

and

$$4k^2 qs - (k^2 + s^2)^2 = 0 \qquad (2.10)$$

with $q = \sqrt{k^2 - k_l^2}$ and $s = \sqrt{k^2 - k_t^2}$. Note that the wave vectors of longitudinal and shear wave $(k_l,\ k_t)$ is a linear function of frequency ω and one shall see later that the k for SAW shall definitely larger than k_l and k_t. After a transformation, the Eq. 2.10 reduces to the form of polynomial equation

$$\eta^6 - 8\eta^4 + 8(3 - 2\zeta^2)\eta^2 + 16(\zeta^2 - 1) = 0, \qquad (2.11)$$

which incorporates the unknown $\eta = k_t/k = c_r/c_t$ and the parameter $\zeta = k_l/k_t = c_t/c_l$. Here the $c_l = \sqrt{(\lambda + 2\mu)/\rho}$, $c_t = \sqrt{\mu/\rho}$ shall be understand as the phase velocity of longitudinal and shear wave respectively while $c_r = \omega/k$ is the phase velocity of SAW. This relation is sometime called the Rayleigh equation. It has six roots, the values of which depends on the material parameters λ and μ.

The Rayleigh wave (SAW) corresponds to the root η_r which lies between 0 and 1 such that $|k| > |k_t| > |k_l|$ is confirmed. It can be shown that for any real media Eq. 2.11 has one and only one such root. Note again that the parameters in equation 2.11 does not depends on ω, which means that the solution η_r is simply a constant if the materials parameters is fixed. This leads to the fact that $c_r = \eta_r c_t$ and the dispersion relation,

$$\omega(k) = c_r|k| = \eta_r c_t|k| \qquad (2.12)$$

is of linear dependence. We note the reader that it is the velocity relation $c_r < c_t < c_l$ maintains the wave front of Rayleigh SAW staying on the surface instead of sinking into the bulk because the waves inside the bulk travels faster.

Next putting the potential wave solution Eq. 2.8 into the displacement expression (Eq. 2.2) we have the general Rayleigh acoustic wave profile

$$
\begin{aligned}
u_x &= ik\varphi_k\left(e^{qz} - \frac{2qs}{k^2 + s^2}e^{sz}\right)e^{i(kx - \omega t)}, \\
u_z &= q\varphi_k\left(e^{qz} - \frac{2k^2}{k^2 + s^2}e^{sz}\right)e^{i(kx - \omega t)}.
\end{aligned}
\qquad (2.13)
$$

where φ_k is the normalization factor which shall be defined in later usage. Since the relative phase between $\phi(u_x/u_z)$ changes sign as the direction of propagation is reversed, we call the surface acoustic wave is spin-momentum locked just like a rotating wheel.

2.3. Quantization of the hybrid magnetization and elastic surface system

We consider a rectangular magnetic nanowire (YIG) on top of the surface of a thick dielectric (GGG) that spans the x, y plane. It extends along the y direction with $z \in [0, d]$ and $x \in x_i + [-w/2, w/2]$, as shown in Fig. 2.1. For an analytical treatment, d is assumed to be much smaller than the skin depth of the SAWs, such that the displacement field in the wire is nearly uniform in the z dependence. The lattice and elastic parameters at the YIG|GGG interface match well [15, 18, 19, 28] and are assumed equal. A uniform and sufficiently large static magnetic field $\boldsymbol{H}_0$ along $\vec{x}$ saturates the equilibrium magnetization $M_s \vec{x}$, normal to the wire.

The system Hamiltonian consists of the elastic energy H_e, the magnetic energy H_m, and the magnetoelastic coupling H_c. Firstly according to the Ref. [29] in our setup the magnetic energy of the Kittel mode H_m under the external field $\boldsymbol{H}_0$ is

$$H_m = \mu_0 \int d\boldsymbol{r} \left(-M_x H_0 + \frac{1}{2} N_{xx} M_x^2 + \frac{1}{2} N_{zz} M_z^2 \right), \tag{2.14}$$

where $\boldsymbol{M} = (M_x, M_y. M_z)^T$ is the magnetization vector and the demagnetization constants are taken as $N_{xx} \simeq d/(d+w)$ and $N_{zz} \simeq w/(d+w)$. Here the μ_0 is the vacuum permeability and in the following $\gamma = g\mu_B$ is the gyromagnetic ratio for YIG and is taken as positive constant. Although the predicted effects are classical, we use a quantum description for convenience and future applications in quantum phononics [3–5, 30, 31]; we can always recover the classical picture by replacing operators by amplitudes.

The transverse magnetization is quantized by the Kittel-magnon operator $\hat{\beta}(t)$ with normalized wave function $m_{y,z}$

$$\hat{M}_{y,z} = -\sqrt{2\gamma \hbar M_s} \left(m_{y,z} \hat{\beta}(t) + m_{y,z}^* \hat{\beta}^\dagger(t) \right). \tag{2.15}$$

Similar to the citation [32], the normalized wave function is derived from the criteria that,

$$\int d\boldsymbol{r} \left(m_y m_z^* - m_y^* m_z \right) = -\frac{i}{2}. \tag{2.16}$$

The Landau-Lifshitz equation for the transverse dynamics in our configuration with saturated magnetization along the $\vec{x}$ direction reads

$$\frac{dM_y}{dt} = -\mu_0 \gamma (H_0 - N_{xx} M_s + N_{zz} M_s) M_z,$$
$$\frac{dM_z}{dt} = \mu_0 \gamma (H_0 - N_{xx} M_s) M_y, \tag{2.17}$$

which is solved by

$$m_z = i\xi_M^2 m_y, \tag{2.18}$$

with dimensionless ellipticity

$$\xi_M = \left(\frac{H_0 - N_{xx} M_s}{H_0 - N_{xx} M_s + N_{zz} M_s} \right)^{1/4}. \tag{2.19}$$

With the normalization condition (Eq. 2.16) the magnon amplitudes read

$$m_y = -\frac{1}{2\sqrt{Lwd}}\frac{1}{\xi_M}, \quad m_z = -\frac{i}{2\sqrt{Lwd}}\xi_M.$$ (2.20)

Inserting these wave amplitudes into magnetization operators $\hat{M}_{y,z}$ and further the $\hat{H}_m$ the Hamiltonian of magnetization can be diagonalized into the simple harmonic oscillator form

$$\hat{H}_m = \hbar\omega_F\hat{\beta}^\dagger\hat{\beta},$$ (2.21)

with eigenfrequency $\omega_F = \mu_0\gamma\sqrt{(H_0 - N_{xx}M_s)(H_0 - N_{xx}M_s + N_{zz}M_s)}$.

In our configuration, only the Rayleigh SAWs couple efficiently with the magnet which by their surface nature and long decay length are well suited to exchange information with spatially remote magnets (check the appendix 2.7 to see other acoustic modes damped away). Thus the elastic Hamiltonian which is a sum of the kinetic and potential energy can be represented by the twice of kinetic energy dues to SAW displacement vibration as [31]

$$H_e = \rho\int d\boldsymbol{r}\,\dot{\boldsymbol{u}}^2(x,z,t).$$ (2.22)

The displacement field $(\hat{u}_x, \hat{u}_z)$ can be expanded into the eigenmodes $\boldsymbol{\psi}(k)$ and phonon operators $\hat{b}_k(t)$ [31]

$$\hat{\boldsymbol{u}}(x,z,t) = \sum_k\left[\boldsymbol{\psi}(x,z,k)\hat{b}_k(t) + \boldsymbol{\psi}^*(x,z,k)\hat{b}_k^\dagger(t)\right].$$ (2.23)

In order to properly diagonalize the elastic Hamiltonian, we shall require the Rayleigh wave profile (Eq. 2.13) been normalized as

$$\int_{-\infty}^0 dz(|\psi_x|^2 + |\psi_y|^2) = \frac{\hbar}{2\rho L\omega_k},$$ (2.24)

leading to the normalization factor

$$\varphi_k = \frac{1}{|k|}\frac{1+b^2}{2a(1-b^2)}\sqrt{\frac{2\hbar}{\rho L c_r}}\,\xi_P,$$ (2.25)

where

$$\xi_P = \frac{a(1-b^2)}{1+b^2}\left(\frac{1+a^2}{2a} + \frac{2a(a-2b)}{b(1+b^2)}\right)^{-1/2}$$ (2.26)

with the dimensionless material constants

$$a = \frac{q}{|k|} = \sqrt{1-(c_r/c_l)^2}, \quad b = \frac{s}{|k|} = \sqrt{1-\eta_r^2}.$$ (2.27)

Then the elastic Hamiltonian can be rephrased into second quantization formalism, which as expected, is the sum of harmonic oscillators of different modes

$$\hat{H}_e = \rho\int d\boldsymbol{r}\,\dot{\boldsymbol{u}}^2(x,z,t) = \sum_k\hbar\omega_k\hat{b}_k^\dagger\hat{b}_k.$$ (2.28)

In YIG films, the magnetocrystalline anisotropy is relative week [15, 19] and the magnetoelastic coupling can be simplified from the general expression (Eq. 1.52) by retaining only the linear term of smallness $M_{y,z}/M_s$ that

$$H_c = \frac{B_\perp}{M_s} \int d\boldsymbol{r} \left(M_y \partial_x u_y + M_z \partial_z u_x + M_z \partial_x u_z \right), \tag{2.29}$$

with $B_\perp$ is the shear magnetoelastic coupling constant. The magnetic wire and non-magnetic substrate are coupled by the dynamics of the surface strain. By the translation symmetry along the nanowire y direction, the displacement field excited by the Kittel magnon shall does not depend on y and dues to the arguing in appendix we can focus on the only interaction between the Kittel mode and SAWs which propagate along the x direction. Performing the integration within the magnetic nanowire with length L the coupling Hamiltonian becomes

$$
\begin{aligned}
H_c = {} & \frac{B_\perp L}{M_s} \int_0^d M_z (u_z|_{x=w/2+x_i} - u_z|_{x=-w/2+x_i}) dz \\
& + \frac{B_\perp L}{M_s} \int_{-w/2+x_i}^{w/2+x_i} M_z (u_x|_{z=d} - u_x|_{z=0}) dx.
\end{aligned}
\tag{2.30}
$$

We note that for the generality the nanowire is centered at position x_i. Limited to the realistic situation in which the wire thickness d is much smaller than the decay length of the SAWs into the bulk, the second term of this integral vanishes [11] and in the first term displacements can be treated as universe along the z direction

$$H_c \rightarrow \frac{B_\perp L d}{M_s} M_z \left(u_z|_{x=w/2+x_i} - u_z|_{x=-w/2+x_i} \right). \tag{2.31}$$

From classical aspect the canonical equation based on the coupling Hamiltonian gives the oscillating force applied onto the substrate surface

$$\boldsymbol{F}|_{x=\pm w/2+x_i} = \mp \frac{B_\perp L d M_z}{M_s} \vec{z}$$

which could excite SAW which traveling outwards in both directions. In this research, however, we consist to the second quantization approach and one can refer to the appendix for the classical formula of pumping of surface acoustic wave.

Substituting Eqs 2.15 and 2.31 we arrive at the quantized magnetoelastic coupling Hamiltonian

$$\hat{H}_c = \hbar \sum_k g_k \hat{\beta}^\dagger \hat{b}_k + H.c., \tag{2.32}$$

in which the coupling constant ($qd \ll 1, sd \ll 1$)

$$g_k \simeq -B_\perp \sqrt{\frac{\gamma}{M_s \rho c_r}} \sqrt{\frac{d}{w}} \sin\left(\frac{kw}{2}\right) \xi_M \xi_P e^{ikx_i}. \tag{2.33}$$

The form factor e^{ikx_i} oscillates and tunes the phase of excited SAW which shall play a vital role for multi nanowire presents. We see that the derived coupling strength is reasonable because it vanishes as the nanowire width w and thickness d approaches 0. We also note that such coupling is reciprocal since $|g_k| = |g_{-k}|$.

2.4. Pumping of SAW by the FMR magnetic nanowire

We now calculate the phonon pumping by a single magnetic nanowire transducer centered at x_0. We excite the FMR inside the nanowire by external microwave field which is quantized and represented by the photon operator $\hat{p}_{in}$ as an external input into the magnons' equation of motion. The Hamiltonian $\hat{H} = \hat{H}_m + \hat{H}_e + \hat{H}_c$ leads to the Heisenberg equation of motion [33, 34]

$$
\begin{aligned}
\frac{d\hat{\beta}}{dt} &= -i[\hat{\beta}, \hat{H}] = -i\omega_F \hat{\beta} - i\sum_k |g_k| e^{ikx_0} \hat{b}_k - (\kappa_m + \kappa_w)\frac{\hat{\beta}}{2} - \sqrt{\kappa_w}\,\hat{p}_{\text{in}}, \\
\frac{d\hat{b}_k}{dt} &= -i[\hat{b}_k, \hat{H}] = -i\omega_k \hat{b}_k - i|g_k| e^{-ikx_0} \hat{\beta} - \delta_k \frac{\hat{b}_k}{2}.
\end{aligned}
\tag{2.34}
$$

Here κ_m and δ_k are the intrinsic damping rates for the nanowire magnons and surface phonons, while the κ_w is the radiative damping induced by the contact with microwave field. This equation of motion can be solved by the Fourier transformation

$$
\hat{\mathcal{O}}(\omega) = \int dt\, \hat{\mathcal{O}}(t) e^{i\omega t},
$$

that

$$
\begin{aligned}
\hat{\beta}(\omega) &= \frac{-i\sqrt{\kappa_w}\,\hat{p}_{in}}{\omega - \omega_F + i(\kappa_m + \kappa_w)/2 - \sum_k |g_k|^2 G_k(\omega)}, \\
\hat{b}_k(\omega) &= G_k(\omega)|g_k| e^{-ikx_0} \hat{\beta}(\omega),
\end{aligned}
\tag{2.35}
$$

where

$$
G_k(\omega) = \frac{1}{\omega - \omega_k + i\delta_k/2}
\tag{2.36}
$$

is the phonon's Green function. From the expression of $\hat{\beta}(\omega)$ we see the additional magnetic damping dues to the phonon pumping at the FMR is given by the imaginary part of the magnon's self-energy [15, 35]

$$
\sigma_{k_r} = -\text{Im}\left(\sum_k |g_k|^2 G_k(\omega_F)\right) = \frac{|g_{k_r}|^2}{c_r},
\tag{2.37}
$$

where we have used the Sokhotski–Plemelj approximation,

$$
\lim_{\epsilon \to 0^+} \frac{1}{x \pm i\epsilon} = \mp i\pi\delta(x) + P\left(\frac{1}{x}\right),
\tag{2.38}
$$

with $\omega \to \omega_F$ and $k_r = \omega_F/c_r$. The real part of the self-energy causes a small frequency shift which is absorbed into ω_F and shall be neglected in the following analysis.

The displacement field given by Eq. 2.23 is a superposition of coherent phonon $\langle \hat{b}_k \rangle$ that are excited by the microwave input $\langle \hat{p}_{in}(\omega) \rangle$. At resonance frequency $\omega = \omega_F$, the contour of the k integral must be closed in the upper (lower) half of the complex plane for $x > x_0$ ($x < x_0$), selecting the poles $k_r + i\epsilon$ ($-k_r - i\epsilon$) in the denominator, where ϵ is

2

the inverse of the phonon propagation length. The low ultrasonic attenuation in GGG at room temperature corresponds to characteristic SAW decay lengths of up to 6 mm [18]. We can therefore safely disregard the phonon damping by setting $\epsilon \to 0_+$, which leads to the displacement fields

$$\boldsymbol{u}(t) = -\frac{1}{c_r} \begin{cases} i\psi(k_r)g^*_{k_r}\langle\hat{\beta}(t)\rangle + H.c., & x > x_0 \\ i\psi(-k_r)g^*_{-k_r}\langle\hat{\beta}(t)\rangle + H.c., & x < x_0 \end{cases} \tag{2.39}$$

On the right (left) side of the nanowire $x > x_0$ ($x < x_0$), the right- and left-propagating waves possess opposite rotations whose directions depends on z are pumped as illustrated schematically in Fig. 2.1. We point out that a classical treatment for the SAW pumping shown in the appendix 2.7 leads to exactly the same results as in Eq. 2.39.

In recent literature such as Ref. [16, 36] the mechanical angular momentum is often referred as phonon spins defined as $\boldsymbol{l} = \rho\langle\boldsymbol{u}\times\dot{\boldsymbol{u}}\rangle_t$, where the subscript t indicates time average. According to a recent PNAS paper [36], such phonon spin can be calculated in operator form, which is similar to the electron spin but with the *state vector* identified with the normalized displacement of (x, y, z) directions, i.e. $\boldsymbol{l} = \langle\boldsymbol{u}|\hat{\boldsymbol{l}}|\boldsymbol{u}\rangle$ with

$$\hat{l}_x = -i\begin{pmatrix} 0 & 0 & 0 \\ 0 & 0 & 1 \\ 0 & -1 & 0 \end{pmatrix}, \quad \hat{l}_y = -i\begin{pmatrix} 0 & 0 & -1 \\ 0 & 0 & 0 \\ 1 & 0 & 0 \end{pmatrix}, \quad \hat{l}_z = -i\begin{pmatrix} 0 & 1 & 0 \\ -1 & 0 & 0 \\ 0 & 0 & 0 \end{pmatrix}, \tag{2.40}$$

and the state vector $|\boldsymbol{u}\rangle = \sqrt{\rho\omega/2}\,(u_x, u_y, u_z)^T$. Thus the pumped SAW possess a constant elastic spin into the y-direction as

$$\boldsymbol{l}(z) = \vec{y}\frac{4\rho\omega_F}{c_r^2}|\langle\hat{\beta}\rangle|^2|g_{k_r}|^2 \times \text{Im}\begin{cases} \psi_x(k_r,z)\psi_z^*(k_r,z), & x > x_0 \\ \psi_x(-k_r,z)\psi_z^*(-k_r,z), & x < x_0 \end{cases} \tag{2.41}$$

We see that $\boldsymbol{l}$ is proportional to the excited magnon population and opposite on each side of the nanowire since $\psi_x(-k)\psi_z^*(-k) = -\psi_x(k)\psi_z^*(k)$. Into the substrate ($-z$ direction), the SAW eigenmodes have a node at which $\boldsymbol{l}$ changes sign as sketch in Fig. 2.1. We point out that the phonon pumping does not remove angular momentum from the ferromagnet since only the x component of the magnetic precession is damped. The force on the interface is a superposition of opposite angular momenta $2\vec{z} = (\vec{z} + i\vec{x}) + (\vec{z} - i\vec{x})$ that by the spin-momentum locking couples to the phonon moving in opposite directions.

We show the efficiency of surface acoustic wave pumping by applying the YIG|GGG material parameters at room temperature. For GGG, it density is $\rho = 7080$ kg/m^3 and bulk acoustic velocity $c_l = 6545$ m/s, $c_t = 3531$ m/s [37], leading to the Rayleigh parameter $\eta_r = 0.927$, $c_r = \eta_r c_t = 3271.8$ m/s, and $\xi_P = 0.537$. For the YIG, its gyromagnetic ratio and saturated magnetization is $\gamma = 1.82 \times 10^{11}$ s^{-1}T^{-1} and $\mu_0 M_s = 0.177$ T [38]. The $B_\perp = 6.96 \times 10^5$ J/m^3 [15] and $\xi_M \approx 1$ when H_0 is comparable to M_s. We plot the pumped phonon spin density at different depths of $z = 0$ and $z = -1.5\,\mu$m in Fig. 2.2(a) with typical FMR frequency $\omega_F = 3$ GHz and setting the nanowire thickness and width as $d = 200$ nm and $w = 2.5\,\mu$m respectively. We see that the spin density is opposite at two sides of the nanowire and changes sign at large depth. The tiny damping along the
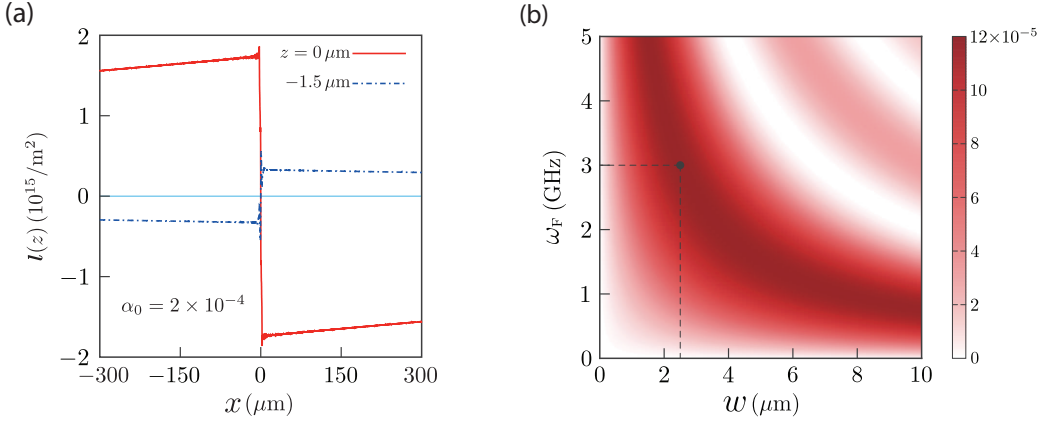
Figure 2.2: Pumped phonon spin density (a) and additional magnon damping coefficient $\alpha_R = \sigma_{k_r}/\omega_F$ (b) for a YIG wire on a GGG substrate as function of FMR frequencies and wire widths.

propagation matches with the good quality factor of GGG substrate as acoustic material. Figure 2.2(b) is a plot of the additional magnon damping coefficient $\alpha_R = \sigma_{k_r}/\omega_F$ in the dependence of FMR frequency ω_F and nanowire width w. We observe periodic geometric effect dues to the $\frac{1}{w}\sin(kw/2)$ factor in the coupling strength. The calculated $\alpha_R \approx 10^{-4}$ is of the order of the intrinsic Gilbert damping for YIG single crystals $\alpha_0 = 4 \times 10^{-5}$ and films $\alpha_0 = 8 \times 10^{-5}$.

2.5. The chiral phonon pumping through two parallel nanowire

In previous section the single wire emits spin-momentum locked SAWs into two directions. Here we propose a truly unidirectional phonon source in the form of two parallel and identical nanowires located at $\boldsymbol{r}_1 = R_1\vec{x}$ and $\boldsymbol{r}_2 = R_2\vec{x}$ of which only the left one is addressed by a local microwave strip line. The excited phonons on the substrate surface propagate to and are then absorbed by the second nanowire whose dynamics re-emits phonons that subsequently interfere with the original ones. Such case is similar to the setup used in Ref. [18] but with the modification from bulk acoustic wave into the surface one.

Denoting the Kittel-magnon operators in the left and right nanowire as $\hat{\beta}_L$ and $\hat{\beta}_R$ and assume $R_1 < R_2$, the Heisenberg equations of motion for the magnon-phonon coupled system (including the microwave source and various dissipation) read

$$\frac{d\hat{\beta}_L}{dt} = -i\hbar\omega_F\hat{\beta}_L(t) - i\hbar\sum_k |g_k|e^{ikR_1}\hat{b}_k(t) - \left(\frac{\kappa_L + \kappa_{w,L}}{2}\right)\hat{\beta}_L(t) - \sqrt{\kappa_{w,L}}\,\hat{p}_{\text{in}}^L(t),$$

$$\frac{d\hat{\beta}_R}{dt} = -i\hbar\omega_F\hat{\beta}_R(t) - i\hbar\sum_k |g_k|e^{ikR_2}\hat{b}_k(t) - \frac{\kappa_R}{2}\hat{\beta}_R(t), \qquad (2.42)$$

$$\frac{d\hat{b}_k}{dt} = -i\hbar\omega_k\hat{b}_k(t) - i\hbar|g_k|e^{-ikR_1}\hat{\beta}_L(t) - i\hbar|g_k|e^{-ikR_2}\hat{\beta}_R(t) - \frac{\delta_k}{2}\hat{b}_k(t).$$

As in previous here the κ_L and κ_R denote the intrinsic (Gilbert) damping of the Kittel

2

modes in the left and right nanowire, and $\kappa_{w,L}$ is the radiative coupling of the left wire to the microwave source. For sufficient large distance $|R_2 - R_1|$ (tens of micrometers for the present system), the excited magnon and phonon operators in frequency space read

$$\hat{\beta}_L(\omega) = \frac{-i\sqrt{\kappa_{w,L}}}{\omega - \omega_F + i\frac{\kappa_L + \kappa_{w,L}}{2} - \sum_k |g_k|^2 G_k(\omega) - f(\omega)} \hat{p}_{\text{in}}^L(\omega),$$

$$\hat{\beta}_R(\omega) = \frac{\sum_k |g_k|^2 G_k(\omega) e^{ik(R_2 - R_1)}}{\omega - \omega_F + i\kappa_R/2 - \sum_k |g_k|^2 G_k(\omega)} \hat{\beta}_L(\omega), \tag{2.43}$$

$$\hat{b}_k(\omega) = |g_k| G_k(\omega) \left(e^{-ikR_1} \hat{\beta}_L(\omega) + e^{-ikR_2} \hat{\beta}_R(\omega) \right),$$

where

$$f(\omega) = \frac{\left(|g_k|^2/c_r \right)^2 e^{i2\omega(R_2 - R_1)/c_r}}{\omega - \omega_F + i\kappa_R/2 - \sum_k |g_k|^2 G_k(\omega)}, \tag{2.44}$$

and $G_k(\omega)$ is the phonon's Green function as in Eq. 2.36.

At the FMR $\omega \to \omega_F$ then

$$\hat{\beta}_R(\omega_F) = \chi(k_r) e^{i\pi + ik_r(R_2 - R_1)} \hat{\beta}_L(\omega_F), \tag{2.45}$$

with the ratio $\chi(k_r) = \sigma_{k_r}/(\kappa_m/2 + \sigma_{k_r})$ modulates the magnetization amplitude in the second wire. The $k_r(R_2 - R_1)$ is the usual phase delay by the phonon transmission and the phase shift of π reflects the dynamical phase relation between magnons and phonons which is the key factor for unidirectionality. By substituting the magnon relation (Eq. 2.45) back into the phonon's solution (Eq. 2.43) we arrived at the phonon's amplitude for the left and right going wave respectively

$$\hat{b}_{-k_r} = |g_{k_r}| G_{k_r} e^{ik_r R_1} \hat{\beta}_L(\omega_F) \left[1 - \chi(k_r) e^{i2k_r(R_2 - R_1)} \right],$$

$$\hat{b}_{k_r} = |g_{k_r}| G_{k_r} e^{-ik_r R_1} \hat{\beta}_L(\omega_F) \left[1 - \chi(k_r) \right]. \tag{2.46}$$

In the strong magnon-phonon coupling limit $\sigma_{k_r} \gg \kappa_m/2$ leading to $\chi(k_r) \to 1$, thus the right-going phonon ($k_r > 0$) is not excited by the double-wire configuration. Finite $\langle \hat{b}_{-k_r} \rangle$ by vanishing $\langle \hat{b}_{k_r} \rangle$ implies a unidirectional phonon current. Such unidirectionality vanishes when the second wire is weakly coupled to the SAW, i.e., $\sigma_{k_r} \ll \kappa_m/2$, that is the phonon transmits through without interacting with the magnet.

By Eqs. 2.23 and 2.46, the displacement fields at the FMR frequency ω_F read

$$\boldsymbol{u} = \frac{2|g_{k_r}|}{c_r} \text{Im} \begin{cases} \boldsymbol{\psi}(-k_r) e^{ik_r R_1} \langle \hat{\beta}_L(t) \rangle \left[1 - \chi(k_r) e^{i2k_r(R_2 - R_1)} \right], & x < R_1 \\ e^{ik_r(R_2 - R_1)} \langle \hat{\beta}_L(t) \rangle \left[\boldsymbol{\psi}(k_r) e^{-ik_r R_2} - \chi(k_r) \boldsymbol{\psi}(-k_r) e^{ik_r R_2} \right], & R_1 < x < R_2 \\ \boldsymbol{\psi}(k_r) e^{-ik_r R_1} \langle \hat{\beta}_L(t) \rangle \left[1 - \chi(k_r) \right], & x > R_2 \end{cases}. \tag{2.47}$$

As we see when $\chi(k_r) \to 1$, the displacement field indeed vanishes in the region $x > R_2$ but is a traveling wave for $x < R_1$ whose amplitude depends on the geometry phase $e^{i2k_r(R_2 - R_1)}$. Between the two nanowire with $R_1 < x < R_2$ the SAW form standing wave with $u_z \sim \sin k_r(x - R_2)$ and $u_x \sim \cos k_r(x - R_2)$. The pumping is unidirectional apart from special cases with frequency or distance that $k_r(R_2 - R_1) = n\pi$ with $n \in \mathbb{Z}_0$, in which

(a)

(b)
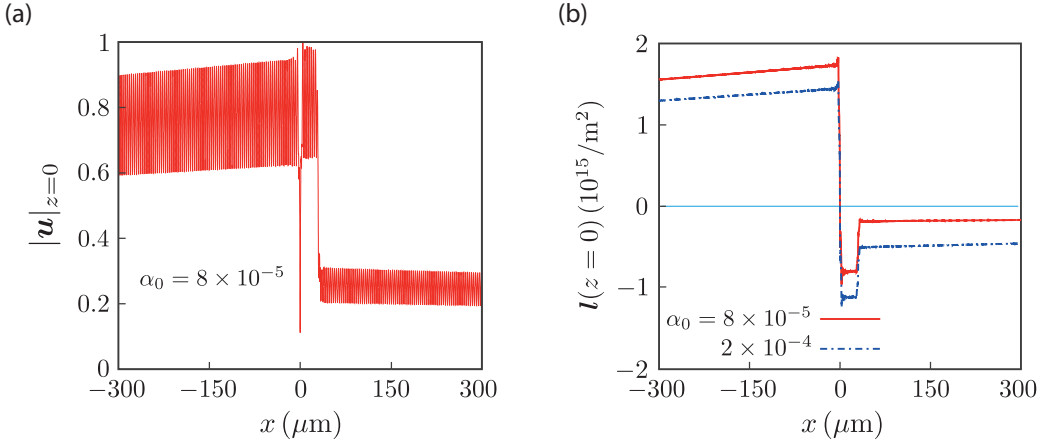
Figure 2.3: Snapshot of the displacement field at the GGG surface $|\boldsymbol{u}|$ (a) and phonon spin density (b), pumped by a YIG wire at the origin under FMR and modulated by a second YIG wire at $30\,\mu\text{m}$ sitting to the right.

case the SAW on the left-hand side vanishes as well and the phonon is fully trapped between the two wires to form a cavity. The phonon emission is not perfectly unidirectional when $\chi(k_r) < 1$. As in Fig. 2.3(a) is a plot of the magnitude of the displacement field at the GGG surface $|\boldsymbol{u}|_{z=0} = \sqrt{u_x^2 + u_z^2}\Big|_{z=0}$ with the intrinsic Gilbert damping in YIG $\alpha_0 = 8 \times 10^{-5}$. We choose the two wires centered at $R_1 = 0$ and $R_2 = 30\,\mu\text{m}$ respectively, and $d = 200\,\text{nm}$, $w = 2.5\,\mu\text{m}$ as previous. The FMR frequency is set to be $\omega_F = 3\,\text{GHz}$ such that the additional damping coefficient is $\alpha_R = 1.2 \times 10^{-4}$. In Fig. 2.3(b) we plot the phonon spin density on the surface for distance far away from the nanowires. The asymmetry of the pumped phonon spin at the two sides of cavity is not perfect, but clearly shows a strong non-reciprocal property contrary to the case of single nanowire.

Another experimentally measurable quantity which inductively shows the resonant cavity feature is the microwave transmission spectra. The microwave output of the left and right nanowires is detected by striplines represented by photon operator $\hat{p}_{\text{out}}^L$ and $\hat{p}_{\text{out}}^R$ that are related by the input-output relations [33, 34]

$$\begin{aligned}
\hat{p}_{\text{out}}^L(\omega) &= \hat{p}_{\text{in}}^L(\omega) + \sqrt{\kappa_{w,L}}\,\hat{\beta}_L(\omega), \\
\hat{p}_{\text{out}}^R(\omega) &= \sqrt{\kappa_{w,R}}\,\hat{\beta}_R(\omega).
\end{aligned} \tag{2.48}$$

The microwave reflection (S_{11}) and transmission (S_{21}) spectra become

$$\begin{aligned}
S_{11}(\omega) &= \frac{\hat{p}_{\text{out}}^L}{\hat{p}_{\text{in}}^L} = 1 - \frac{i\kappa_{w,L}}{\omega - \omega_F + i(\kappa_L + \kappa_{w,L})/2 - \sum_k |g_k|^2 G_k(\omega) - f(\omega)}, \\
S_{21}(\omega) &= \frac{\hat{p}_{\text{out}}^R}{\hat{p}_{\text{in}}^L} = (S_{11}(\omega) - 1)\sqrt{\frac{\kappa_{w,R}}{\kappa_{w,L}}}\,\frac{\sum_k |g_k|^2 G_k(\omega) e^{ik(R_2 - R_1)}}{\omega - \omega_F + i\kappa_R/2 - \sum_k |g_k|^2 G_k(\omega)}.
\end{aligned} \tag{2.49}$$

When the two magnetic nanowires are assumed to be identical, the microwave transmis-

2
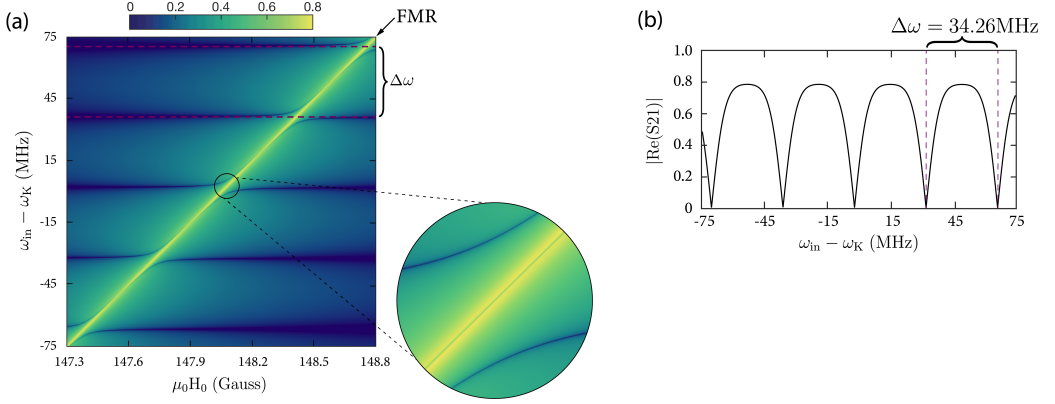
Figure 2.4: Microwave transmission ($|\text{Re}S_{21}|$) between two YIG nanowire transducers on top of a GGG substrate. (a) The minima in the transmission (black contour) anticross with the ω_F near regularly spaced frequencies ω_n. (b) Transmission spectra along the FMR resonance line. Note that the transmission dips originate from the think black contour hidden within the FMR peaks (yellow region) shown in the magnified insert.

sion with excitation (input) at R_1 and detection (output) at R_2 which is

$$S_{21}(\omega) = (S_{11}(\omega) - 1) \frac{\langle \hat{\beta}_R(\omega) \rangle}{\langle \hat{\beta}_L(\omega) \rangle}, \qquad (2.50)$$

can measure the phase relation between the Kittel modes at FMR in the two wire as

$$S_{21}(\omega_F) = (1 - S_{11}(\omega_F)) \chi(k_r) e^{ik_r(R_2 - R_1)}. \qquad (2.51)$$

At the special microwave frequencies $\omega_F = \omega_n = \pi c_r(n + 1/2)/(R_2 - R_1)$, where $n \in \mathbb{Z}_0$, $S_{11}(\omega_F)$ is real while the phase factor $e^{ik_r(R_2 - R_1)} = i(-1)^n$ becomes purely imaginary then $\text{Re}S_{21}(\omega_n) = 0$ develops the minima.

  We plot the real part of the transmission amplitude in Fig. 2.4(a) as a function of microwave frequency closed to $\omega_K = 3\,\text{GHz}$ and static magnetic field H_0. The parameters are chosen the same as in previous and the radiative damping as $\kappa_w = 1\,\text{MHz}$. The dips in the transmission are traced by the black contours and the horizontal dash line correspond to the special frequencies ω_n. Due to the magnon-phonon coupling, these horizontal lines are deformed to the anti-crossing shape when $\omega_F \to \omega_n$. The transmission dips are shown more vivid alone the FMR resonance line as in Fig. 2.4(b). For $R_2 - R_1 = 300\,\mu\text{m}$ the frequency space between these dips is $\Delta\omega = \pi c_r/(R_2 - R_1) = 34.26\,\text{MHz}$ which matches exactly to the gap of horizontal dash lines.

2.6. Summary and outlook

In conclusion, we developed a theory for pumping SAWs based on the magnetoelastic coupling and proposed a phonon cavity device that realizes unidirectional phonon current in a reciprocal system. When exciting a single magnetic nanowire by microwaves, we predict an additional passive wire could induce the unidirectional phonon current

and formation of standing waves in the region between two magnetic nanowires. Devices with more than two wires or made from magnetic materials with larger magnetoelastic coupling may achieve full unidirectionality. Here the unidirectionality emerges from a dynamical phase shift, rather than the purely geometrical interference employed by electrical unidirectional SAW generators [23].

The pumped phonon can propagate coherently over millimeters on the substrate surface, which is very promising for classical and quantum transport of spin information. It can be measured by Brillouin light scattering [16] and/or the spin-rotation coupling by fabricating a conductor on top of the acoustic medium [13, 14]. Such a generation of unidirectionality from interference does not require a nonreciprocal coupling mechanism but only an out-of-phase relation of the two fields at resonance. The phenomenon should be universal for many field propagation phenomena, such as exchange coupled magnetic nanowires and films and reciprocally coupled magnons and waveguide photons.

2.7. Appendix: Classical formalism for SAW pumping

In this appendix we calculate in classical formulation the excitation of Rayleigh SAW by the oscillating surface force

$$\boldsymbol{F}|_{x=\pm w/2+x_i} = \mp \frac{B_\perp L d M_z}{M_s} \vec{z},\tag{2.52}$$

which arises from the magnetoelastic coupling Hamiltonian (Eq. 2.31). We shows that the classical results matches exactly to the quantum mechanical calculation and explains the reason that we ignore other branches of acoustic modes but leaving only the surface modes into consideration.

The boundary conditions for the stress tensor (line load) reads

$$\sigma_{zz}|_{z=0_-} = \frac{1}{L}\frac{dF}{dx} \simeq -\frac{B_\perp d}{M_s} M_z \left[\delta\left(x - \left(\frac{w}{2} + x_i\right)\right) - \delta\left(x - \left(-\frac{w}{2} + x_i\right)\right)\right],$$
$$\sigma_{xz}|_{z=0_-} = 0.\tag{2.53}$$

The displacement field can be written as $\boldsymbol{u} = \nabla V + \nabla \times \boldsymbol{A}$, with vector potential $\boldsymbol{A} = A\vec{y}$ for omitting the $\vec{y}$'s dependency of displacement. For isotropic material and using the stiffness relation, one can solve the elastic equation of motion (Eq. 2.7) with these conditions by a plane-wave ansatz (dropping the explicit time harmony) [27]

$$V = \int_{-\infty}^{\infty} \mathcal{V}(k) e^{i\left(kx + \sqrt{k_l^2 - k^2}\, z\right)} dk,$$
$$A = \int_{\infty}^{\infty} \mathcal{A}(k) e^{i\left(kx + \sqrt{k_t^2 - k^2}\, z\right)} dk.\tag{2.54}$$

With the Fourier transformation of the boundary condition

$$\sigma_{zz}(k)|_{z=0_-} = i\frac{f_z}{\pi}\sin(kw/2)e^{-ikx_i} \qquad \sigma_{xz}(k)|_{z=0_-} = 0,\tag{2.55}$$

2

where $f_z = (B_\perp d/M_s)M_z$, we find the excited elastic potential in k-space is given by

$$\mathcal{V}(k) = i\frac{f_z}{\pi\mu}\frac{2k^2 - k_t^2}{F(k)}\sin(kw/2)\,e^{-ikx_i},$$

$$\mathcal{A}(k) = -\frac{f_z}{\pi\mu}\frac{2k\sqrt{k^2 - k_l^2}}{F(k)}\sin(kw/2)\,e^{-ikx_i}, \tag{2.56}$$

and

$$F(k) = (2k^2 - k_t^2)^2 - 4k^2\sqrt{k^2 - k_l^2}\sqrt{k^2 - k_t^2}. \tag{2.57}$$

Then the displacement field on the substrate surface ($z = 0$) reads

$$u_x|_{z=0} = -\frac{f_z}{\pi\mu}\int_{-\infty}^{\infty}\frac{k\sin(kw/2)}{F(k)}\left[(2k^2 - k_t^2) - 2\sqrt{k^2 - k_l^2}\sqrt{k^2 - k_t^2}\right]e^{ik(x-x_i)}\,dk,$$

$$u_z|_{z=0} = -\frac{if_z k_t^2}{\pi\mu}\int_{-\infty}^{\infty}\frac{\sqrt{k^2 - k_l^2}\sin(kw/2)}{F(k)}e^{ik(x-x_i)}\,dk. \tag{2.58}$$

For locations far away from the nanowire, i.e. $|x - x_i| \gg w$, this integral can be performed analytically by resorting to the complex contour integral (see Fig. 2.5). Taking the root of equation $F(k_r) = 0$ (Rayleigh equation) as singularity and also note the $\pm k_l$ and $\pm k_t$ as branching point, one can solve this integration by choosing proper contour according to the case $x > x_i$ or $x < x_i$. In addition we apply the Watson's lemma for the asymptotic treatment of integration along the branch cuts, leading to the results of displacement field on the substrate surface ($z = 0$)

$$u_x^\pm|_{z=0} = \pm\frac{if_z}{2\mu}\frac{(1 - b^2)}{-4 + (1 + b^2)\left[1 + \frac{1}{2}(\frac{1}{a^2} + \frac{1}{b^2})\right]}\sin\left(\frac{k_r w}{2}\right)e^{\pm ik_r(x-x_i)}$$

$$\pm\frac{2f_z e^{-i\frac{\pi}{4}}}{\mu}\sqrt{\frac{2}{\pi}}\sqrt{\frac{a^2 - b^2}{1 - b^2}}\left[\frac{(1 - a^2)^{\frac{1}{2}}(1 - b^2)^{\frac{3}{2}}}{(1 + b^2 - 2a^2)^3}\sin\left(\frac{k_l w}{2}\right)\frac{e^{\pm ik_l(x-x_i)}}{[k_l(x - x_i)]^{3/2}} + \sin\left(\frac{k_t w}{2}\right)\frac{e^{\pm ik_t(x-x_i)}}{[k_t(x - x_i)]^{3/2}}\right]$$

$$+ \mathcal{O}(kx)^{-\frac{5}{2}},$$

$$u_z^\pm|_{z=0} = -\frac{f_z}{\mu}\frac{a(1 - b^2)}{(1 + b^2)\left[-4 + (1 + b^2)[1 + \frac{1}{2}(\frac{1}{a^2} + \frac{1}{b^2})]\right]}\sin\left(\frac{k_r w}{2}\right)e^{\pm ik_r(x-x_i)}$$

$$\pm\frac{f_z e^{i\frac{\pi}{4}}}{\mu}\sqrt{\frac{2}{\pi}}\left[\frac{(1 - a^2)(1 - b^2)}{(1 + b^2 - 2a^2)^2}\sin\left(\frac{k_l w}{2}\right)\frac{e^{\pm ik_l(x-x_i)}}{[k_l(x - x_i)]^{3/2}} + \frac{4(a^2 - b^2)}{1 - b^2}\sin\left(\frac{k_t w}{2}\right)\frac{e^{\pm ik_t(x-x_i)}}{[k_t(x - x_i)]^{3/2}}\right]$$

$$+ \mathcal{O}(kx)^{-\frac{5}{2}}. \tag{2.59}$$

Here the $'\pm'$ sign stands for the right and left going wave which exist on the right and left side of nanowire respectively. One see that the bulk plane wave, including the longitudinal $e^{ik_l(x-x_i)}$ and shear $e^{ik_t(x-x_i)}$ type, decaying as $1/[k_l(x - x_i)]^{3/2}$ and $1/[k_t(x - x_i)]^{3/2}$
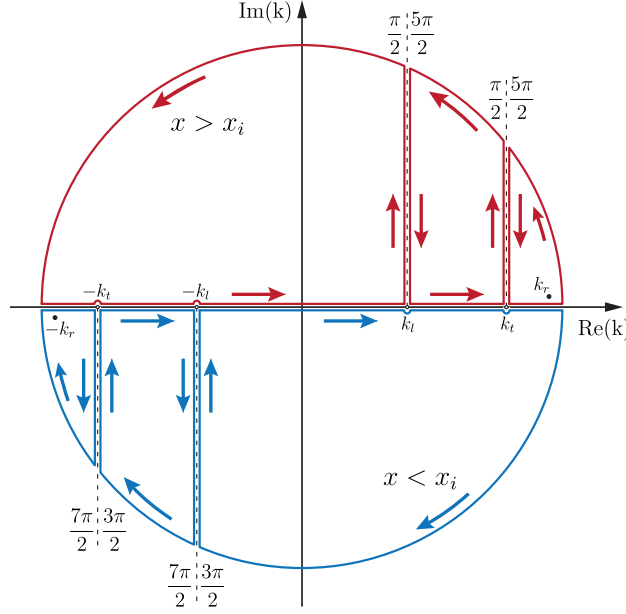
Figure 2.5: Contour in the complex k plane. The upper half plane is used for $x > x_i$ and lower half plane for $x < x_i$. Branch cuts at $\pm k_l$ and $\pm k_t$ are indicated. The Rayleigh points $\pm k_r$ acquires a small imaginary part by causality of sound attenuation.

respectively, leaving only the Rayleigh surface wave $e^{ik_r(x-x_i)}$ at the position tens of micrometers away from the nanowire.

Thus retaining only the SAWs, we find the displacement field from the integral for general z,

$$u_x = -\frac{f_z}{\pi\mu} \int_{-\infty}^{\infty} \frac{k\sin(kw/2)}{F(k)} \left[(2k^2 - k_t^2)\, e^{\sqrt{k^2-k_l^2}\,z} - 2\sqrt{k^2-k_l^2}\sqrt{k^2-k_t^2}\, e^{\sqrt{k^2-k_t^2}\,z} \right] e^{ik(x-x_i)}\, dk,$$

$$u_z = \frac{if_z}{\pi\mu} \int_{-\infty}^{\infty} \frac{\sqrt{k^2-k_l^2}\sin(kw/2)}{F(k)} \left[(2k^2 - k_t^2)\, e^{\sqrt{k^2-k_l^2}\,z} - 2k^2\, e^{\sqrt{k^2-k_t^2}\,z} \right] e^{ik(x-x_i)}\, dk.$$

$$(2.60)$$

We get the Rayleigh surface acoustic wave as

$$u_x^{\pm} = \pm\frac{if_z}{\mu} \frac{1}{-4 + (1+b^2)\left[1 + \frac{1}{2}(\frac{1}{a^2} + \frac{1}{b^2})\right]} \sin\left(\frac{k_r w}{2}\right) \left[e^{qz} - \frac{2ab}{1+b^2} e^{sz} \right] e^{\pm ik_r(x-x_i)},$$

$$u_z^{\pm} = \frac{f_z}{\mu} \frac{a}{-4 + (1+b^2)\left[1 + \frac{1}{2}(\frac{1}{a^2} + \frac{1}{b^2})\right]} \sin\left(\frac{k_r w}{2}\right) \left[e^{qz} - \frac{2}{1+b^2} e^{sz} \right] e^{\pm ik_r(x-x_i)}.$$

$$(2.61)$$

Inserting the force term $f_z = (B_\perp d/M_s)\hat{M}_z$ and the expression of $\hat{M}_z$ in the main text, we

arrived at the final expression of excited displacement fields

$$
\begin{aligned}
u_x^{\pm} &= \mp \frac{B_{\perp} \xi_M \xi_P}{\rho c_r^2} \sqrt{\frac{2\hbar \gamma d}{L w M_s}} \frac{\xi_P}{1-b^2} \sin\left(\frac{k_r w}{2}\right) \left[e^{qz} - \frac{2ab}{1+b^2} e^{sz} \right] e^{\pm i k_r (x-x_i)} \langle \hat{\beta}(t) \rangle \\
&= -\frac{1}{c_r} i \psi_x(\pm k_r) g_{\pm k_r}^* \langle \hat{\beta}(t) \rangle, \\
u_z^{\pm} &= \frac{i B_{\perp} \xi_M \xi_P}{\rho c_r^2} \sqrt{\frac{2\hbar \gamma d}{L w M_s}} \frac{a \xi_P}{1-b^2} \sin\left(\frac{k_r w}{2}\right) \left[e^{qz} - \frac{2}{1+b^2} e^{sz} \right] e^{\pm i k_r (x-x_i)} \langle \hat{\beta}(t) \rangle \\
&= -\frac{1}{c_r} i \psi_z(\pm k_r) g_{\pm k_r}^* \langle \hat{\beta}(t) \rangle,
\end{aligned}
\tag{2.62}
$$

in which we used the Rayleigh relation $4ab = (1 + b^2)^2$. These final results exactly reproduce the displacement expression we derived in the main text through the quantum formalism (Eq. 2.39).

References

[1] X. Zhang, G. E. W. Bauer, and T. Yu, *Unidirectional pumping of phonons by magnetization dynamics,* Phys. Rev. Lett. **125**, 077203 (2020).

[2] A. A. Oliner, *Acoustic surface waves (Topics in applied physics)* (Springer, 2014).

[3] M. V. Gustafsson, T. Aref, A. F. Kockum, M. K. Ekström, G. Johansson, and P. Delsing, *Propagating phonons coupled to an artificial atom,* Science **346**, 207 (2014).

[4] K. J. Satzinger, Y. P. Zhong, H.-S. Chang, G. A. Peairs, A. Bienfait, M.-H. Chou, and *et al*, *Quantum control of surface acoustic-wave phonons,* Nature **563**, 661 (2018).

[5] D. A. Golter, T. Oo, M. Amezcua, I. Lekavicius, K. A. Stewart, and H. Wang, *Coupling a surface acoustic wave to an electron spin in diamond via a dark state,* Phys. Rev. X **6**, 041060 (2016).

[6] P. Delsing, A. N. Cleland, M. J. A. Schuetz, J. Knörzer, G. Giedke, J. I. Cirac, and *et al*, *The 2019 surface acoustic waves roadmap,* Journal of Physics D: Applied Physics **52**, 353001 (2019).

[7] Y. Yahagi, B. Harteneck, S. Cabrini, and H. Schmidt, *Controlling nanomagnet magnetization dynamics via magnetoelastic coupling,* Phys. Rev. B **90**, 140405 (2014).

[8] M. Weiler, L. Dreher, C. Heeg, H. Huebl, R. Gross, M. S. Brandt, and S. T. B. Goennenwein, *Elastically driven ferromagnetic resonance in nickel thin films,* Phys. Rev. Lett. **106**, 117601 (2011).

[9] L. Dreher, M. Weiler, M. Pernpeintner, H. Huebl, R. Gross, M. S. Brandt, and S. T. B. Goennenwein, *Surface acoustic wave driven ferromagnetic resonance in nickel thin films: Theory and experiment,* Phys. Rev. B **86**, 134415 (2012).

[10] R. Sasaki, Y. Nii, Y. Iguchi, and Y. Onose, *Nonreciprocal propagation of surface acoustic wave in niⱡinbo₃,* Phys. Rev. B **95**, 020407 (2017).

[11] J. Puebla, M. Xu, B. Rana, K. Yamamoto, S. Maekawa, and Y. Otani, *Acoustic ferromagnetic resonance and spin pumping induced by surface acoustic waves,* Journal of Physics D: Applied Physics **53**, 264002 (2020).

[12] I. Lisenkov, A. Jander, and P. Dhagat, *Magnetoelastic parametric instabilities of localized spin waves induced by traveling elastic waves,* Phys. Rev. B **99**, 184433 (2019).

[13] M. Matsuo, J. Ieda, K. Harii, E. Saitoh, and S. Maekawa, *Mechanical generation of spin current by spin-rotation coupling,* Phys. Rev. B **87**, 180402 (2013).

[14] D. Kobayashi, T. Yoshikawa, M. Matsuo, R. Iguchi, S. Maekawa, E. Saitoh, and Y. Nozaki, *Spin current generation using a surface acoustic wave generated via spin-rotation coupling,* Phys. Rev. Lett. **119**, 077202 (2017).

[15] S. Streib, H. Keshtgar, and G. E. W. Bauer, *Damping of magnetization dynamics by phonon pumping,* Phys. Rev. Lett. **121**, 027202 (2018).

[16] J. Holanda, D. S. Maior, A. Azevedo, and S. M. Rezende, *Detecting the phonon spin in magnon–phonon conversion experiments,* Nature Physics **14**, 500 (2018).

[17] C. Berk, M. Jaris, W. Yang, S. Dhuey, S. Cabrini, and H. Schmidt, *Strongly coupled magnon–phonon dynamics in a single nanomagnet,* Nature Communications **10**, 2652 (2019).

[18] K. An, A. N. Litvinenko, R. Kohno, A. A. Fuad, V. V. Naletov, L. Vila, U. Ebels, and *et al*, *Coherent long-range transfer of angular momentum between magnon kittel modes by phonons,* Phys. Rev. B **101**, 060407 (2020).

[19] A. Rückriegel and R. A. Duine, *Long-range phonon spin transport in ferromagnet–nonmagnetic insulator heterostructures,* Phys. Rev. Lett. **124**, 117201 (2020).

[20] K. S. Das, J. Liu, B. J. van Wees, and I. J. Vera-Marun, *Efficient injection and detection of out-of-plane spins via the anomalous spin hall effect in permalloy nanowires,* Nano Letters **18**, 5633 (2018).

[21] L. J. Cornelissen, J. Liu, R. A. Duine, J. B. Youssef, and B. J. van Wees, *Long-distance transport of magnon spin information in a magnetic insulator at room temperature,* Nature Physics **11**, 1022 (2015).

[22] J. Chen, C. Liu, T. Liu, Y. Xiao, K. Xia, G. E. W. Bauer, M. Wu, and H. Yu, *Strong interlayer magnon-magnon coupling in magnetic metal-insulator hybrid nanostructures,* Phys. Rev. Lett. **120**, 217202 (2018).

[23] P. Ventura, M. Solal, P. Dufilie, J. M. Hode, and F. Roux, *A new concept in SPUDT design: the RSPUDT (resonant SPUDT),* in *1994 Proc. of IEEE Ultrasonics Symposium,* Vol. 1 (1994) pp. 1–6 vol.1.

2

2

[24] R. Camley, *Nonreciprocal surface waves,* Surface Science Reports **7**, 103 (1987).

[25] R. Verba, I. Lisenkov, I. Krivorotov, V. Tiberkevich, and A. Slavin, *Nonreciprocal surface acoustic waves in multilayers with magnetoelastic and interfacial dzyaloshinskii-moriya interactions,* Phys. Rev. Applied **9**, 064014 (2018).

[26] R. Verba, V. Tiberkevich, and A. Slavin, *Wide-band nonreciprocity of surface acoustic waves induced by magnetoelastic coupling with a synthetic antiferromagnet,* Phys. Rev. Applied **12**, 054061 (2019).

[27] I. A. Viktorov, *Rayleigh and Lamb Waves: Physical Theory and Applications* (Springer, 1967).

[28] L. D. Landau, L. P. Pitaevskii, A. M. Kosevich, and E. M. Lifshitz, *Theory of Elasticity* (Butterworth-Heinemann, 1986).

[29] L. D. Landau and E. M. Lifshitz, *Electrodynamics of Continuous Media* (Butterworth-Heinemann, 1984).

[30] R. Manenti, A. F. Kockum, A. Patterson, T. Behrle, J. Rahamim, G. Tancredi, F. Nori, and P. J. Leek, *Circuit quantum acoustodynamics with surface acoustic waves,* Nature Communications **8**, 975 (2017).

[31] M. J. A. Schuetz, E. M. Kessler, G. Giedke, L. M. K. Vandersypen, M. D. Lukin, and J. I. Cirac, *Universal quantum transducers based on surface acoustic waves,* Phys. Rev. X **5**, 031031 (2015).

[32] L. R. Walker, *Magnetostatic modes in ferromagnetic resonance,* Phys. Rev. **105**, 390 (1957).

[33] C. W. Gardiner and M. J. Collett, *Input and output in damped quantum systems: Quantum stochastic differential equations and the master equation,* Phys. Rev. A **31**, 3761 (1985).

[34] A. A. Clerk, M. H. Devoret, S. M. Girvin, F. Marquardt, and R. J. Schoelkopf, *Introduction to quantum noise, measurement, and amplification,* Rev. Mod. Phys. **82**, 1155 (2010).

[35] S. Streib, N. Vidal-Silva, K. Shen, and G. E. W. Bauer, *Magnon-phonon interactions in magnetic insulators,* Phys. Rev. B **99**, 184442 (2019).

[36] Y. Long, J. Ren, and H. Chen, *Intrinsic spin of elastic waves,* Proceedings of the National Academy of Sciences **115**, 9951 (2018).

[37] M. Schreier, A. Kamra, M. Weiler, J. Xiao, G. E. W. Bauer, R. Gross, and S. T. B. Goennenwein, *Magnon, phonon, and electron temperature profiles and the spin seebeck effect in magnetic insulator/normal metal hybrid structures,* Phys. Rev. B **88**, 094410 (2013).

[38] A. A. Serga, A. V. Chumak, and B. Hillebrands, *YIG magnonics,* Journal of Physics D: Applied Physics **43**, 264002 (2010).

3

Magnetism on the thermal dynamics of 2D antiferromagnetic membranes

In the end, it's not the years in your life that count. It's the life in your years.

Abraham Lincoln

We developed a theoretical scheme of incorporating the magnetoelastic contribution into the thermal elastic dynamics for the thin membranes of 2D antiferromagnetic material with restricted geometry. We extended the elastic Grüneisen relation into an effective version which includes the magnetic counterpart to the volume change of internal energy. Based on the specific heat and thermal conductivity from the elastic and magnetic origins we predicted the dependency of observables, such as effective Grüneisen parameter, thermal expansion coefficient, and the damping factor, with respect to a wide range of temperature across the phase transition. Our model of analysis as been validated by applying to the case of $FePS_3$ flake resonator and the theoretical predictions fits well with the reported experiment data.

3.1. Introduction

In recent decades the 2D magnetic (van der Waals) layered materials have consistently attained the focus of research from both theoretical and experimental aspects [1, 2]. Compared to the three-dimensional counterpart, the 2D magnetic membranes constitute ideal platform to explore fundamental physics of magnetism and also its coupling to other degrees of freedom in the low dimensional regime [3]. The heterostructures build upon the 2D magnetism show susceptibility with respect to external stimuli leading to the emergent interfacial phenomena and novel spintronic devices [1, 4]. Within these materials, the FePS$_3$ compound is of particular interest because it is measured to be a 2D Ising model with zigzag antiferromagnetic (AFM) order in which the magnetic Fe atom constitute honeycomb lattice [5, 6]. Although the magnetic and electronic structure of this material has been studied intensively, there is limited understanding of its thermal properties and especially the magnetic contribution to the specific heat and thermal flux in the restricted geometry such as the thin membranes of several nanometers in thickness and micrometers in the planar dimension [5, 7, 8]. The knowledge of its thermal properties is important for further application in spin-caloritronics [4] and also stands for another tool of investigating the magnetic phase transition apart from the Raman spectroscopy [5, 9].

In this Chapter, we extend the analysis of magnetoelastic coupling into a wide range of temperature beyond the phase transition, aiming at providing a theoretical explanation for the observed anomaly [9] in thermal transport of FePS$_3$ flake resonator. Showing in the Fig. 3.1, the membranes suspended over a cavity undergo a drum-like vibration whose eigenfrequency is related to the planar strain which can be tuned by the gate voltage and also by the environment temperature due to the thermal expansion. At a fixed gate voltage the membrane is pushed down, and the increase of temperature leads to the drop of strain that at around the Neel temperature ($T_N \approx 114$ K) the breaking of magnetic stiffness would soften this material and a sudden drop of resonance frequency has been observed [9]. Moreover, the vanishing of magnons as additional thermal carrier after $T > T_N$ would lead to a drop of the overall thermal conductivity which has been measured through the damping factor Q^{-1} as function of temperature.
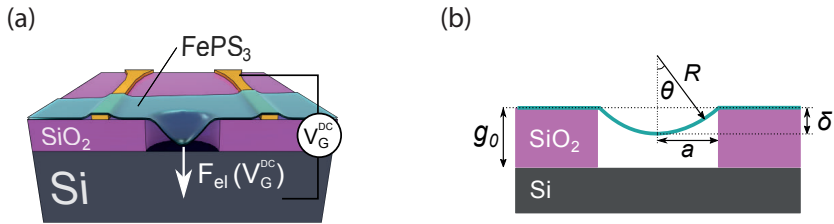
Figure 3.1: (a) Schematic figure for the FePS$_3$ resonator setup. The device is settled in nearly vacuum environment so that the thermal transfer through air damping can be ignored. Thermal expansion coefficient of the SiO$_2$ substrate is tiny and the silicon base is also small compared to the FePS$_3$. The flake thickness is $h = 45$ nm and diameter $d = 10\,\mu$m. (b) Fixed gate voltage pushes down the membranes and as temperature increases the flake expands leading to a decrease of planar tension. Figure quoted from publication [9].

In order to quantitatively explain experimental findings for thermal phenomena of the hybrid system, we develop a scheme of merging the magnetic contribution into the

thermoelastic dynamics and predict the temperature dependence for observables including heat capacity, linear expansion coefficient, and damping factor for the clamped FePS$_3$ membranes. Starting from the non-magnetic thermoelastic free energy we firstly derive the expression for the damping factor Q^{-1} of thin membrane/plate which turns out to be a function of the overall thermal expansion coefficient, the specific heat, and the thermal conductivity (See section 3.2). Then we derive the total specific heat C_V which has origins including the phonon and magnon excitations and also the part of energy required to break the Ising coherence around phase transition. We calculate the thermal conductivity κ as a sum of the phonon and magnon both as heat carriers and showed its magnitude are much smaller than the bulk compound because the limited particle lifetime due to the restricted geometry. Most importantly, by including the magnetoelastic Hamiltonian into the thermoelastic free energy we prove the total thermal expansion coefficient $\tilde{\alpha}$ retains the usual formalism of Grüneisen relation but with the incorporated effective Grüneisen parameter $\tilde{\gamma}$. It essentially describes the variation of internal energy including all the components ascribed to the volume change (See section 3.3). Using real material parameters we fitted experimental measurements with our model of analysis. Good agreement with recent experiment data [9, 10] supports the validity of our results (See section 3.4). The strong magnetic *weight* as part of the internal energy for this geometry restricted membranes making it an ideal platform to study the optomechanics integrated with the magnetism tuning. It is also expected that the model developed in this work can be useful for further analysis in the 2D spin-caloritronic devices.

3.2.   Bending of thin plate and the temperature gradient

In order to calculate the damping coefficient Q^{-1}, we firstly have to solve the coupled dynamics including the degree of freedom from elasticity, magnetism, and temperature field. In the following section 3.3.3, one shall see that the contribution of magnetoelastic coupling can be incorporated into the effective thermoelastic coupling and the governing equations of motion can be narrowed to including only the dynamics of elastic vibration and temperature gradient. In this section, we deal with the round plate with its undeformed surface lying on the $X-Y$ plane and study its out-of-plane ($\hat{z}$) vibration. We use the cylinder coordinate (r, φ, z) and assume its thickness h is much smaller than the plate diameter d, i.e. $h \ll d$. The displacement u_z and deformation ϵ_{ij} for plate are also considered to be small such that $u_i \ll h$ and $\epsilon_{ij} \ll h$.

The displacement fields along $(\hat{r}, \hat{\varphi})$ direction are respectively represented by u_r meaning the radial extension and u_φ meaning the circumferential distortion. One should note that u_φ represents the displaced distance along the $\hat{\varphi}$ direction not the φ itself, $u_\varphi = r d\varphi$. The strain tensor in cylinder coordinate is expressed in the form [11]

$$\epsilon_{rr} = \frac{\partial u_r}{\partial r}, \; \epsilon_{\varphi\varphi} = \frac{1}{r}\frac{\partial u_\varphi}{\partial \varphi} + \frac{u_r}{r}, \; \epsilon_{zz} = \frac{\partial u_z}{\partial z},$$

$$\epsilon_{\varphi z} = \frac{1}{2}\left(\frac{1}{r}\frac{\partial u_z}{\partial \varphi} + \frac{\partial u_\varphi}{\partial z}\right), \; \epsilon_{rz} = \frac{1}{2}\left(\frac{\partial u_r}{\partial z} + \frac{\partial u_z}{\partial r}\right), \tag{3.1}$$

$$\epsilon_{r\varphi} = \frac{1}{2}\left(\frac{\partial u_\varphi}{\partial r} - \frac{u_\varphi}{r} + \frac{1}{r}\frac{\partial u_r}{\partial \varphi}\right).$$

It is easy to show that according to the coordinate transformation, the relation $\epsilon_{rr} + \epsilon_{\varphi\varphi} + \epsilon_{zz} = \epsilon_{xx} + \epsilon_{yy} + \epsilon_{zz}$ holds, meaning the volume change, as it should, does not depends on the choice of coordination. Beyond this, the thermoelastic free energy (Eq. 1.43) and elastic tensor relation for isotropic material

$$\sigma_{ij} = K_T \epsilon_i^i \delta_{ij} + 2\mu(\epsilon_{ij} - \frac{1}{3}\epsilon_i^i \delta_{ij}), \quad \epsilon_i^i = \sum_i \epsilon_{ii}, \tag{3.2}$$

also hold true in formalism for any orthogonal coordinates [11].

In order to effective describe the characteristic deformation of the 3D elastic body we establish a concept of neutral surface. Regarding to the bending of thin plate, one side is compressed (the concave side) while the opposite is extended (convex side). Between these two sides, there is a surface which has neither extension nor compression, i.e. $\epsilon_i^i = 0$, and is referred as the *neutral surface*. Mount the undeformed neutral surface onto the $z = 0$ plane and based on the small deformation assumption, the displacement on the neutral surface is $u_r^0 = 0$, $u_\varphi^0 = 0$, $u_z^0 = \zeta(r, \varphi, t)$ with $\zeta \ll h$. Due to the small deformation, the internal stress on z-th surface should be much smaller than the stress along the longitudinal direction, $\sigma_{iz} = 0$, which leads to the hypotheses inside the bulk volume [12, 13]

$$\epsilon_{rz} = 0, \quad \epsilon_{\varphi z} = 0, \quad \sigma_{zz} = 0. \tag{3.3}$$

With the assumed neutral surface hypotheses, the displacement inside the plate can be expressed by the function of ζ that

$$u_r = -z\frac{\partial \zeta}{\partial r}, \quad u_\varphi = -\frac{z}{r}\frac{\partial \zeta}{\partial \varphi}, \quad u_z = \zeta. \tag{3.4}$$

and the remaining strain components are given by

$$\begin{aligned}
\epsilon_{rr} &= -z\frac{\partial^2 \zeta}{\partial r^2}, & \epsilon_{\varphi\varphi} &= -z\left(\frac{1}{r}\frac{\partial \zeta}{\partial r} + \frac{1}{r^2}\frac{\partial^2 \zeta}{\partial \varphi^2}\right), \\
\epsilon_{r\varphi} &= -z\frac{\partial}{\partial r}\left(\frac{1}{r}\frac{\partial \zeta}{\partial \varphi}\right), & \epsilon_{zz} &= \frac{z\sigma}{1-\sigma}\left(\frac{\partial^2 \zeta}{\partial r^2} + \frac{1}{r}\frac{\partial \zeta}{\partial r} + \frac{1}{r^2}\frac{\partial^2 \zeta}{\partial \varphi^2}\right).
\end{aligned} \tag{3.5}$$

Define the Laplace operator on the plane

$$\Delta = \frac{\partial^2}{\partial r^2} + \frac{1}{r}\frac{\partial}{\partial r} + \frac{1}{r^2}\frac{\partial^2}{\partial \varphi^2}, \tag{3.6}$$

then $\epsilon_{rr} + \epsilon_{\varphi\varphi} = -z\Delta\zeta$ and $\epsilon_{zz} = \frac{z\sigma}{1-\sigma}\Delta\zeta$. For the case of axial symmetric plate it is reasonable to assume $\zeta = \zeta(r, t)$ which does not depends on the polar angle φ, then the strain can be even simplified into

$$\epsilon_{rr} = -z\frac{\partial^2 \zeta}{\partial r^2}, \quad \epsilon_{\varphi\varphi} = -\frac{z}{r}\frac{\partial \zeta}{\partial r}, \quad \epsilon_{zz} = \frac{z\sigma}{1-\sigma}\Delta\zeta, \quad \Delta = \frac{\partial^2}{\partial r^2} + \frac{1}{r}\frac{\partial}{\partial r}, \tag{3.7}$$

and other components equals to zero. Substituting the strain tensor into the thermoelastic free energy (Eq. 1.43) one can derive its expression as the function of ζ

$$F_{\text{el}} = \int_0^{2\pi} d\varphi \int_0^R r\,dr \frac{Y h^3}{12(1-\sigma^2)}\left[(1+\sigma)\frac{\alpha}{3}I_T\Delta\zeta + \frac{1}{2}\left(\zeta''^2 + \frac{1}{r^2}\zeta'^2 + \frac{2\sigma}{r}\zeta'\zeta''\right)\right], \tag{3.8}$$

where the thermal inertia

$$I_T(r) = \frac{12}{h^3} \int_{-h/2}^{h/2} z\theta(r,z)\,dz, \qquad (3.9)$$

in which $\theta = T - T_0$ is small differences between the temperature within the plate T and the environment temperature T_0. The internal force exerted on to the volume element of unit surface is $f_\zeta = -\delta F_{\text{el}}/\delta\zeta$ and the equation of motion for the vibration of the circular plate is

$$\rho h \frac{\partial^2 \zeta}{\partial t^2} + \frac{\partial F_{\text{el}}}{\partial \zeta} = 0 \quad \rightarrow \quad \rho h \frac{\partial^2 \zeta}{\partial t^2} + \frac{Yh^3}{12(1-\sigma^2)} [\Delta\Delta\zeta + (1+\sigma)\alpha/3\,\Delta I_T] = 0. \qquad (3.10)$$

As for the dynamics of temperature field the heat diffusion equation is a rephrase of energy conservation, that is the heat absorption equals to the energy flows $T\frac{\partial S}{\partial t} = -\nabla \cdot \mathbf{q} = \kappa\Delta T$ with $\mathbf{q} = -\kappa\nabla T$ is the thermal flux and κ is the heat conduction coefficient [14]. From the thermoelastic coupling we understand that the heat absorption leads to not only increase of particle motion but also the volume expansion, $dS = dS_0(T) + K_T\alpha\epsilon_i^i$. Applying the relation $\partial S_0/\partial T = \rho C_V/T$, we have $\rho C_V \partial T/\partial t = \kappa\Delta T - K_T\alpha T_0\partial\epsilon_i^i/\partial t$. The equation of motion for describing the dynamics of small temperature differences within the plate has the general form

$$\kappa\Delta\theta + \kappa\frac{\partial^2\theta}{\partial z^2} = \rho C_V \frac{\partial\theta}{\partial t} + K\alpha T_0 \frac{\partial\epsilon_i^i}{\partial t}. \qquad (3.11)$$

As from Ref. [15] we make an approximation that the temperature gradient is small in the longitudinal direction compared to the vertical direction, $\Delta\theta \ll \partial^2\theta/\partial z^2$. Combing the strain components from Eq. 3.7 the governing equation for the dynamics of temperature field in thin plate then becomes

$$\kappa\frac{\partial^2\theta}{\partial z^2} = \rho C_V \frac{\partial\theta}{\partial t} - zK_T\alpha T_0 \frac{1-2\sigma}{1-\sigma}\frac{\partial\Delta\zeta}{\partial t}. \qquad (3.12)$$

Inserting the ansatz solution $\zeta = \zeta_0 e^{i\omega t}$ and $\theta = \theta_0 e^{i\omega t}$ into the Eq. 3.12 we have the equation for temperature field which can be solved by the boundary condition that there is no thermal conduction on the top and bottom surface,

$$\frac{\partial\theta_0}{\partial z} = 0 \quad \text{at } z = \pm\frac{h}{2}. \qquad (3.13)$$

The solved temperature profile across the plate is given by

$$\theta_0(r,z) = \frac{K_T\alpha T_0}{\rho C_V}\frac{1-2\sigma}{1-\sigma}\left[z - \frac{\sin(mz)}{m\cos(mh/2)}\right]\Delta\zeta_0, \qquad (3.14)$$

with the wave vector

$$m = \sqrt{-\frac{i\omega\rho C_V}{\kappa}} = (1-i)\sqrt{\frac{\omega\rho C_V}{2\kappa}}. \qquad (3.15)$$

Applying this temperature profile into the moment of inertia (Eq. 3.9) and the elastic equation of motion (Eq. 3.10) becomes an eigen-equation

$$\rho h\omega^2\zeta_0 = \frac{Yh^3}{12(1-\sigma^2)}[1 + \Delta_Y(1 + f(\omega))]\Delta\Delta\zeta_0 \quad \rightarrow \quad \frac{Y_\omega h^3}{12(1-\sigma^2)}\Delta\Delta\zeta_0 = \rho h\omega^2\zeta_0, \quad (3.16)$$

with the modified Young's modulus $Y_\omega = [1 + \Delta_Y(1 + f(\omega))]$ is frequency-dependent and the adiabatic degree $f(\omega)$ ranges from -1 to 0 for low and high vibrating frequency identifying the isothermal and adiabatic extremes,

$$f(\omega) = \frac{24}{m^3 h^3}\left[\frac{mh}{2} - \tan\left(\frac{mh}{2}\right)\right]. \tag{3.17}$$

The quantity Δ_Y which is a measure of *thermal relaxation strength* acquires the from

$$\Delta_Y = \frac{1+\sigma}{1-\sigma}\frac{Y\alpha^2 T_0}{\rho C_V}. \tag{3.18}$$

Letting $12(1-\sigma^2)\rho\omega^2/Y_\omega h^2 = q^4$, then the Eq. 3.16 becomes $\Delta\Delta\zeta_0 = q^4\zeta_0$ and can be solved by $\Delta\zeta_0 = q^2\zeta_0$ with $\zeta_0 = AJ_0(qr) + BY_0(qr) + CI_0(qr) + DK_0(qr)$. Here (J_0, Y_0, I_0, K_0) are the first and second Bessel functions of the zero-th order respectively. Due to the finite value of ζ_0 at $r = 0$, the $B = D = 0$ and $\zeta_0 = AJ_0(qr) + CI_0(qr)$ with the coefficient (A, C) to be defined by the boundary condition. For the case of clamped plate, the boundary condition (a is plate radius) has the form $\zeta_0|_{r=a} = 0$, $\partial\zeta_0/\partial r|_{r=a} = 0$, which can be satisfied by $(q_n a)^2 \equiv \mathscr{C}_n = \{10.21, 39.38, 89.10, \cdots\}$. The complex eigenfrequency then reads

$$\omega = \omega_0\sqrt{1 + \Delta_Y(1 + f(\omega_0))}, \tag{3.19}$$

with the unperturbed eigenfrequency for the n-th vibration mode is

$$\omega_0 = q_n^2 h\sqrt{\frac{Y}{12\rho(1-\sigma^2)}} = \mathscr{C}_n\frac{h}{a^2}\sqrt{\frac{Y}{12\rho(1-\sigma^2)}}. \tag{3.20}$$

Due to the complex value of frequency ω, the time dependency $e^{i\omega t}$ of physical quantity decays along with the oscillation. Assuming $\omega = \omega_0(1 + i\eta)$ then the displacement decays as $\zeta(t) \sim e^{i\omega_0 t}e^{-\eta\omega_0 t}$. The damping for this oscillating system is captured by the damping factor Q^{-1} which is defined to be the ratio of energy loss per radian to the energy stored in the oscillator. Because the oscillating energy is quadratic to the displacement field so we have $E(t) \sim e^{-2\eta\omega_0 t}$ leading to the fractional energy loss per radian is $1 - e^{-2\eta} \approx 2\eta$. Thus the system damping for elastic oscillator is qualified by the $Q^{-1} = 2|\text{Im}(\omega)/\text{Re}(\omega)|$. Shortening the parameter mh within the function $f(\omega)$ into a single variable ξ [15]

$$\xi = h\sqrt{\frac{\omega_0\rho C_V}{2\kappa}}, \tag{3.21}$$

the thermoelastic damping Q^{-1} can be derived as

$$Q^{-1} = \Delta_Y\left(\frac{6}{\xi^2} - \frac{6}{\xi^3}\frac{\sinh\xi + \sin\xi}{\cosh\xi + \cos\xi}\right) = \frac{1+\sigma}{1-\sigma}\frac{Y\alpha^2 T_0}{\rho C_V}\left(\frac{6}{\xi^2} - \frac{6}{\xi^3}\frac{\sinh\xi + \sin\xi}{\cosh\xi + \cos\xi}\right). \tag{3.22}$$

Since the thermoelastic variables such as α, κ and C_V are temperature dependent, it is easy to understand the damping factor Q^{-1} also changes with T_0 and it will show anomaly in the present of second order phase transition with which the specific heat C_V has observed discontinuity. For convenience, in the following we will replace the environment temperature T_0 by the symbol T with consensus.

3.3. Thermal observables for elastic plate hybrid with magnetic phase transition

In this section we study the thermal observables for the elastic plate hybrid with magnetism for a wild range of temperature across the phase transition. To this aim we start with deriving the heat capacity and thermal conductivity due to the bosons. Then we shows the incorporation of magnetoelastic coupling into the effective thermoelastic free energy and derive the effective expansion coefficient $\tilde{\alpha}$ and damping factor Q^{-1} for the thermal-magnetic-elastic vibrating system.

In general, below the phase transition the material's heat capacity $C = dQ/dT$ comes from the thermal excitation of the bosons, which are quasi-particles mainly the phonons for ordinary insulators and also include magnons for FM and AFM materials. If the temperature is homogeneous then the Bose-Einstein density of excited bosons is uniformly distributed across the material. However, the existence of temperature field leads to the excess number of quasi-particles staying out of equilibrium and then transport according to the temperature gradient. If the environment temperature is close to the range of magnetic phase transition, the coherence of precession between the neighbouring spins breaks down and an additional contribution to the specific heat should be taken into account. The decaying of magnetization $\boldsymbol{M}$ as the heating procedure leads to an accompanying decrease of the effective exchange field H_E and anisotropy field H_A in magnon's dispersion equation 1.26. This energy renormalization [16, 17] should also be incorporated into the calculation of magnon's specific heat and thermal conductivity.

Mathematically the heat capacity due to the bosons is

$$C_V = \frac{1}{V} \frac{\partial}{\partial T} \sum_{\boldsymbol{k}} \hbar \omega_{\boldsymbol{k}} \bar{n}_{\boldsymbol{k}}, \quad \bar{n}_{\boldsymbol{k}} = \frac{1}{e^{\beta \hbar \omega_{\boldsymbol{k}}} - 1}, \tag{3.23}$$

where $\bar{n}_{\boldsymbol{k}}$ is the Bose-Einstein's equilibrium amount of bosons of energy $\hbar \omega_{\boldsymbol{k}}$. The thermal conductivity is defined as the coefficient for heat flux due to the temperature gradient, $\boldsymbol{q} = -\kappa \nabla T$. From kinetic transfer theory this thermal flux can be calculated by

$$\boldsymbol{q} = -\frac{1}{V} \sum_{\boldsymbol{k}} \hbar \omega_{\boldsymbol{k}} \boldsymbol{v}_{\boldsymbol{k}} (\tau_{\boldsymbol{k}} \boldsymbol{v}_{\boldsymbol{k}} \cdot \nabla \bar{n}_{\boldsymbol{k}}) = -\frac{1}{V} \frac{\partial}{\partial T} \sum_{\boldsymbol{k}} \hbar \omega_{\boldsymbol{k}} \bar{n}_{\boldsymbol{k}} \tau_{\boldsymbol{k}} (\nabla T \cdot \boldsymbol{v}_{\boldsymbol{k}}) \boldsymbol{v}_{\boldsymbol{k}}, \tag{3.24}$$

in which an isotropic κ can be extracted if the particle velocity $\boldsymbol{v}_{\boldsymbol{k}}$ is homogeneous to each direction. However, if the particle velocity has directional bias then κ depends on the orientation and thermal transfer shows anisotropy. In the simplest case, if the particle's lifetime $\tau_{\boldsymbol{k}} = \tau_0$ and velocity $\boldsymbol{v}_{\boldsymbol{k}} = \bar{v}$ does not depends on wavevector $\boldsymbol{k}$ we see that the thermal flux can be simplified as $\boldsymbol{q} = -\frac{\bar{v}^2 \tau_0}{V} \frac{\partial}{\partial T} \sum_{\boldsymbol{k}} \hbar \omega_{\boldsymbol{k}} \bar{n}_{\boldsymbol{k}} \nabla T \equiv -C \bar{v}^2 \tau_0 \cdot \nabla T$ leading to the simple form $\kappa = C \bar{v}^2 \tau_0$. Once we know the dispersion relation $\omega_{\boldsymbol{k}}$ and the lifetime $\tau_{\boldsymbol{k}}$ for the mobile quasi-particles we can determine specific heat C_V and thermal conductivity κ at least in a numerical way.

The elastic specific heat and thermal conductivity can be derived from the statistics of low lying phonon modes (acoustic modes) based on the general equations of 3.23 and 3.24 with the sound wave dispersion relation $\omega_{\boldsymbol{k}} = \bar{v} \boldsymbol{k}$, and $\bar{v}$ is the Debye averaged

acoustic velocity defined in Eq. 1.42,

$$
\begin{aligned}
C_{\mathrm{db}}(T) &= \frac{\hbar^2}{2\pi} \frac{3}{k_B T^2} \int_0^{k_{\mathrm{db}}} dk \frac{k\omega_k^2 e^{\beta\hbar\omega_k}}{(e^{\beta\hbar\omega_k}-1)^2}, \\
\kappa_{\mathrm{db}}(T) &= \frac{\hbar^2}{4\pi} \frac{3\bar{v}^2}{k_B T^2} \int_0^{k_{\mathrm{db}}} dk \frac{\tau_k k\omega_k^2 e^{\beta\hbar\omega_k}}{(e^{\beta\hbar\omega_k}-1)^2}.
\end{aligned}
\tag{3.25}
$$

The elastic zone boundary can be defined by the Debye temperature as $k_{\mathrm{db}} = k_B T_{\mathrm{db}}/\hbar\bar{v}$. Note that here we have assumed the elastic lattice is of 2D while the vibration is still 3 dimensional. It can be adjusted easily to the longitudinal or shear polarization only by replacing the factor 3 into 1 or 2 respectively.

3.3.1. Specific heat and thermal conduction due to the magnon excitations

Specific to the 2D AFM material, we set the external field $H_0 = 0$ and according to Eq. 1.26 the dispersion relation depends on the direction of wave vector $\boldsymbol{k}$. Contrary to detailed treatment as in the Refs. [7], in this work we simplify the detailed 2D lattice structure and make the homogeneous assumption ($a = b$) such that we rephrase the $\psi_{\boldsymbol{k}}$ of Eq. 1.27 into $\psi_k = \cos(\pi k/2k_m)$ being isotropic with $k \in [0, k_m]$ is limited to the first Brillouin zone and k_m is defined from the spherical energy boundary assumption [16, 18],

$$
\sum_{\boldsymbol{k}} = \frac{V}{(2\pi)^2} \int d\boldsymbol{k} = \frac{Na^2}{(2\pi)^2} \int_0^{k_m} 2\pi k dk = N \quad \rightarrow \quad \frac{k_m a}{2} = \sqrt{\pi}.
\tag{3.26}
$$

Thus, the dispersion relation for AFM magnon becomes

$$
\hbar\omega_k = \gamma\mu_0 H_E \sqrt{\sin^2(\pi k/2k_m) + \eta^2 + 2\eta},
\tag{3.27}
$$

with $\eta = H_A/H_E$ is the ratio of anisotropy field to the exchange field. For some AFM material such as the RbMnF$_3$ which has very small anisotropy $H_A = 4.5$ Oe, the exchange field is as large as $H_E = 830$ kOe leading to $\eta \approx 0$ and it is considered as a typical 3D Heisenberg antiferromagnet [19, 20]. For other materials such as the FeF and the FePS$_3$ used in our experiment the magnetic anisotropy is strong and comparable to the exchange field, resulting in $\eta \gtrless 1$ which makes them a quasi Ising system [19, 21].

As environment temperature goes up, the spontaneous magnetization $M(T)$ decays because the thermal magnon excitation [16, 22] and also the decoherence between neighbouring spins for the $T \lesssim T_N$. Since $M = -g\mu_B NS$, the effective spin magnitude $S(T)$ decays which results in the decreasing of $H_E = 2Sz|J|/\mu_0\gamma$ and $H_A = 2SA/\mu_0\gamma$ in the dispersion relation. As a consequence, the temperature dependence for the $\omega(T)$ should be taken into account in deriving the magnon specific heat and thermal conductivity. For simple treatment one can apply the molecular field approximation (mean field theory) in which the magnetization $M(T) = M_0 B(x)$ with $B(x)$ is the Brillouin function and $x = \mu_0 n_w M(T) g\mu_B S_0/k_B T$ is the normalized energy [23]. Although this mean field approach does not provide the correct magnetization around phase transition, it leads to good results of magnon spectra at temperatures $T < 0.8 T_N$ [16, 17].
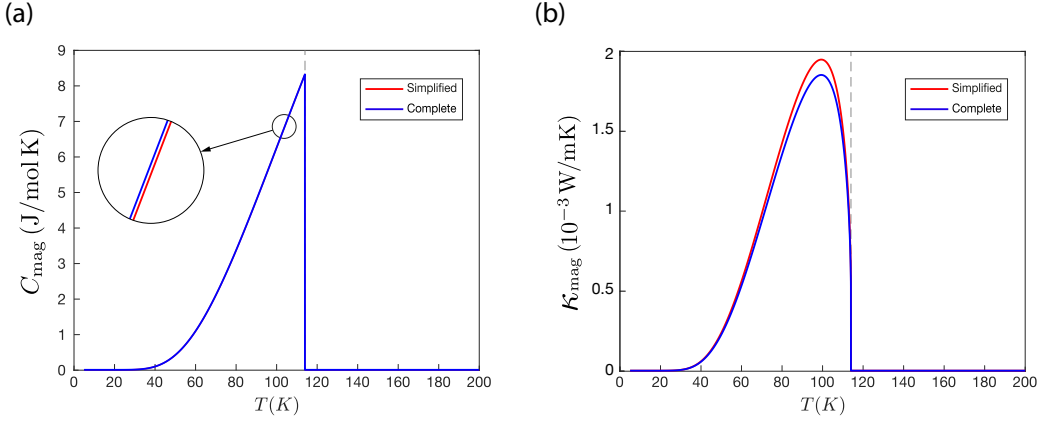
(a) (b)

Figure 3.2: (a) The magnon's specific heat and (b) thermal conductivity derived from the complete 2-D integral and the simplified 1-D integral respectively. Here we assumed the lifetime for magnon is approximately 1.8 ps and does not depends on the modes for simplicity. The results indicate the difference between these two integral strategy is small and we can use the simplified version for further calculations.

With the derived dispersion relation, the heat capacity due to thermal magnons excitation in the 2D AFM model is

$$
\begin{aligned}
C_{\mathrm{mag}}(T) &= \frac{\hbar^2}{2\pi} \frac{1}{k_B T^2} \int_0^{k_m} dk \frac{k\omega_k^2 \cdot e^{\beta\hbar\omega_k}}{(e^{\beta\hbar\omega_k}-1)^2} \\
&= \frac{\hbar^2 k_m^2}{2\pi k_B} \frac{1}{T^2} \int_0^1 dq \frac{q\omega_q^2 \cdot e^{\beta\hbar\omega_q}}{(e^{\beta\hbar\omega_q}-1)^2},
\end{aligned}
\tag{3.28}
$$

where the explicit temperature dependence on $\omega_k(T)$ has been suppressed and we replace k with the normalized wave vector $q = k/k_m$ ranging from 0 to 1. As a comparison, we plot the $C_{\mathrm{mag}}(T)$ derived from the 2-D integral of (q_x, q_y) of the dispersion relation $\hbar\omega_{\boldsymbol{q}} = \gamma\mu_0 H_E \sqrt{(1-\psi_{\boldsymbol{q}}^2)+\eta^2+2\eta}$ with $\psi_{\boldsymbol{q}} = \cos(q_x\pi/2)\cos(q_y\pi/2)$. Showing in Fig. 3.2(a) we see the complete 2-D integral and the simplified one result in almost exactly the same curve which validates that we can indeed ignore the direction of (q_x, q_y) and shorten the $\psi_{\boldsymbol{q}}$ into 1-D integral on q with the $\psi_q = \cos(q\pi/2)$.

For the magnon's thermal conductivity, it is defined from the heat flux (Eq. 3.24) that

$$
\boldsymbol{q} = -\frac{1}{(2\pi)^2} \int d\boldsymbol{k} \frac{1}{k_B T^2} \frac{\tau_k (\hbar\omega_k)^2 e^{\beta\hbar\omega_k}}{(e^{\beta\hbar\omega_k}-1)^2} (\nabla T \cdot \boldsymbol{v}_k)\boldsymbol{v}_k.
\tag{3.29}
$$

Using the 2-D dispersion relation we derive the velocity of magnons to be

$$
(v_x, v_y) = \frac{\gamma\mu_0 H_E}{2\hbar k_m} \frac{\pi\psi_k}{\sqrt{(1-\psi_k^2)+\eta^2+2\eta}} \cdot \left(\sin\frac{k_x\pi}{2k_m}\cos\frac{k_y\pi}{2k_m}, \cos\frac{k_x\pi}{2k_m}\sin\frac{k_y\pi}{2k_m} \right),
\tag{3.30}
$$

with which the integral can be performed as

$$
\int (\nabla\boldsymbol{T}\cdot\boldsymbol{v}_k)\boldsymbol{v}_k \, d\boldsymbol{k} = \nabla\boldsymbol{T} \frac{1}{2} \int (v_x^2 + v_y^2) \, d\boldsymbol{k},
\tag{3.31}
$$

where we have used the fact that $\int v_x^2 d\mathbf{k} = \int v_y^2 \mathbf{k}$ due to the symmetry consideration. From the heat flux expression we extract the thermal conductivity and written into the form of 2-D integral,

$$\kappa_{\mathrm{mag}} = \left(\frac{\gamma\mu_0 H_E}{8}\right)^2 \frac{1}{k_B T^2} \int \frac{\tau_k e^{\beta\hbar\omega_q}}{(e^{\beta\hbar\omega_q}-1)^2} \left[\left(\frac{\gamma\mu_0 H_E}{\hbar}\right)^2 - \left(\omega_q^2 - \omega_0^2\right)\right] (1 - \cos q_x \pi \cdot \cos q_y \pi) d\mathbf{q}, \tag{3.32}$$

Based on the homogeneous lattice assumption, it can be further simplified into the 1-D integral of q such that

$$\kappa_{\mathrm{mag}} = \left(\frac{\gamma\mu_0 H_E}{8}\right)^2 \frac{\pi}{k_B T^2} \int_0^1 \frac{\tau_k \omega_q^2 e^{\beta\hbar\omega_q}}{(e^{\beta\hbar\omega_q}-1)^2} \frac{q \sin^2 q\pi}{\sin^2 q\pi/2 + \eta^2 + 2\eta} dq, \tag{3.33}$$

where $\hbar\omega_q = \gamma\mu_0 H_E \sqrt{\sin^2 q\pi/2 + \eta^2 + 2\eta}$. Showing in Fig. 3.2(b) we notice again the difference between complete 2-D integral and the simplified one is small enough for the case of κ_{mag}, and in the following we shall use the 1-D integral of q for the thermal observables. At low temperatures the heat capacity and thermal conductivity share the same growing curve due to the fact that $\kappa \approx Cvl = Cv^2\tau$ and v, τ are almost constant for small T. At large enough temperatures the exchange fields $H_E(T)$ decays in step with the decreasing of $M(T)$ which leads to the softening of magnons and after phase transition there is no existence of magnons. Thus we see the drop of C_{mag} and κ_{mag} for $T > T_N$. Additionally the particle's lifetime (or its inverse $\tau^{-1} = \eta$ the relaxation rate) plays an important role in their transport properties. In general, the relaxation rate for various particles, either bosons or fermions, comes from several origins [24] that $\eta = \eta_{\mathrm{bd}} + \eta_{\mathrm{pt}} + \eta_{\mathrm{nlsc}}$, with η_{bd} is the boundary deflection by material edges, η_{pt} is the scattering with the point defects, and η_{nlsc} stands for the non-linear scattering among particles themselves. Usually $\eta_{\mathrm{bd}} + \eta_{\mathrm{pt}} = \eta_0 \equiv \tau_0^{-1}$ is a constant which does not depend on wavevector k and temperature T. The non-linear scattering has several origins for different particles but it is generally proportional to T for the 3-particle scattering and T^2 for the 4-particle scattering process [25, 26]. Therefore $\eta_k = \eta_0(1 + b_k T + c_k T^2)$ and the coefficients can be calculated by studying the detailed process. However, in this work of membranes setup both the phonon and magnon's lifetime are limited by the defect and boundary scattering [27]. Therefore we shall ignore the non-linear scattering between quasi-particles and claim the lifetime $\tau = \tau_0$ is a constant which does not depends on the wave vector nor the temperature.

3.3.2. Specific heat due to the break of spin coherence around phase transition

As the environment temperature close to the phase transition regime the magnetic specific heat is dominated by energy absorption for the breaking of spin coherence and due to the nature of second order phase transition the anomaly of C_M near T_N should be expected [23]. The derivation for anomaly of C_M depends on the detailed lattice structure. In this chapter we focus on the material FePS$_3$ which is an Ising-type 2D antiferromagnet of the honeycomb (hexagon) lattice [6–8, 28]. According to the references [29–31],
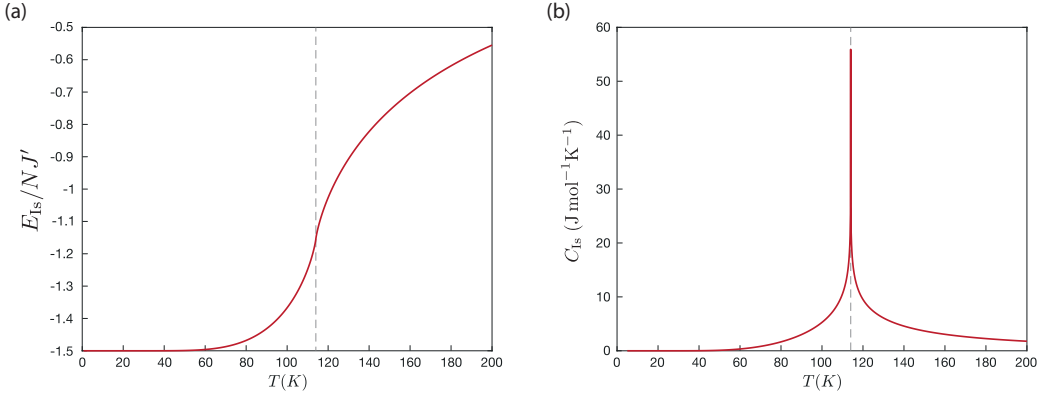
Figure 3.3: The temperature dependence of magnetic energy and specific for 2D Ising honeycomb lattice, numerically calculated according to the Eq. 3.36. One can check that at $T = 0$, $K \to \infty$ then $E_{Is}/NJ' \to -3/2$ as expected because the coordination number for honeycomb lattice is 3.

the partition function for honeycomb lattice reads

$$\frac{1}{N}\log Z(T) = \log 2 + \frac{1}{16\pi^2}\int_0^{2\pi}\int_0^{2\pi} d\theta_1 d\theta_2 \log\left[\cosh^3 2K + 1 - \sinh^2 2K \cdot P_{\boldsymbol{\theta}}\right], \quad (3.34)$$

where $K = J'/k_B T \equiv \beta J'$ is the normalized temperature in which J' is the effective coupling energy from the exchange Hamiltonian $H = -2J\sum \boldsymbol{S}_i \cdot \boldsymbol{S}_j \equiv -J'\sum \hat{\boldsymbol{S}}_i \cdot \hat{\boldsymbol{S}}_j$, thus $J' = 2JS^2$ [30]. The integrand parameter is $P_{\boldsymbol{\theta}} = \cos\theta_1 + \cos\theta_2 + \cos(\theta_1 + \theta_2)$ [31]. The critical point for honeycomb lattice is reached as $\sinh 2K_c = \sqrt{3}$ and the Neel temperature is

$$T_N = \frac{2J'}{k_B \log(2 + \sqrt{3})}. \quad (3.35)$$

Thus one can derive the effective coupling energy J' based on the measured Neel temperature. Following the procedures of differentiating $E_{Is} = -\frac{d\log Z}{d\beta}$ and $C_{Is} = \frac{dE_{Is}}{dT}$, we have the specific heat due to the breaking of spin coherence reads

$$\frac{1}{Nk_B}C_{Is}(T) = \frac{K^2}{16\pi^2}\int_0^{2\pi}\int_0^{2\pi} d\theta_1 d\theta_2 \left\{ \frac{6\sinh 4K \sinh 2K - 4\cosh 4K(2P_{\boldsymbol{\theta}} - 3\cosh 2K)}{\cosh^3 2K + 1 - \sinh^2 2K \cdot P_{\boldsymbol{\theta}}} \right.$$
$$\left. - \frac{\sinh^2 4K(2P_{\boldsymbol{\theta}} - 3\cosh 2K)^2}{\left[\cosh^3 2K + 1 - \sinh^2 2K \cdot P_{\boldsymbol{\theta}}\right]^2} \right\}.$$
$$(3.36)$$

The temperature dependence of the Ising type magnetic energy and specific heat is shown in Fig. 3.3 Although there is no macroscopic magnetization above T_N, the short range spin correlations still persist and shall finally vanish to zero for large enough temperature. The total magnetic specific heat for our material FePS$_3$ is then a sum of the Ising and magnon's contribution $C_M = C_{Is} + C_{mag}$.

3.3.3. Incorporating the magnetoelastic coupling into thermoelastic free energy

The previous analysis for the damping of thin plate in section 3.2 does not involve the magnetic effect on the heat transportation. In nature, the magnetoelastic coupling should be included into the total free energy and the analysis of the hybrid of magnetic, elastic, and thermal dynamics should be considered [32, 33]. According to Refs. [34, 35], the magnetoelastic coupling energy in general has the form

$$F_{\text{MEC}} = -Nz\frac{\partial J}{\partial V}\langle \boldsymbol{S}_i \cdot \boldsymbol{S}_j\rangle \epsilon_i^i, \tag{3.37}$$

in which N is the number of spins per unit volume, z is the coordination number, and ϵ_i^i is the fractional volume change. The two-spin correlation function $\langle \boldsymbol{S}_i \cdot \boldsymbol{S}_j\rangle$ indicates the average over space and time for any two nearest neighbouring spins. Incorporating this free energy into the thermal elastic one (Eq. 1.43) we write down the total free energy taking both the thermal and magnetic elastic coupling into consideration

$$F = F_0 - K_T\alpha_E\theta\epsilon_i^i + \frac{1}{2}K_T\left(\epsilon_i^i\right)^2 + \mu\sum_{ij}\left(\epsilon_{ij} - \frac{1}{3}\epsilon_i^i\delta_{ij}\right)^2 - Nz\frac{\partial J}{\partial V}\langle \boldsymbol{S}_i \cdot \boldsymbol{S}_j\rangle\epsilon_i^i. \tag{3.38}$$

Note that we have replaced α in Eq. 1.43 with the symbol α_E in order to highlight its elastic origin. The strain in equilibrium can be derived from $\partial F/\partial\epsilon_i^i = 0$, leading to the combined effect on volume changes due to both thermal expansion and magnetostriction

$$\epsilon_i^i = \alpha_E\theta - \beta_T Nz\frac{J}{V}\gamma_M\langle \boldsymbol{S}_i \cdot \boldsymbol{S}_j\rangle, \tag{3.39}$$

where the magnetic Grüneisen constant γ_M describing the volume dependence on the exchange coupling strength has the form [34, 36]

$$\gamma_M = -\frac{V}{J}\frac{\partial J}{\partial V}. \tag{3.40}$$

The part of volume changes due to the magnetostriction is proportional to the two-spin correlation function which can be changed by the variation of either temperature or external field. In this chapter we assume there is no external field applied onto the plate, then the temperature increase leads to the decaying of spin correlation and results in the magnetostriction expansion. Since the magnetic energy derived from the Heisenberg Hamiltonian $H = -2J\sum\boldsymbol{S}_i \cdot \boldsymbol{S}_j$ is that $E_M = -NzJ\langle \boldsymbol{S}_i \cdot \boldsymbol{S}_j\rangle$, it is reasonable to defines the magnetic specific heat as [33]

$$C_M = -NzJ\frac{\partial\langle \boldsymbol{S}_i \cdot \boldsymbol{S}_j\rangle}{\partial T}. \tag{3.41}$$

As a result the deviation of local spin coherence due to the small change of local temperature θ is $C_M\theta = -NzJ\langle \boldsymbol{S}_i \cdot \boldsymbol{S}_j\rangle$ and the total volume change can be succinctly expressed into the form

$$\epsilon_i^i = \alpha_E\theta + \beta_T\gamma_M\frac{C_M}{V}\theta = (\alpha_E + \alpha_M)\theta \equiv \tilde{\alpha}\theta. \tag{3.42}$$
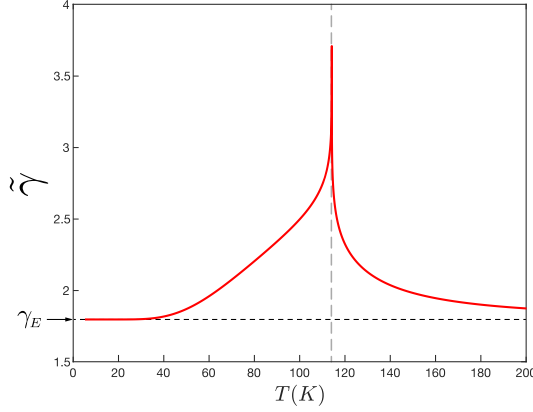
Figure 3.4: Temperature dependence for the effective Grüneisen parameter $\tilde{\gamma}$ derived from Eq. 3.44. The elastic parameter is calculated to be to be $\gamma_E = 1.798$ [9] and the ratio is chosen to be $\gamma_M/\gamma_E = \nu = 4$. The $\tilde{\gamma}$ start from γ_E because the $C_M \approx 0$ for small temperatures.

We see that by merging the magnetoelastic coupling into the free energy, the thermal expansion coefficient α_E should be extended to the one including the magnetic contribution $\tilde{\alpha} = \alpha_E + \alpha_M$.

The magnetic Grüneisen relation $\alpha_M = \beta_T \rho \gamma_M C_M$ is almost similar to the elastic counterpart (Eq. 1.49) meaning the thermal and magnetic properties both originate from the variation of spin coherence and it is the magnetic Grüneisen parameter makes them a connection. Therefore the overall thermal expansion coefficient for the hybrid system can be written into the form

$$\tilde{\alpha} = \beta_T \rho \gamma_E C_E + \beta_T \rho \gamma_M C_M = \beta_T \rho \left(\gamma_E C_E + \gamma_M C_M \right) = \beta_T \rho \tilde{\gamma} C_V, \qquad (3.43)$$

which maintains the Grüneisen relation formalism but with $C_V = C_E + C_M$ is the total specific heat combining the elastic and magnetic ones and with the effective Grüneisen parameter defined as

$$\tilde{\gamma} = \frac{\gamma_E C_E + \gamma_M C_M}{C_E + C_M}. \qquad (3.44)$$

Although the elastic and magnetic Grüneisen parameters are both almost independent of temperature [35, 37], the effective Grüneisen parameter usually presents a peak at phase transition T_N (as shown in Fig. 3.4). This phenomenon originates from the anomaly of magnetic specific heat near phase transition rendering the $\tilde{\gamma} \approx \gamma_E$ for T far away from T_N and $\tilde{\gamma} \approx \gamma_M$ for the T close to T_N. Usually the γ_M is several times larger than the elastic γ_E and it can be theoretically predicted based on detailed study of magnetic structure [36]. In this work, however, we shall simplify the analysis by assuming a phenomenological factor $\nu = \gamma_M/\gamma_E$ which can be further determined by fitting the theoretical prediction of the thermal observables such as the $\tilde{\alpha}$ and Q^{-1} to the measured values.

In this way the part of thermal expansion mediated by magnetostriction can be effectively absorbed into the non-magnetic formalism simply by replacing α_E with $\tilde{\alpha}$. Together, the specific heat and thermal conductivity in the elastic and thermal dynamics equation (Eq. 3.10 and Eq. 3.12) should also be replaced by the total specific heat

$C_V = C_E + C_M$ and total thermal conductivity $\kappa = \kappa_E + \kappa_M$ [32]. The overall damping coefficient Q^{-1} for the elastic and magnetic hybrid plate has the form (Eq. 3.22)

$$Q^{-1} = \frac{1+\sigma}{1-\sigma} \frac{Y\tilde{\alpha}^2 T}{\rho C_V} \left(\frac{6}{\xi^2} - \frac{6}{\xi^3} \frac{\sinh\xi + \sin\xi}{\cosh\xi + \cos\xi} \right), \quad \xi = h\sqrt{\frac{\omega_0 \rho C_V}{2\kappa}}, \qquad (3.45)$$

with the $\tilde{\alpha}$, C_V, and κ are thermal observables which can be measured and predicted based on the theory developed in this chapter.

Furthermore, the magnetoelastic coupling of Eq. 3.37 can be rephrased as $F_{\text{MEC}} = Nz\rho\gamma_M J \langle \mathbf{S}_i \cdot \mathbf{S}_j \rangle \epsilon_i^i$ and for the Ising model it can be simplified into the spin correlation about $\hat{z}$ axis. Then the $F_{\text{MEC}} = Nz\rho\gamma_M J \langle S_i^z S_j^z \rangle \epsilon_i^i \equiv \Lambda L_z^2 \epsilon_i^i$ can be included into the Landau free energy that

$$F = F_0 + \left[a(T - T_N) + \Lambda\epsilon_i^i \right] L_z^2 + B L_z^4, \qquad (3.46)$$

and the Neel temperature at the influence of elastic strain is

$$T_N^* = T_N - \frac{\Lambda}{a}\epsilon_i^i. \qquad (3.47)$$

Since the proportionality Λ and Landau factor a are positive, we predict the decreasing of Neel temperature with the enhancing of plate strain ϵ_i^i [9].

3.4. Model validation through the thermal observables measured for the 2D AFM material FePS$_3$

Here we validate the theory developed in this chapter by calculating the linear thermal expansion coefficient α_L and damping factor Q^{-1} of the Ising-type 2D antiferromagnetic material FePS$_3$ whose phase transition temperature is about $T_N = 114K$ [9]. In the published paper (Ref. [9]), Šiškins and etc. have measured the vibration frequency of the base model f_0 for the membrane-plate of FePS$_3$ in the setup of Fig. 3.1. According to Ref. [38] the resonance frequency of the round resonator in the membrane-plate regime can be approximated by

$$f_0 = \sqrt{f_{\text{membrane}}^2 + f_{\text{plate}}^2}, \qquad (3.48)$$

in which the plate frequency is $f_{\text{plate}} = \omega_0/2\pi$ according to the Eq. 3.20 and the membranes fundamental frequency is

$$f_{\text{membranes}} = \frac{2.4048}{2\pi a} \sqrt{\frac{N}{\rho h}}, \qquad (3.49)$$

with $N = N_0 + Y h\epsilon_r^{\text{th}}/(1-\sigma)$ is the in-plane tension along radial direction. N_0 is the initial tension introduced by fabrication and can be further tuned by the external gate voltage V_G. The second part comes from the thermal expansion of the membranes which becomes a solely factor for the temperature dependency of the resonance frequency f_0 if we assume the plate frequency f_{plate} is independent to the environmental temperature
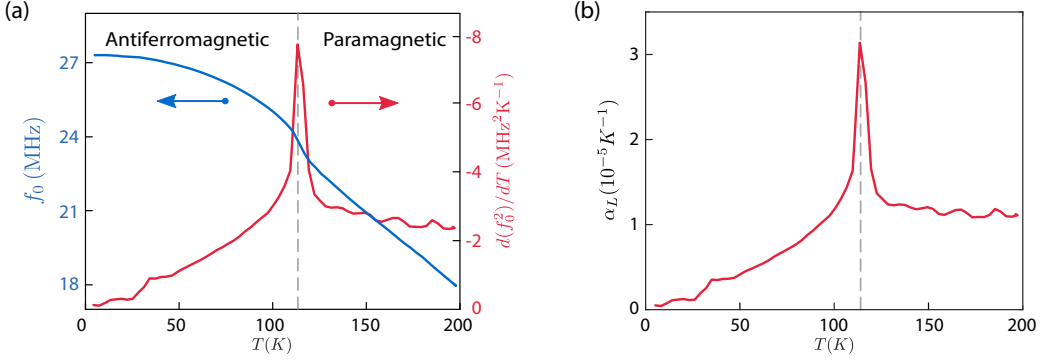
Figure 3.5: (a) Solid-blue line: the measured fundamental resonator frequency f_0 as function of temperature for the FePS$_3$ plate-membranes. Solid-red line: the derivative of f_0^2 to T. (b) Derived linear thermal expansion coefficient of FePS$_3$ plate-membranes according to Eq. 3.50. Quoted from the Fig.2 in Ref. [9].

because the Young's modulus Y and Poisson coefficient σ are almost independent to a small range of T varying from 0 to $200\,K$ in the Šiškins' experiment. The thermal strain is relate to the linear expansion coefficient of the resonator and silicon substrate by the relation $d\epsilon_r^{th}/dT = -(\alpha_L - \alpha_{si})$. As a consequence, by measuring the temperature dependency of $f_0(T)$ one can derive the thermal expansion coefficient of FePS$_3$ such that

$$\alpha_L = \alpha_{si} - \left(\frac{2\pi a}{2.4048}\right)^2 \frac{\rho(1-\sigma)}{Y}\frac{d(f_0^2)}{dT}. \tag{3.50}$$

The experimental measurement are presented in Fig. 3.5 and one indeed observes the α_L anomaly around the phase transition.

From the theoretical point of view, the linear expansion coefficient is one-third of the volume expansion coefficient developed in the previous section of the hybrid system, namely $\alpha_L = \tilde{\alpha}/3$ based on Eq. 3.43. In order to derive the theoretical prediction of α_L, one needs to calculate the specific heat of the elastic and magnetic parts. Firstly, for the magnetic specific of the Ising origin (Eq. 3.36), the effective coupling energy J' is derived from the measured Neel temperature $T_N = 114K$ and according to Eq. 3.35 we have $J' = 6.48\,$meV. Therefore the nearest neighbour spin-to-spin coupling energy in the Hamiltonian $H = -2J\sum S_i \cdot S_j$ has the value $J = J'/2S^2 = 0.81\,$meV since the atomic spin for FePS$_3$ is $S = 2$. One sees that the derived J is very close to the first-nearest neighbour interaction (shown in Fig. 3.6) $J_1 = 2J \approx 1.5\,$meV measured in the neutron scattering experiment [7, 8]. Using this derived J' we plot the C_{Is} in Fig. 3.3(b). Secondly, for the magnetic specific of the magnon origin (Eq. 3.28), it is necessary to figure out the exchange and anisotropy field on the sublattices in order to apply the dispersion relation in Eq. 3.27. However, according to the magnetostriction effect the inter-atomic interaction are modulated by the strain and varies with the membranes thickness [28]. Here we simplify the analysis by selecting the effective field as $\mu_0 H_E = 69\,$Tesla and $\mu_0 H_A = 138\,$Tesla in order to best fit the derived $C_M(T)$ and $\alpha_L(T)$ with the measured data. According to Eq. 1.21, the effective interaction between sublattices then becomes $J_{sub} \approx -1\,$meV and anisotropy is $A \approx 6\,$meV which are close to the measured data whose values take $J_2 = -0.04\,$meV, $J_3 = -0.96\,$meV, and $A = 3.78\,$meV as quoted from Refs. [7, 8]. The cal-
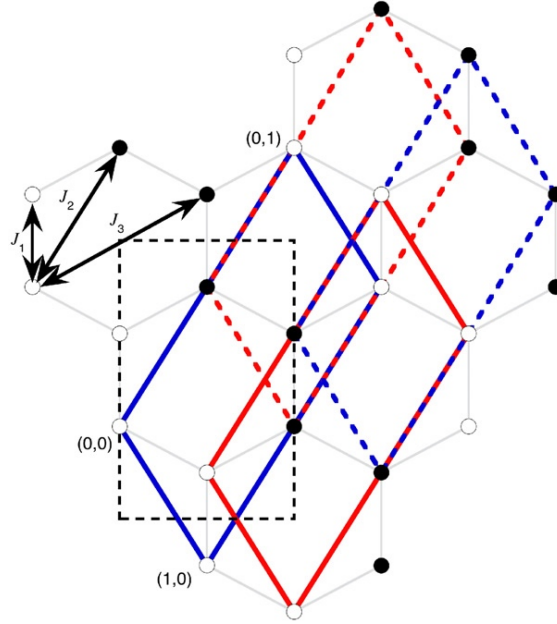
3

Figure 3.6: Schematic of the magnetic lattice for FePS$_3$ quoted from Ref. [8]. White dots mean the spin pointing out of the page and the black dots mean the spins pointing into the page. J_1, J_2, J_3 are the first-, second-, and third nearest neighbour interaction for the Hamiltonian $H = -\sum_{i,j} J_{i,j} \boldsymbol{S}_i \cdot \boldsymbol{S}_j$ [7]. The magnon dispersion relation with the effective exchange field is calculated based on the sub-lattice structure indicated by the red and blue rhombus. Total spin of magnetic Fe atom is $S = 2$ and the coordination number for sublattice is $z = 2$.

culated C_{mag} is shown in Fig. 3.2(a) and the total magnetic specific heat C_M is shown in Fig. 3.7(a). Obtained from first-principle calculation, the elastic parameters of FePS$_3$ are $Y = 103\,\text{GPa}$, $\sigma = 0.304$, $\rho = 3375\,\text{kg}\,\text{m}^{-3}$ and $\bar{v} = 3823\,\text{m}\,\text{s}^{-1}$ [9]. According to the Ref. [10], the elastic specific heat for FePS$_3$ is a mixing of Debye and Einstein parts with the Debye temperature $T_{\text{db}} = 236\,\text{K}$ and Einstein temperature $T_{\text{ei}} = 523\,\text{K}$. The suggested combination ratio is 0.54 and the elastic specific heat $C_E = (1 - 0.54)C_{\text{db}} + 0.54 C_{\text{ei}}$ can be derived from Eq. 3.25. In Fig. 3.7(b) we present the calculated C_E as doted blue line and the total specific heat $C_V = C_E + C_M$ as solid red line.

Our theoretical predictions fit well the measured data shown in Fig. 3.8 and therefore validate the choice of parameters and the applicability of our model. Furthermore, using these parameters we get the elastic Grüneisen factor $\gamma_E = 1.798$ based on Eq. 1.50 and the compressibility $\beta_T = 1.14 \times 10^{-11}\,\text{Pa}^{-1}$. By assuming the ratio $v = \gamma_M / \gamma_E = 4$ and applying the derived specific heats we calculate and plot the effective Grüneisen parameter $\tilde{\gamma}$ as function of temperature in Fig. 3.4. It is then straightforwards to derive the overall linear expansion coefficient for the hybrid system $\alpha_L = \tilde{\alpha}/3$ based on equation 3.43. Bear in mind that if one uses molar specific heat from the Fig. 3.7(b), the density should also chosen to be the molar density which is $\rho = 18443\,\text{mol}\,\text{m}^{-3}$ for FePS$_3$. Showing in Fig. 3.9 the theoretical prediction for α_L fits well the measured data which consolidates the scheme of merging the magnetoelastic coupling into the non-magnetic equation of motions for the hybrid system.
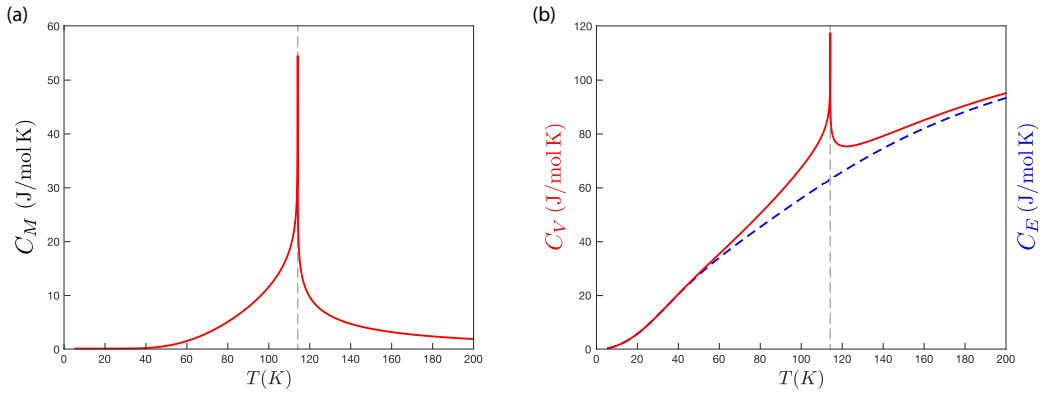
Figure 3.7: (a) Magnetic specific heat $C_M = C_{\text{Is}} + C_{\text{mag}}$ is the sum of the 2D Ising statistics and the magnon's contribution. (b) Solid red: total specific heat $C_V = C_E + C_M$ of the FePS$_3$. It shows anomaly around the phase transition because the divergence of magnetic C_M. Doted blue: the elastic specific heat $C_E = (1-0.54)C_{\text{db}} + 0.54C_{\text{ei}}$ according to Ref. [10]. We point out that there are 5 mol of atoms per 1 mol molecule for the FePS$_3$ compound.

3
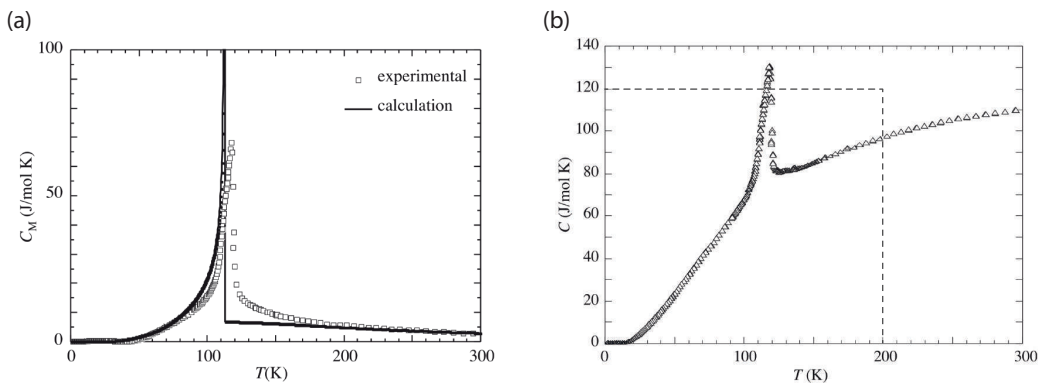
Figure 3.8: Measured Specific heat for FePS$_3$ quoted from Takano's paper [10]. (a) the experimental data and Takano's prediction for C_M. In his calculation, the magnetic specific heat instantly decays to zero which does not fits into the measurements whereas my plotting fits better. (b) the experimental data for the total specific heat. Note here the temperature ranges from 0 to 300 K while in my plotting the temperature stops at 200 K.

3
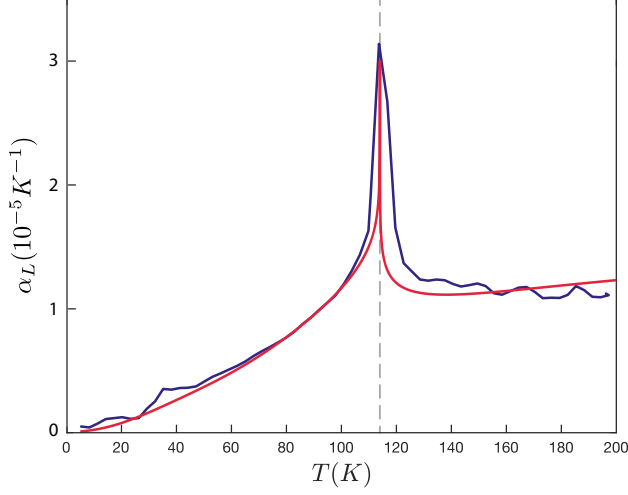
Figure 3.9: Solid red: theoretical predicted linear expansion coefficient $\alpha_L = \tilde{\alpha}/3$ based on the Eq. 3.43 with the derived specific heat from Fig. 3.7 and effective Grüneisen parameter $\tilde{\gamma}$ from Fig. 3.4. Solid blue: experimental derived α_L from Fig. 3.50(b).

In order to calculate and plot the damping coefficient Q^{-1} according to Eq. 3.45 one still needs to know the temperature dependence of thermal conductivity κ especially in the hybrid materials whose thermal conduction has several different origins. As for the FePS$_3$, we have $\kappa = \kappa_{\mathrm{ph}} + \kappa_{\mathrm{mag}}$ and we can ignore the scattering between phonons and magnons because the magnon's energy in antiferromagnetic is usually at the range of THz while the phonon's energy is usually of several GHz which means the coupling between these two quasi-particles is small. As stated in the previous section, particle lifetime is limited by the boundary scattering and can be treated as a constant $\tau = \tau_0$. The κ_{mag} can be derived according to Eq. 3.33 together with material constants and the fitting parameter $\tau_{0,\mathrm{mag}} \approx 3.8\,\mathrm{ps}$ [39]. As for the phonon's contribution, we simplify the analysis by utilizing the Debye averaged sound velocity and apply the fitting parameter $\tau_{0,\mathrm{ph}} \approx 0.8\,\mathrm{ps}$ such that $\kappa_{\mathrm{ph}} = C_E \bar{v}^2 \tau_{0,\mathrm{ph}}$. The total thermal conductivity is plotted in Fig. 3.10(a) and we see it is much smaller than the measured value for bulk FePS$_3$ compound which has $\kappa \approx 1\,\mathrm{W/mK}$ at room temperature [5]. This is due to the membranes geometry whose thickness is only $h = 45\,\mathrm{nm}$ which limits mobility of phonons and thus the small thermal conductivity. The transverse thermal time constant $\tau_z = h^2 \rho C_V / \pi \kappa$, which measures the time for establishing the temperature equilibrium across the plate, is also plotted and it is close to the Šiškins measurement. With the parameter $\xi = \pi \sqrt{f_0 \tau_z}$ and based on the previously derived expansion coefficient $\tilde{\alpha}$ and total specific heat C_V, we have the damping coefficient Q^{-1} derived and shown in Fig. 3.11. We see the agreement between theoretical prediction and experiment data is good enough and the drop of thermal transfer after phase transition can be ascribed to the depletion of magnons as thermal carriers.

(a)

(b)
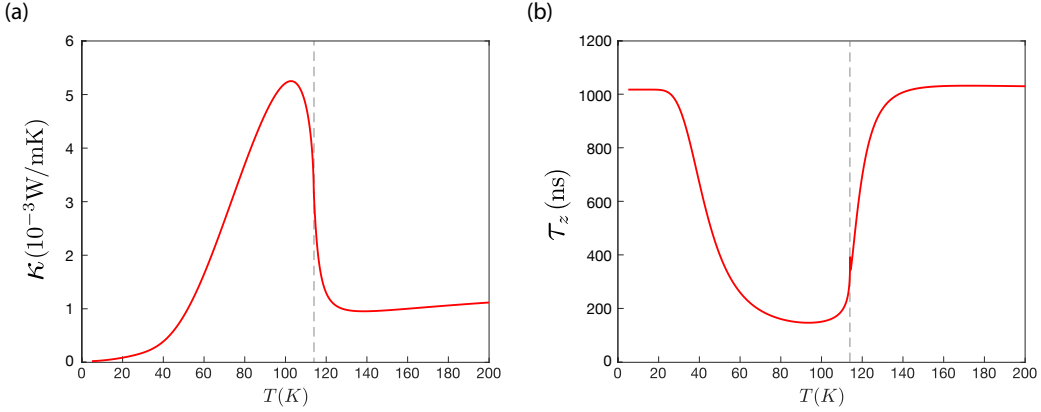
Figure 3.10: (a) Total thermal conductivity which is a sum of the phonon and magnons' contribution as thermal carriers $\kappa = \kappa_{\mathrm{ph}} + \kappa_{\mathrm{mag}}$. For the membranes setup the magnetic part dominates before the phase transition and vanishes afterwards. (b) The thermal time constant along the $\hat{z}$-th direction $\tau_z = h^2 \rho C_V / \pi \kappa$. The smaller of τ_z means the faster of temperature approaching equilibrium.
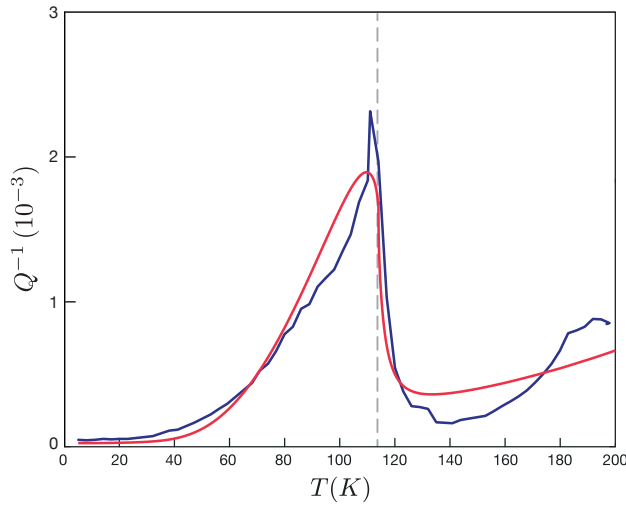
Figure 3.11: Solid red: theoretical prediction for damping coefficient Q^{-1} based on the Eq. 3.45 with FePS$_3$ material parameters stated in the main texts. Solid blue: experimentally measured curve quoted from Šiškins paper (Ref. [9]).

3.5.   Summary and outlook

In conclusion we studied the magnetoelastic effect on the thermal transfer within the thin AFM plate for a wide range of temperature across the magnetic phase transition. In specific, we developed a theory of merging the exchange magnetoelastic interaction into the thermal elastic free energy and further predicted the temperature dependence for observables such as specific heat C_V, linear expansion coefficient $\tilde{\alpha}$, and damping factor Q^{-1} for the quasi-2D Ising AFM material FePS$_3$. Compared to the experimentally measured data, our theoretical predictions agree very well especially for the specific heat and

3

linear expansion coefficient. As for the transport related property, the theoretical plot of $Q^{-1}(T)$ shows the overall trend consistent with the measured curve and it still has rooms for improvement. It is because in this work we have simplified the magnon and phonon velocity $\boldsymbol{v}_k$ to be homogeneous and utilized an isotropic thermal conductivity for analysis. According to the quasi 2D material these assumptions may not sufficient enough and one can improve these transport properties by studying the detailed lattice structure [8]. It may also helpful to find a double peak effect [40] for the $\kappa(T)$ is helpful to explain the secondary surging of Q^{-1} after $T > T_N$. However, our theoretical treatment builds a general scheme to study the thermal observables for the magnetic-elastic-thermal integrated system. The key is generalizing the Grüneisen relation by incorporating various contributions and arriving at an effective Grüneisen coefficient $\tilde{\gamma}$ (Eq. 3.44). This quantity essentially describes the variation of internal energy with respect to the volume change and its temperature dependency represents the changing of *weight* in the internal energy for each components in the hybrid system. Therefore the scheme developed in this chapter can be extended to include other contributors such as electrons in the spintronic and spin-caloritronic devices.

References

[1] C. Gong and X. Zhang, *Two-dimensional magnetic crystals and emergent heterostructure devices,* Science **363** (2019), 10.1126/science.aav4450.

[2] C. Gong, L. Li, Z. Li, H. Ji, A. Stern, Y. Xia, and etc., *Discovery of intrinsic ferromagnetism in two-dimensional van der waals crystals,* Nature **546**, 265 (2017).

[3] H. Li, S. Ruan, and Y.-J. Zeng, *Intrinsic van der waals magnetic materials from bulk to the 2D limit: New frontiers of spintronics,* Advanced Materials **31**, 1900065 (2019).

[4] S. R. Boona, R. C. Myers, and J. P. Heremans, *Spin caloritronics,* Energy Environ. Sci. **7**, 885 (2014).

[5] F. Kargar, E. A. Coleman, S. Ghosh, J. Lee, A. Balandin, and etc., *Phonon and thermal properties of quasi-two-dimensional FePS$_3$ and MnPS$_3$ antiferromagnetic semiconductors,* ACS Nano **14**, 2424 (2020).

[6] J.-U. Lee, S. Lee, J. H. Ryoo, S. Kang, T. Y. Kim, P. Kim, C.-H. Park, J.-G. Park, and H. Cheong, *Ising-type magnetic ordering in atomically thin FePS$_3$,* Nano Letters **16**, 7433 (2016).

[7] D. Lançon, H. C. Walker, E. Ressouche, B. Ouladdiaf, K. C. Rule, G. J. McIntyre, T. J. Hicks, H. M. Rønnow, and A. R. Wildes, *Magnetic structure and magnon dynamics of the quasi-two-dimensional antiferromagnet FePS$_3$,* Phys. Rev. B **94**, 214407 (2016).

[8] A. R. Wildes, K. C. Rule, R. I. Bewley, M. Enderle, and T. J. Hicks, *The magnon dynamics and spin exchange parameters of FePS$_3$,* Journal of Physics: Condensed Matter **24**, 416004 (2012).

[9] M. Šiškins, M. Lee, S. Mañas-Valero, and et al, *Magnetic and electronic phase transitions probed by nanomechanical resonators,* Nature Communication **11**, 2698 (2020).

[10] Y. Takano, N. Arai, A. Arai, Y. Takahashi, K. Takase, and K. Sekizawa, *Magnetic properties and specific heat of MPS₃ (M=Mn, Fe, Zn),* Journal of Magnetism and Magnetic Materials **272-276**, E593 (2004).

[11] L. D. Landau and E. M. Lifshitz, *Chapter ii - the equilibrium of rods and plates,* in *Theory of Elasticity* (Butterworth-Heinemann, 1986) third edition ed., pp. 38–86.

[12] C.-H. Huang, *Transverse vibration analysis and measurement for the piezoceramic annular plate with different boundary conditions,* Journal of Sound and Vibration **283**, 665 (2005).

[13] Y. Sun and H. Tohmyoh, *Thermoelastic damping of the axisymmetric vibration of circular plate resonators,* Journal of Sound and Vibration **319**, 392 (2008).

[14] J. W. McPherson, *Heat Generation and Dissipation* (Springer International Publishing, 2019).

[15] R. Lifshitz and M. L. Roukes, *Thermoelastic damping in micro- and nanomechanical systems,* Phys. Rev. B **61**, 5600 (2000).

[16] S. M. Rezende, R. L. Rodríguez-Suárez, J. C. Lopez Ortiz, and A. Azevedo, *Thermal properties of magnons and the spin seebeck effect in yttrium iron garnet/normal metal hybrid structures,* Phys. Rev. B **89**, 134406 (2014).

[17] K. Shen, *Finite temperature magnon spectra in yttrium iron garnet from a mean field approach in a tight-binding model,* New Journal of Physics **20**, 043025 (2018).

[18] S. H. Simon, *The Oxford Solid State Basics* (Oxford University Press, 2016).

[19] J. C. López Ortiz, G. A. Fonseca Guerra, F. L. A. Machado, and S. M. Rezende, *Magnetic anisotropy of antiferromagnetic RbMnF₃,* Phys. Rev. B **90**, 054402 (2014).

[20] P. H. Cole and W. J. Ince, *Equilibrium spin configuration and resonance behavior of RbMnF3,* Phys. Rev. **150**, 377 (1966).

[21] X. Wang, K. Du, Y. Y. F. Liu, P. Hu, J. Zhang, Q. Zhang, M. H. S. Owen, X. Lu, C. K. Gan, P. Sengupta, C. Kloc, and Q. Xiong, *Raman spectroscopy of atomically thin two-dimensional magnetic iron phosphorus trisulfide (FePS₃) crystals,* 2D Materials **3**, 031009 (2016).

[22] S. M. Rezende, A. Azevedo, and R. L. Rodríguez-Suárez, *Introduction to antiferromagnetic magnons,* Journal of Applied Physics **126**, 151101 (2019).

[23] J. M. D. Coey, *Magnetism and Magnetic Materials* (Cambridge University Press, 2010).

[24] N. G. S. Verma, *Phonon conductivity of trivalent rare-earth-doped gallium and aluminium garnets,* Phys. Rev. B **6**, 3509 (1972).

[25] C. Kittel, *Introduction to Solid State Physics*, eighth edition ed. (John Wiley, 2004).

3

[26] S. M. Rezende, R. L. Rodríguez-Suárez, R. O. Cunha, A. R. Rodrigues, F. L. A. Machado, G. A. Fonseca Guerra, J. C. Lopez Ortiz, and A. Azevedo, *Magnon spin-current theory for the longitudinal spin-seebeck effect,* Phys. Rev. B **89**, 014416 (2014).

[27] R. J. Dolleman, S. Houri, D. Davidovikj, S. J. Cartamil-Bueno, Y. M. Blanter, H. S. J. van der Zant, and P. G. Steeneken, *Optomechanics for thermal characterization of suspended graphene,* Phys. Rev. B **96**, 165421 (2017).

[28] J. M. Zhang, Y. Z. Nie, X. G. Wang, Q. L. Xia, and G. H. Guo, *Strain modulation of magnetic properties of monolayer and bilayer FePS$_3$ antiferromagnet,* Journal of Magnetism and Magnetic Materials **525**, 167687 (2021).

[29] R. Houtappel, *Order-disorder in hexagonal lattices,* Physica **16**, 425 (1950).

[30] R. Pathria and P. D. Beale, *Statistical Mechnics* (Elsevier, 2011).

[31] V. Matveev and R. Shrock, *Complex-temperature singularities in the d = 2 ising model: triangular and honeycomb lattices,* Journal of Physics A: Mathematical and General **29**, 803 (1996).

[32] N. Prasai, B. A. Trump, G. G. Marcus, A. Akopyan, S. X. Huang, T. M. McQueen, and J. L. Cohn, *Ballistic magnon heat conduction and possible poiseuille flow in the helimagnetic insulator Cu$_2$OSeO$_3$,* Phys. Rev. B **95**, 224407 (2017).

[33] B. E. Argyle, N. Miyata, and T. D. Schultz, *Magnetoelastic behavior of single-crystal Europium Oxide. I. thermal expansion anomaly,* Phys. Rev. **160**, 413 (1967).

[34] Y. Shapira and N. F. Oliveira, *Magnetostriction, magnetoelastic coupling, and the magnetic Grüneisen constant in the antiferromagnet RbMnF$_3$,* Phys. Rev. B **18**, 1425 (1978).

[35] Y. Shapira, R. D. Yacovitch, C. C. Becerra, S. Foner, E. J. McNiff, D. R. Nelson, and L. Gunther, *Magnetostriction and the two-spin correlation function in EuO,* Phys. Rev. B **14**, 3007 (1976).

[36] G. O. Gomes, L. Squillante, A. C. Seridonio, A. Ney, R. E. Lagos, and M. de Souza, *Magnetic Grüneisen parameter for model systems,* Phys. Rev. B **100**, 054446 (2019).

[37] D. B. McWhan, P. C. Souers, and G. Jura, *Magnetic and structural properties of europium metal and europium monoxide at high pressure,* Phys. Rev. **143**, 385 (1966).

[38] A. Castellanos-Gomez, R. van Leeuwen, M. Buscema, H. S. J. van der Zant, G. A. Steele, and W. J. Venstra, *Single-layer mos2 mechanical resonators,* Advanced Materials **25**, 6719 (2013).

[39] X. Wu, Z. Liu, and T. Luo, *Magnon and phonon dispersion, lifetime, and thermal conductivity of iron from spin-lattice dynamics simulations,* Journal of Applied Physics **123**, 085109 (2018).

[40] Y. Ando, J. Takeya, D. L. Sisson, S. G. Doettinger, I. Tanaka, R. S. Feigelson, and A. Kapitulnik, *Thermal conductivity of the spin-peierls compound CuGeO$_3$,* Phys. Rev. B **58**, R2913 (1998).

4

Chiral coupling of magnons in waveguides

The secret of happiness, you see, is not found in seeking more,
but in developing the capacity to enjoy less.

Socrates

In this chapter we theoretically investigate the collective excitations of multiple millimeter-sized ferromagnetic spheres mediated by waveguide photons. By the position of the magnets in the waveguide, the magnon-photon coupling can be tuned to be chiral, i.e., magnons only couple with photons propagating in one direction, leading to an asymmetric transfer of angular momentum and energy between the magnets. A large concentration of the magnon's population can be achieved at an edge of long chain of magnets. The chain also supports standing waves with low radiation efficiency that are inert to the chirality.

4.1. Introduction

Magnetic insulators are promising materials for low dissipation information technology with magnons, the elementary excitation of magnetic order, rather than electrons [2–5]. The long lifetime of magnons in high-quality magnetic insulators such as yttrium iron garnet (YIG) [6] are suitable for data storage, logic, and medium-distance interconnects but cannot compete with photons in terms of speed and coherence lengths. Coupled magnon-photon systems are therefore promising for quantum communication over large distances [7]. The interface to conventional electronics are metal contacts that allow magnons to interact with conduction electrons by interfacial exchange interaction, giving rise to spin pumping and spin transfer torques [8, 9]. Magnons in separate nanomagnets couple by the long-range dipolar interaction, giving rise to chiral transport phenomena [10–12].

Strong coherent coupling between photons in high-quality cavities and spin ensembles such as NV centers in diamond [13, 14], rare earth ions [15, 16], and ferromagnets [17, 18], is attractive because of its potential for quantum memories [19] and transducers. While a (nearly) closed cavity can have very long photon lifetimes, efficient photon transport requires an open waveguide, the main object of the present study. Coherent microwave emission from a precessing magnetization of a ferromagnet in a waveguide can be measured via the additional damping of magnons [20–22] on top of the intrinsic Gilbert damping. The Larmor precession of the magnetization couples preferentially to photons with the same polarization. Due to the tunable ellipticity of the AC magnetic field, magnets at certain locations in a waveguide (to be discussed in the main text) also couple preferentially to photons propagating in one direction. Such a chiral coupling of atoms and quantum dots with optical photons attracts much attention [23, 24].

Here we study a collection of magnetic particles placed in a microwave waveguide [21, 25], as shown in Fig. 4.1. The radiation emitted by a magnet typically drives all the other magnets, leading to an effective long-range dissipative coupling, reminiscent of the coherent coupling in a closed cavity [19]. The coupling mediated by travelling photons in atomic ensembles [26–30] causes collective super- and sub-radiance. Here, we discuss analogous modes in macroscopic magnonic systems but with incorporating the chirality, which can be probed by microwaves at room temperature.

We show magnets can couple chirally to waveguide photons, leading to the non-reciprocal magnon-magnon interaction [23]. For given locations in a waveguide, one magnet can affect another one without back-action [24]. We predict the imbalance of the magnon population in a chain of magnets that can be significantly enhanced up to several order of magnitude. We study the collective excitations of up to ~ 100 magnets, with focusing on super-radiant and sub-radiant modes, i.e. modes with very higher or lower radiation efficiency than the independent one [31]. We find that the superradiant states [26–30] are well localized at the edge of the chain [26, 32]. In contrast, the lowest subradiant states are standing-wave–like and centered in the chain and are only weakly affected by the chirality of the coupling. Here we formulate the theory for the physical properties of the collective modes for one, two and many spheres in a waveguide, such as the microwave transmission spectra.

This chapter is organized as follows. We introduce the model in Sec. 4.2 including the Hamiltonian for subsystems and especially calculate the magnon-photon coupling con-
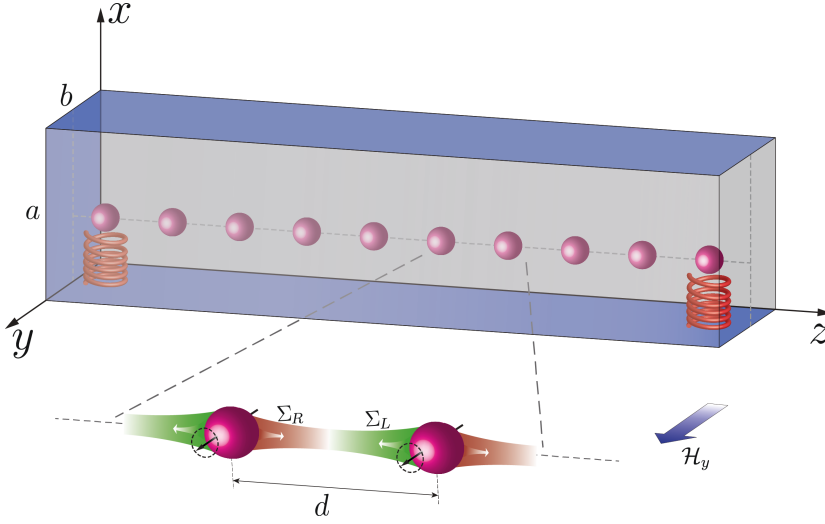
Figure 4.1: Chain of magnetic spheres with period d in a microwave waveguide. The chain and waveguide are parallel to the $\hat{z}$ axis and magnetizations are oriented along $\hat{y}$ axis by a magnetic field H_y. Every magnet interacts with all other magnets to the right (Σ_R) and to the left (Σ_L). Small coils attached to magnet can excite and detect the local magnon accumulation.

stants. Based on the input-out theory, in Sec. 4.3 we derived the photon scattering matrix for a general waveguide geometry and positions of the magnets. As an example we focus on magnon-photon coupling in a rectangular waveguide in Sec. 4.4. We specifically address the coupling constants and radiative damping of magnet in this case. We derive collective modes with super- and sub-radiance in long magnetic chains in Sec. 4.5. Finally, Sec. 4.6 contains a discussion of the results and conclusions.

4.2. Model description

We focus here on magnets that are small enough compared with the photon wavelength such that only the homogeneous collective excitation or Kittel mode couples with the microwave photon [33]. We consider a waveguide infinite in the z-direction with a rectangular cross-section from $(0,0)$ to (a, b), as shown in Fig. 4.1. We assume metallic boundaries, i.e. the electric field parallel to the surface vanishes. There are N equivalent magnets with gyromagnetic ratio $-\gamma$, saturated magnetization M_s, and volume V_s. Their centers are located at $\boldsymbol{r}_i = (\boldsymbol{\rho}_i, z_i)$, where $\boldsymbol{\rho} = (x, y)$ is the position in the waveguide's cross-section.

The dynamics is governed by the Hamiltonian $\hat{H} = \hat{H}_{\text{EM}} + \hat{H}_{\text{M}} + \hat{H}_{\text{int}}$, with electromagnetic contribution

$$\hat{H}_{\text{EM}} = \int \left[\frac{\epsilon_0}{2} E^2(\boldsymbol{r}) + \frac{\mu_0}{2} H^2(\boldsymbol{r}) \right] d\boldsymbol{r}, \tag{4.1}$$

the magnetic part

$$\hat{H}_{\text{M}} = -\mu_0 \int \left[H_0(\boldsymbol{r}) M_y(\boldsymbol{r}) + \boldsymbol{H}_1(\boldsymbol{r}) \cdot \boldsymbol{M}(\boldsymbol{r}) \right] d\boldsymbol{r}, \tag{4.2}$$

and the magnon-photon interaction

$$\hat{H}_{\text{int}} = -\mu_0 \int \boldsymbol{H}(\boldsymbol{r}) \cdot \boldsymbol{M}(\boldsymbol{r}) \, d\boldsymbol{r}. \tag{4.3}$$

The time-dependence is implicit. Here, $\{\boldsymbol{E}, \boldsymbol{H}\}$ represent the electric and magnetic fields of the photons in the waveguide, $\boldsymbol{H}_1$ is the sum of dipolar and anisotropy field [34]. For simplicity we assume it is much smaller than the external saturating field, $H_0 \gg H_1$, so that it can be ignored. $\boldsymbol{M}$ is the magnetization, ϵ_0 and μ_0 are the permittivity and permeability of the free space, and $H_0 \hat{\boldsymbol{y}}$ denotes the static applied field that saturates the magnetizations.

The electromagnetic fields can be expanded in photon operators,

$$\boldsymbol{H}(\boldsymbol{r}) = \sum_{k,\lambda} \left(\boldsymbol{\mathcal{H}}_k^\lambda(\boldsymbol{\rho}) e^{ikz} \hat{p}_k^\lambda + \text{h.c.} \right), \tag{4.4}$$

with $\boldsymbol{\mathcal{H}}_k^\lambda(\boldsymbol{\rho})$ being the eigenmodes for the magnetic field in the waveguide [35], and similarly for the electric field with $\boldsymbol{H} \to \boldsymbol{E}$ and $\boldsymbol{\mathcal{H}} \to \boldsymbol{\mathcal{E}}$ (Eq. 1.67). Here k denotes the momentum in the $\boldsymbol{z}$-direction, and λ is the mode index. The photon operators satisfy the field commutation relations

$$\left[\hat{p}_k^\lambda, \hat{p}_{k'}^{\lambda'\dagger} \right] = \delta(k - k')\delta_{\lambda\lambda'}. \tag{4.5}$$

By proper normalization (Eq. 1.68) the Hamiltonian for EM field can be rephrased into (up to a constant)

$$\hat{H}_{\text{EM}} = \hbar \sum_{k,\lambda} \Omega_k^\lambda \hat{p}_k^{\lambda\dagger} \hat{p}_k^\lambda, \tag{4.6}$$

with the photon frequency

$$\Omega_k^\lambda = c\sqrt{\gamma_\lambda^2 + k^2}, \tag{4.7}$$

and c is the speed of light in vacuum. We assume the losses in high-quality waveguide to be small compared to the magnetic dissipation and not important on the length scale of interest.

The magnetization $\boldsymbol{M}(\boldsymbol{r})$ is confined to the magnets that are much smaller than typical photon wavelengths and waveguide dimensions (usually > 1 cm), such that the magnetic field is a constant inside each magnet. The excitations of the (linearized) magnetic Hamiltonian are spin waves, or its quanta, magnons. For magnets with axial symmetry around the magnetization, the microwaves couple strongly only with the Kittel mode, i.e. the uniform precession of the magnetization and we disregard other modes in the following. We quantize the magnetization as [36, 37]

$$M_{j,z} - iM_{j,x} = \sqrt{\frac{2\hbar\gamma M_s}{V_s}} \hat{\beta}_j,$$

$$M_{j,z} + iM_{j,x} = \sqrt{\frac{2\hbar\gamma M_s}{V_s}} \hat{\beta}_j^\dagger, \tag{4.8}$$

$$M_{j,y} = M_s - \frac{\hbar\gamma}{V_s} \hat{\beta}_j^\dagger \hat{\beta}_j,$$

where $\hat{\beta}_j$ is the annihilation operator for a Kittel magnon in the j-th magnet with $j \in \{1,\ldots,N\}$. The coefficients are chosen to ensure that $\boldsymbol{M}_j \cdot \boldsymbol{M}_j \approx M_s^2$ and the magnetic Hamiltonian Eq. (4.2), up to a constant becomes

$$\hat{H}_{\mathrm{M}} = \hbar \sum_{j=1}^{N} \omega_j \hat{\beta}_j^\dagger \hat{\beta}_j, \qquad \omega_j = \gamma \mu_0 H_0(\boldsymbol{r}_j). \tag{4.9}$$

Inserting Eqs. (4.6) and (4.9) into the interaction Hamiltonian the equation 4.3 becomes

$$\hat{H}_{\mathrm{int}} = \hbar \sum_j \sum_{k,\lambda} \left[g_j^\lambda(k) \hat{p}_k^\lambda \hat{\beta}_j^\dagger + \mathrm{h.c.} \right], \tag{4.10}$$

with the coupling constant

$$g_j^\lambda(k) = \mu_0 \sqrt{\frac{\gamma M_s V_s}{2\hbar}} \left[i \mathcal{H}_x^\lambda(k) - \mathcal{H}_z^\lambda(k) \right] e^{ikz_j}. \tag{4.11}$$

The chirality of coupling $g(k) \neq g(-k)$ arises based on the non-symmetric reflection of EM wave travelling in $\pm k$ as shown in Eq. 1.66. In physics, this reflects this coupling is of angular momentum conservation such that the counter-clockwise precession of spins only couples to the counter-clockwise polarization of EM waves. If the magnetic field is circular polarized then this coupling is fully chiral, while if the magnetic field is elliptical polarized the coupling is partially chiral. The distributed magnets experience different phases along the waveguide longitudinal position and we can tune this coupling strength and chirality by the position of the magnets $\boldsymbol{\rho}_j$. One can see in the sec 4.4 that in rectangular waveguide the coupling constant can be written into the form of $g_j^\lambda(k) = i e^{ikz_j} \tilde{g}_j^\lambda(k)$ with the $\tilde{g}_j^\lambda(k)$ is real number.

4.3. Photon mediated interaction between magnetic spheres

From the Hamiltonian $\hat{H} = \hat{H}_{\mathrm{em}} + \hat{H}_{\mathrm{m}} + \hat{H}_{\mathrm{int}}$, we obtain the equation of motion for photons by the Heisenberg relation $\dot{\hat{\mathcal{O}}} = -i[\hat{\mathcal{O}}, \hat{H}]$,

$$\frac{d\hat{p}_k^\lambda}{dt} = -i\Omega_k^\lambda \hat{p}_k^\lambda - i \sum_j \tilde{g}_j^\lambda(k) \hat{\beta}_j. \tag{4.12}$$

The symbolic solution is

$$\hat{p}_k^\lambda(t) = \hat{p}_{k,\mathrm{in}}^\lambda e^{-i\Omega_k^\lambda t} - \sum_j i \tilde{g}_j^\lambda(k) \int_{-\infty}^{t} \hat{\beta}_j(\tau) e^{-i\Omega_k^\lambda(t-\tau)} d\tau, \tag{4.13}$$

where $\hat{p}_k(-\infty) \equiv \hat{p}_{k,\mathrm{in}}^\lambda$ is the microwave input [38, 39]. The first term is the free evolution and the second term is the (spontaneous and stimulated) radiation generated by magnons. The output field $\hat{p}_{k,\mathrm{out}}^\lambda = \lim_{t\to\infty} \hat{p}_k^\lambda(t) e^{i\Omega_k^\lambda t}$ then reads

$$\hat{p}_{k,\mathrm{out}}^\lambda = \hat{p}_{k,\mathrm{in}}^\lambda - i \sum_j \tilde{g}_j^\lambda \int_{-\infty}^{\infty} \hat{\beta}_j(\tau) e^{i\Omega_k^\lambda \tau} d\tau. \tag{4.14}$$

The magnon dynamics is governed by equation of motion

$$\frac{d\hat{\beta}_j}{dt} = -i\omega_j\hat{\beta}_j - \hat{\mathcal{D}}_{\text{int},j} - \hat{\mathcal{D}}_{\text{ph},j}, \tag{4.15}$$

where

$$\hat{\mathcal{D}}_{\text{int},j} = \frac{\kappa_j}{2}\hat{\beta}_j, \qquad \hat{\mathcal{D}}_{\text{ph},j} = i\sum_{k,\lambda} g_j^\lambda(k)\hat{p}_k^\lambda. \tag{4.16}$$

This is equivalent to the linearized Landau-Lifshitz-Gilbert (LLG) equation. Here the linewidth $\kappa_j = 2\alpha_G\omega_j$, where α_G is the Gilbert damping parameter. Each magnet is connected to an intrinsic bath of phonons and other magnons, which generates the thermal torque. However, in our model we assume this interaction is Markovian and all magnons are Gibbs distributed at equilibrium [38], leading to the vanishing thermal torque in the intrinsic damping.

When magnons are coupled by photons, the torque $\hat{\mathcal{D}}_{\text{ph},j}$ can be split as

$$\hat{\mathcal{D}}_{\text{ph},j}(t) = \hat{T}_j(t) + i\sum_l \int_{-\infty}^t d\tau\,\tilde{\Sigma}_{jl}(t-\tau)\hat{\beta}_l(\tau), \tag{4.17}$$

where the first term is generated by the photon input,

$$\hat{T}_j(t) = i\sum_{k,\lambda} g_j^\lambda(k)\hat{p}_{k,\text{in}}^\lambda e^{-i\Omega_k^\lambda t}, \tag{4.18}$$

while the second term describes the photon-mediated coupling

$$\tilde{\Sigma}_{jl}(t-\tau) = -i\sum_{k,\lambda} g_j^\lambda(k)\bar{g}_l^\lambda(k)e^{-i\Omega_k^\lambda(t-\tau)}, \tag{4.19}$$

which can be interpreted as (real or virtual) (k,λ)-mode photon emission from magnet l with amplitude $\bar{g}_l^\lambda(k)$ followed by the absorption in magnet j with amplitude $g_j^\lambda(k)$. The interaction is retarded by the finite light velocity. However, even for large distances $r_{jl} < 1$ m, $\kappa_j r_{jl}/c < 0.02$, where $\kappa_j = 2\pi \times 1\,\text{MHz}$ is a typical magnon linewidth, so $\tilde{\Sigma}_{jl}(t-\tau)$ decays much faster than the magnon envelope dynamics. For short times $|t-\tau| < r_{jl}/c$ the magnons can be assumed to move coherently $\hat{\beta}_l(\tau) \approx \hat{\beta}_l(t)e^{i\omega_l(t-\tau)}$. This Markovian approximations simplifies Eq. (4.15) to

$$\frac{d\hat{\mathscr{B}}}{dt} = -i\tilde{\omega}\hat{\mathscr{B}} - i\Sigma\hat{\mathscr{B}} - \hat{\mathscr{T}}, \tag{4.20}$$

introducing the column vectors for local magnetization $\hat{\mathscr{B}} = (\hat{\beta}_1,\ldots,\hat{\beta}_N)^T$, and the (microwave) torque

$$\hat{\mathscr{T}} \equiv (\hat{T}_1,\cdots,\hat{T}_N)^T = i\sum_{k,\lambda} \hat{p}_{k,\text{in}}^\lambda e^{-i\Omega_k^\lambda t}\mathscr{G}_k^\lambda, \tag{4.21}$$

according to the coupling vector $\mathscr{G}_k^\lambda = (g_1^\lambda(k),\ldots,g_N^\lambda(k))^T$. A local antenna such as metal-wire coils close to each sphere [19] can locally excite or detect its dynamics, leading to

the distributed torque $\hat{\mathcal{T}} \to \hat{\mathcal{T}} + \hat{\mathcal{T}}_l$, where $\hat{\mathcal{T}}_l = (\hat{P}_1, \cdots, \hat{P}_N)^T$ and $\hat{P}_i$ is the local input amplitude. The elements of the matrices $\tilde{\omega}$ and Σ read

$$\tilde{\omega}_{jl} = \delta_{jl}\left(\omega_j - i\frac{\kappa_j}{2}\right), \tag{4.22}$$

$$\Sigma_{jl} = \int_0^{\infty} \tilde{\Sigma}_{jl}(t) e^{i\omega_l t} dt. \tag{4.23}$$

Inserting $\tilde{\Sigma}$, we obtain the magnon self-energy

$$\Sigma_{jl} = \sum_{k,\lambda} \frac{g_j^{\lambda}(k)\bar{g}_l^{\lambda}(k)}{\omega_l - \Omega_k^{\lambda} + i0^+}. \tag{4.24}$$

According to (Eq. 4.20), the $\mathrm{Re}\Sigma$ modulates the frequencies of each magnet by the other magnets (coherent coupling), while the $\mathrm{Im}\Sigma$ changes their damping rate (dissipative coupling).

The diagonal elements of the coupling Σ_{jj} in Eq. (4.24) are magnet's self-interaction that shifts the frequencies by a small amount ($\mathrm{Re}\Sigma_{jj} \ll \omega_j$ as shown below) and also describe the radiative damping by $\mathrm{Im}\Sigma_{jj}$. The non-diagonal elements $\Sigma_{i\neq l}$ couple different magnets. Taking the complex integral of k that $\sum_k = \frac{1}{2\pi}\int dk$ and using residual theorem, we obtain the effective coupling from magnet l to magnet j as

$$\Sigma_{jl} = \sum_{\lambda}^{\mathrm{Im}k_l^{\lambda}=0} \begin{cases} -i\left(\Sigma_L^{\lambda} + \Sigma_R^{\lambda}\right)/2 - \delta\omega_j^{\lambda}, & j = l \\ -i\Sigma_R^{\lambda} e^{ik_l^{\lambda}(z_j - z_l)}, & z_j > z_l \\ -i\Sigma_L^{\lambda} e^{ik_l^{\lambda}(z_l - z_j)}, & z_j < z_l \end{cases} \tag{4.25}$$

The summation till $\mathrm{Im}k_l^{\lambda} = 0$ limits over the λ's for which $k_l^{\lambda} = \sqrt{\omega_l^2/c^2 - \gamma_{\lambda}^2}$ is real, i.e. the frequency of the l-th magnet is larger than the λ-band edge. The frequency shift for magnet j by the photon band λ is calculated to be

$$\delta\omega_j^{\lambda} = \frac{\gamma\mu_0 M_s V_s k_c}{ab} \sin^2\left(\gamma_x^{\lambda} x_j\right) \cos^2\left(\gamma_y^{\lambda} y_j\right), \tag{4.26}$$

where k_c is an upper cut-off for the wave numbers, which is typically governed by high-frequency losses in the boundaries. For typical electron relaxation time in copper, $\tau_{\mathrm{el}} = 50$ fs ($\Omega_c \sim 2\pi \times 20$ THz) [40], $k_c = 2\pi/(\tau_{\mathrm{el}}c) \sim 10^5$ m^{-1} and $\delta\omega_j^{\lambda} \lesssim 2\pi \times 100$ MHz for $a \sim b \sim 2$ cm and the sphere radius of 0.5 mm, which is much smaller than the Kittel mode frequency $\omega_j \sim 2\pi \times 10$ GHz. Taking the $-ie^{-ikz_j}g_j^{\lambda} = \left|g_j^{\lambda}\right| \equiv \tilde{g}_j^{\lambda}$, the rightwards and leftwards inter-magnets coupling magnitude is calculated to be

$$\Sigma_R^{\lambda} = \frac{\tilde{g}_j^{\lambda}\left(k_l^{\lambda}\right)\tilde{g}_l^{\lambda}\left(k_l^{\lambda}\right)}{v^{\lambda}\left(k_l^{\lambda}\right)}, \qquad \Sigma_L^{\lambda} = \frac{\tilde{g}_j^{\lambda}\left(-k_l^{\lambda}\right)\tilde{g}_l^{\lambda}\left(-k_l^{\lambda}\right)}{v^{\lambda}\left(-k_l^{\lambda}\right)}. \tag{4.27}$$

Here the photon group velocity derived from dispersion relation (Eq. 4.7) is

$$v^{\lambda}(k) = \left|\frac{d\Omega_k^{\lambda}}{dk}\right| = c^2\frac{|k|}{\Omega_k^{\lambda}}. \tag{4.28}$$

4.3.1. Collective modes

The coupling between magnets by photon exchange in the waveguide gives rise to collective excitations. In the language of quantum optics [26, 28], it can be interpreted as an effective non-Hermitian Hamiltonian between magnons, $\hat{H}_{\text{eff}} = \hbar \hat{\mathscr{B}}^\dagger \tilde{H}_{\text{eff}} \hat{\mathscr{B}}$ and matrix

$$\tilde{H}_{\text{eff}} = (\tilde{\omega} + \Sigma), \tag{4.29}$$

with which (ignore input $\hat{\mathscr{T}}$) its Heisenberg equation of motion would recover the magnon dynamics as in equation 4.20. Since the Hamiltonian is of non-Hermitian these couplings are dissipative and the level attraction in the transmission spectrum can be expected. In general, any two systems coupled via continuous travelling waves are dissipatively coupled.

The right and left eigenvectors of the non-Hermitian $\tilde{H}_{\text{eff}}$ are not the same. Let the right eigenvectors of $\tilde{H}_{\text{eff}}$ to be $\{\psi_\zeta\}$ with corresponding eigenvalues $\{v_\zeta\}$ where $\zeta \in \{1,\ldots,N\}$ labels the collective modes. It is also convenient to define the right eigenvectors of $\tilde{H}_{\text{eff}}^\dagger$ as $\{\phi_\zeta\}$ with corresponding eigenvalues $\{\bar{v}_\zeta\}$. Without degeneracies, i.e. $\forall \zeta \zeta'$ $v_\zeta \neq v_{\zeta'}$, we have bi-orthonormality $\psi_\zeta^\dagger \phi_\zeta' = \phi_\zeta^\dagger \psi_\zeta' = \delta_{\zeta\zeta'}$ after normalization. It is easy to prove then $\phi_\zeta^\dagger$ is a left eigenvector of $\tilde{H}_{\text{eff}}$, i.e. $\psi_\zeta^\dagger \tilde{H}_{\text{eff}} = v_\zeta \psi_\zeta^\dagger$. The non-uniqueness of the normalization condition does not affect the observables.

Defining matrices $\mathscr{L} = (\phi_1,\ldots,\phi_N)$ and $\mathscr{R} = (\psi_1,\ldots,\psi_N)$ in terms of left and right eigenvectors, the bi-orthonormality $\mathscr{R}^\dagger \mathscr{L} = \mathscr{L}^\dagger \mathscr{R} = \mathscr{I}_N$, where $\mathscr{I}_N$ is the $N \times N$ identity matrix, leads to

$$\tilde{\omega} + \Sigma = \mathscr{R} v \mathscr{L}^\dagger, \tag{4.30}$$

with matrix elements $v_{ij} = (v_1,\ldots,v_N)\delta_{ij}$. Defining the collective mode operator

$$\hat{\alpha}_\zeta = \phi_\zeta^\dagger \hat{\mathscr{B}}, \tag{4.31}$$

$\hat{\alpha}_\zeta$ annihilates a quasiparticle in a collective mode with "wave function"ψ_ζ. Introduce the column vector for collective excitations $\hat{\alpha} = (\hat{\alpha}_1,\ldots,\hat{\alpha}_N)^T$ it relation with the local magnon excitation can succinct to be $\hat{\alpha} = \mathscr{L}^\dagger \hat{\mathscr{B}}$. As an inverse transformation, the magnetization follows from the right eigenvectors

$$\hat{\mathscr{B}}(t) = \sum_\zeta \psi_\zeta \hat{\alpha}_\zeta(t) \quad \rightarrow \quad \hat{\mathscr{B}} = \mathscr{R}\hat{\alpha}. \tag{4.32}$$

Substituting (Eq. 4.30) into (Eq. 4.20) leads to the equation of motion on the collective mode

$$\frac{d\hat{\alpha}_\zeta}{dt} = -i v_\zeta \hat{\alpha}_\zeta - \hat{\tau}_\zeta, \tag{4.33}$$

where the torque on ζ mode is

$$\hat{\tau}_\zeta = \phi_\zeta^\dagger \hat{\mathscr{T}}. \tag{4.34}$$

4.3.2. Photon scattering spectrum

The coupled set of magnons leads to collective excitations that affect the transmission and reflection of input photons with fixed frequency ω_{in}. The ensemble average $\langle \cdots \rangle$ of

input mode λ is

$$\left\langle \hat{p}_{k,\text{in}}^{\lambda} \right\rangle = A_{\lambda}\delta(k - k_{\lambda}), \tag{4.35}$$

where A_{λ} is the amplitudes of the incoming microwave field and k_{λ} is the positive wave vector satisfying $\Omega_{k_{\lambda}}^{\lambda} = \omega_{\text{in}}$ and we assume that k_{λ} is unique. The average of torque acting on the mode ζ deduced from its definition (Eq. 4.34 and 4.21) is

$$\left\langle \hat{\tau}_{\zeta} \right\rangle = i e^{-i\omega_{\text{in}}t} \sum_{\lambda} A_{\lambda}\mathscr{A}_{\zeta+}^{\lambda}. \tag{4.36}$$

The absorption coefficients for λ band

$$\mathscr{A}_{\zeta\pm}^{\lambda} \equiv \phi_{\zeta}^{\dagger}\mathscr{G}_{\pm k_{\lambda}}^{\lambda} \quad \rightarrow \quad \mathscr{A}^{\lambda} = \mathscr{L}^{\dagger}\mathscr{G}^{\lambda} \tag{4.37}$$

are a linear combination of g_{j}^{λ} with weights given by the left eigenvector. We argue in section 4.5 that as the number of magnetic N goes large, magnons may be localized to only a few magnets, such that a local coupling constant can dominate the global absorption. The average amplitude of mode ζ follows from Eq. (4.33). In the steady state

$$\left\langle \hat{\alpha}_{\zeta}(t) \right\rangle = e^{-i\omega_{\text{in}}t} \sum_{\lambda} A_{\lambda}\frac{\mathscr{A}_{\zeta+}^{\lambda}}{\omega_{\text{in}} - \nu_{\zeta}}. \tag{4.38}$$

Mode ζ is resonantly excited when $\omega_{\text{in}} = \text{Re}\,\nu_{\zeta}$ with spectral broadening $\text{Im}\nu_{\zeta}$.

Similarly the emission coefficients for λ band defined as

$$\mathscr{E}_{\zeta\pm}^{\lambda} \equiv \mathscr{G}_{\pm k_{\lambda}}^{\lambda\dagger}\psi_{\zeta} \quad \rightarrow \quad \mathscr{E}^{\lambda} = \mathscr{G}^{\lambda\dagger}\mathscr{R} \tag{4.39}$$

are linear combination of couplings $\bar{g}_{j}^{\lambda}$ weighted by the right eigenvector. When the latter is localized, emission is governed by a few local magnetizations and their couplings. It is easy to understand the relation $\mathscr{G}^{\lambda\dagger}\hat{\mathscr{B}} = \mathscr{E}^{\lambda}\hat{\alpha}$ holds, and the averaged photon output according to Eq. 4.14 can be rephrased into

$$\left\langle \hat{p}_{k,\text{out}}^{\lambda} \right\rangle = \left\langle \hat{p}_{k,\text{in}}^{\lambda} \right\rangle - i \sum_{\zeta} \mathscr{E}_{\zeta\pm}^{\lambda} \int \hat{\alpha}_{\zeta}(\tau)e^{i\Omega_{k}^{\lambda}\tau}\,d\tau, \tag{4.40}$$

with $+$ $(-)$ sign for $k > 0$ $(k < 0)$. Inserting the magnon mediated absorption $\langle \hat{\alpha}\rangle$ from Eq. 4.38, one can present the overall output as the form of photon transmission and reflection

$$\left\langle \hat{p}_{k,\text{out}}^{\lambda} \right\rangle = \sum_{\lambda'} \left[S_{21}^{\lambda\lambda'}\delta(k - k_{\lambda}) + S_{22}^{\lambda\lambda'}\delta(k + k_{\lambda}) \right] A_{\lambda'}, \tag{4.41}$$

with the transmission amplitude

$$S_{21}^{\lambda\lambda'}(\omega_{\text{in}}) = \delta_{\lambda\lambda'} - \frac{i}{\nu^{\lambda}(k_{\lambda})} \sum_{\zeta=1}^{N} \frac{\mathscr{E}_{\zeta+}^{\lambda}\mathscr{A}_{\zeta+}^{\lambda'}}{\omega_{\text{in}} - \nu_{\zeta}}, \tag{4.42}$$

and the reflection amplitude

$$S_{11}^{\lambda\lambda'}(\omega_{\text{in}}) = -\frac{i}{\nu^{\lambda}(k_{\lambda})} \sum_{\zeta=1}^{N} \frac{\mathscr{E}_{\zeta-}^{\lambda} \mathscr{A}_{\zeta+}^{\lambda'}}{\omega_{\text{in}} - \nu_{\zeta}}. \tag{4.43}$$

S_{12} and S_{22} can be found respectively from S_{11} and S_{21} by the substitution $\mathscr{A}_{\zeta+}^{\lambda'} \to \mathscr{A}_{\zeta-}^{\lambda'}$. The (inter-band) scattering amplitudes resonate at N eigen frequencies of the collective magnetic modes. We point out the photon transmission spectra can also calculated from the scattering theory leading to exactly the same results. Check the appendix 4.7 for more details.

4.4. Rectangular waveguide

Here as an example, we discuss the coupling matrix Σ for a rectangular waveguide with cross-section goes from $(0,0)$ to $(a \geqslant b, b)$. We use mode index $\lambda = \{n, m, \text{TE/TM}\}$, in which integers $n, m \geqslant 0$ are the number of nodes of magnetic (or electric) field in the x- and y-directions, and TE or TM denotes the polarization. In rectangular waveguide the photon dispersion of equation 4.7 has the property $\gamma_x = \pi n/a$, $\gamma_y = \pi m/b$ (Eq. 1.65), and it does not depend on polarization. For simplicity it is also assumed the magnetic spheres are all identical.

The magnetic field of the TM modes are

$$\mathscr{H}_x^{\lambda} = \sqrt{\frac{2\hbar\Omega_k^{\lambda}}{\mu_0 ab}} \frac{\gamma_y}{\gamma} \sin(\gamma_x x) \cos(\gamma_y y),$$

$$\mathscr{H}_y^{\lambda} = -\sqrt{\frac{2\hbar\Omega_k^{\lambda}}{\mu_0 ab}} \frac{\gamma_x}{\gamma} \cos(\gamma_x x) \sin(\gamma_y y), \tag{4.44}$$

with both $n, m > 0$, and of the TE modes read

$$\mathscr{H}_z^{\lambda} = -i\sqrt{\frac{2\eta\hbar}{ab\epsilon_0 \Omega_k^{\lambda}}} \frac{\gamma}{\mu_0} \frac{|k|}{k} \cos(\gamma_x x) \cos(\gamma_y y),$$

$$\mathscr{H}_x^{\lambda} = \sqrt{\frac{2\eta\hbar}{ab\epsilon_0 \Omega_k^{\lambda}}} \frac{|k|}{\mu_0} \frac{\gamma_x}{\gamma} \sin\gamma_x x) \cos(\gamma_y y), \tag{4.45}$$

$$\mathscr{H}_y = \sqrt{\frac{2\eta\hbar}{ab\epsilon_0 \Omega_k^{\lambda}}} \frac{|k|}{\mu_0} \frac{\gamma_y}{\gamma} \cos(\gamma_x x) \sin(\gamma_y y),$$

in which the parameter $\eta = 2 - \delta_{n,0} - \delta_{m,0}$ and at least one of the indices $n, m > 0$. According to general expression of coupling constant in Eq. 4.11 we have

$$g_j^{\lambda}\big|_{\text{TM}} = ie^{ikz_j} \sqrt{\frac{\gamma\mu_0 M_s V_s \Omega_k^{\lambda}}{ab}} \frac{\gamma_y}{\gamma} \sin(\gamma_x x_j) \cos(\gamma_y y_j)$$

$$\equiv ie^{ikz_j} \tilde{g}_j^{\lambda}(k)\big|_{\text{TM}}, \tag{4.46}$$

and

$$g_j^\lambda\big|_{\mathrm{TE}} = ie^{ikz_j}\sqrt{\frac{2\eta\gamma M_s V_s}{ab\epsilon_0\Omega_k^\lambda}}\frac{|k|}{k}\frac{\gamma_x}{\gamma}\cos(\gamma_y y_j)\left[k\sin(\gamma_x x_j)+\frac{\gamma^2}{\gamma_x}\cos(\gamma_x x_j)\right]$$
$$\equiv ie^{ikz_j}\tilde{g}_j^\lambda(k)\big|_{\mathrm{TE}}. \tag{4.47}$$

For the TE modes, the magnon-photon coupling depends on the direction of propagation. The chirality $\tilde{g}_j^\lambda(k)\big|_{\mathrm{TE}} \neq \tilde{g}_j^\lambda(-k)\big|_{\mathrm{TE}}$ is caused by a magnetic field that is not linearly polarized. For example in the $\{1,0,\mathrm{TE}\}$ mode, the two magnets j and l located at $z_j > z_l$ and the j-th magnet sits on a position x_j satisfying

$$\cot\left(\frac{\pi x_j}{a}\right) = -\sqrt{\frac{a^2\omega_l^2}{\pi^2 c^2}-1}, \tag{4.48}$$

then the photon mediated magnon-magnon coupling is fully chiral, i.e. $\Sigma_{jl}=0$ according to Eq. 4.27. So the l-th magnet does not affect the j-th meaning the coupling is nonreciprocal, one magnet feels the dynamics of another but not the other way around.

When tuning the magnon frequency to below the bottom of all λ-bands except for the lowest TE_{10} mode (the TE_{00} mode does not exist), i.e.

$$\frac{\pi}{a} < \frac{\omega_l}{c} < \left\{\frac{\pi}{b},\frac{2\pi}{a}\right\}, \tag{4.49}$$

we can freely tune the chirality. Fig. 4.2 shows a snapshot of the magnetic field for the lowest TE_{10} mode propagating along the $-z$-direction. For the modes along the z-direction, the local ellipticity is reversed. Solving Eq. (4.48) with $\omega_l = \sqrt{5}\,c\pi/a$, magnon-photon coupling is fully chiral for magnets sitting on the green and red dotted line. The chirality vanishes on the center (black dotted) line and is partially chiral elsewhere. Spectral overlap with TM-photons at higher frequencies would reduce the chirality.

For a single magnet with (Kittel) frequency ω_m, its magnon lifetime broadening is $\delta\omega = 2(\alpha_G+\alpha_r)\omega$, where α_G is the Gilbert damping parameter and

$$\alpha_r = \frac{-\mathrm{Im}\Sigma}{\omega_m} = \sum_\lambda \frac{\left|g^\lambda\left(k^\lambda\right)\right|^2+\left|g^\lambda\left(-k^\lambda\right)\right|^2}{2c^2 k^\lambda}, \tag{4.50}$$

To the lowest TE_{10} mode of a rectangular waveguide the associated radiative damping do not depend on the y-coordinate. Results are plotted in Fig. 4.3 for two frequencies of $\omega_m/c = (2/\sqrt{3})\pi/a$ and $\omega_m/c = \sqrt{3}\pi/a$ with parameters $a = 1.6$ cm, $b = 0.6$ cm, magnetic sphere of radius $r_s = 0.6$ mm and intrinsic Gilbert damping $\alpha_G = 5\times 10^{-5}$ [21]. α_r depends strongly on x, but weaker when close to the special position of chiral coupling, i.e., $x = a/3$ and $2a/3$ at $\omega_m/c = (2/\sqrt{3})\pi/a$.

The broadening of the ferromagnetic resonance is not so sensitive to g's chirality, but the transmission is. In the $\lambda = \{1,0,\mathrm{TE}\}$ mode the scattering matrix in Eqs. (4.42) and (4.43) reduces to

$$S_{21}(\omega_{\mathrm{in}}) = \frac{\omega_{\mathrm{in}}-\omega_m+i\alpha_G\omega_m+i(\Sigma_L-\Sigma_R)/2}{\omega_{\mathrm{in}}-\omega_m+i\alpha_G\omega_m+i(\Sigma_L+\Sigma_R)/2}, \tag{4.51}$$

4
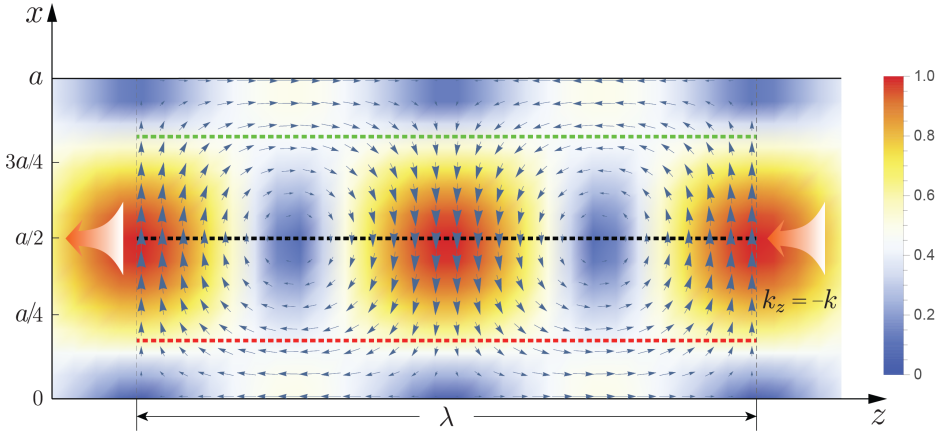
Figure 4.2: Snapshot of the spatial distribution of the AC magnetic field of the lowest TE_{10} mode in a rectangular wave guide propagating along the $-z$-direction. The arrows indicate the direction and modulus of the field. The latter is also indicated by the color shading, from zero (dark blue) to maximum value (dark red). The vector field of modes along the z-direction (not shown) is reversed. The green and red (black) dotted lines indicate the locations at which the magnon-photon coupling is chiral (non-chiral) for magnon frequency tuned to $\omega_l = \sqrt{5}\,c\pi/a$. On the red (green) line, the magnon mode only couples to photons with positive (negative) linear momentum.
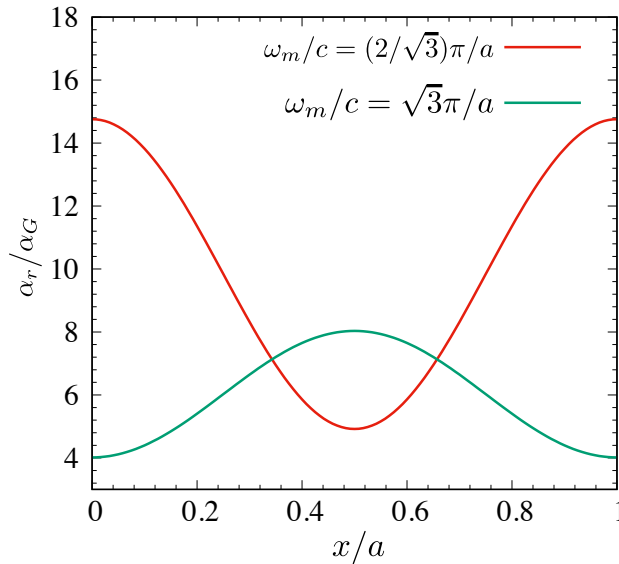
Figure 4.3: Position-dependent radiative damping α_r scaled by the intrinsic Gilbert damping α_G of a YIG sphere by the TE_{10} mode of a rectangular waveguide for two magnetic frequencies ω_m. The parameters are specified in the $a = 1.6$cm, $b = 0.6$cm, and magnet sphere of radius $r_s = 0.6$mm.

where the magnet's directional self-coupling magnitude is

$$\Sigma_R = \left.\frac{|g(k)|^2}{v(k)}\right|_{\text{TE}_{10}}, \qquad \Sigma_L = \left.\frac{|g(-k)|^2}{v(k)}\right|_{\text{TE}_{10}}. \tag{4.52}$$

When $\Sigma_L = \Sigma_R$, the transmission amplitude drops at the resonance $\omega_{\text{in}} = \omega_m$ to a small value $\sim \alpha_G \omega_m / \Sigma_R$. However, for full chirality with $\Sigma_R = 0$, the magnet does not absorb photons travelling towards the right and the waveguide is transparent. When $\Sigma_L = 0$, on the other hand the transmission probability is still unity, but the phase is shifted by π.

4.5. Magnets chain

The imbalance of the magnon distribution is enhanced when more magnets are added to the waveguide. Let us consider a chain of N identical magnets located on a line ($\boldsymbol{\rho}_{\forall i} = \boldsymbol{\rho}$) at equal distance $z_{j+1} - z_j = d \, (0 < j < N)$. This scheme is realized already (but in a closed cavity) for $N = 7$ according to the paper [19]. We study the eigenvectors and eigenvalues of the non-Hermitian matrix

$$\tilde{H}_{\text{eff}} = \left(\omega_m - i\alpha_G\omega_m - i\frac{\Sigma_R + \Sigma_L}{2}\right)\mathscr{I}_{N\times N}$$

$$+ \begin{pmatrix} 0 & -i\Sigma_L e^{ikd} & -i\Sigma_L e^{2ikd} & \dots & -i\Sigma L e^{(N-1)ikd} \\ -i\Sigma_R e^{ikd} & 0 & -i\Sigma_L e^{ikd} & \dots & -i\Sigma_L e^{(N-2)ikd} \\ -i\Sigma_R e^{2ikd} & -i\Sigma_R e^{ikd} & 0 & \dots & -i\Sigma_L e^{(N-3)kd} \\ \vdots & \vdots & \vdots & \ddots & \vdots \\ -i\Sigma_R e^{i(N-1)kd} & -i\Sigma_R e^{i(N-2)kd} & -i\Sigma_R e^{i(N-3)kd} & \dots & 0 \end{pmatrix}, \tag{4.53}$$

where we dropped the TE_{10} mode index λ and

$$k = \sqrt{\frac{\omega_m^2}{c^2} - \left(\frac{\pi}{a}\right)^2}. \tag{4.54}$$

The photons emitted by magnet j to the right are, in our perturbative and adiabatic approach seen, equivalently and instantaneously by all magnets on the right but with a phase factor $e^{ik|z_j - z_l|}$, and analogously for the magnets to the left.

The photon-mediated interaction generates a band structure with generalized Bloch states labelled $\zeta \in \{1, \dots, N\}$ with right eigenvectors $\{\psi_\zeta\}$ and corresponding eigenvalues $\{v_\zeta\}$,

$$(v_\zeta - \tilde{H}_{\text{eff}})\psi_\zeta = 0. \tag{4.55}$$

The real part of v_ζ is the resonance frequency of the ζ-mode and the imaginary part its lifetime. The eigenvectors of $\tilde{H}_{\text{eff}}^\dagger$, ϕ_ζ with eigenvalue v_ζ^* are related to ψ_ζ by a parity-time reversal operation when the spectrum is not degenerate, which is the case for the

simple chain considered here. Let $\mathcal{T}$ be the complex conjugation and

$$\mathcal{P} = \begin{pmatrix} 0 & 0 & \dots & 0 & 1 \\ 0 & 0 & \dots & 1 & 0 \\ \vdots & \vdots & \ddots & \vdots & \vdots \\ 0 & 1 & \dots & 0 & 0 \\ 1 & 0 & \dots & 0 & 0 \end{pmatrix} \tag{4.56}$$

exchanges the magnets $1 \leftrightarrow N$, $2 \leftrightarrow N-1$ and so on, akin to the inversion operation. However, $\mathcal{P}$ does not act on the waveguide and is therefore not a parity operator of the whole system. Clearly, $\mathcal{P}^2 = \mathcal{T}^2 = 1$. $\mathcal{P}$ interchanges $\Sigma_{L \leftrightarrow R}$ in Eq. (4.53), which is equivalent to the transpose operation, i.e. $\tilde{H}_{\text{eff}}^T = \mathcal{P}\tilde{H}_{\text{eff}}\mathcal{P}$, while $\tilde{H}_{\text{eff}}^{\dagger} = \mathcal{P}\mathcal{T}\tilde{H}_{\text{eff}}\mathcal{T}\mathcal{P}$ and

$$\tilde{H}_{\text{eff}}^{\dagger}\mathcal{P}\mathcal{T}\psi_\zeta = v_\zeta^* \mathcal{P}\mathcal{T}\psi_\zeta, \tag{4.57}$$

implying that $\phi_\zeta = \mathcal{P}\mathcal{T}\psi_\zeta$. We chose a normalization

$$\psi_\zeta^T \mathcal{P}\psi_\zeta = 1 \tag{4.58}$$

such that $\phi_\zeta^{\dagger}\psi_\zeta = 1$ and it is then sufficient to describe the dynamics in terms of only the right eigenvectors ψ_ζ.

The magnets interaction with the photons (again suppressing indices) are coherently tuned by the phase vector,

$$\mathcal{G} = -i\sqrt{\Sigma_R v}\left(1, e^{ikd}, \dots, e^{i(N-1)kd}\right)^T. \tag{4.59}$$

The emission amplitude $\mathcal{E}_\zeta = \mathcal{G}^{\dagger}\psi_\zeta = i\sqrt{\Sigma_R v}\tilde{\psi}_\zeta(k)$, where we defined the discrete Fourier transform

$$\tilde{\psi}_\zeta(k) = \left(1, e^{-ikd}, \dots, e^{-i(N-1)kd}\right)^T \psi_\zeta. \tag{4.60}$$

The absorption amplitude $\mathcal{A}_\zeta = \phi_\zeta^{\dagger}\mathcal{G}$ is related to the emission by

$$\mathcal{A}_\zeta = e^{i(N-1)kd}\mathcal{E}_\zeta. \tag{4.61}$$

The global transmission (Eq. 4.42)

$$S_{21}(\omega_{\text{in}}) = 1 - i\Sigma_R e^{i(N-1)kd}\sum_\zeta \frac{\tilde{\psi}_\zeta^2(k)}{\omega_{\text{in}} - v_\zeta}, \tag{4.62}$$

is governed by the right eigenvectors. The total coherent magnetization of the array

$$\langle \hat{\mathcal{B}}(t) \rangle = A\sqrt{\Sigma_R v}e^{-i\omega_{\text{in}}t}e^{i(N-1)kd}\sum_\zeta \frac{\tilde{\psi}_\zeta(k)}{\omega_{\text{in}} - v_\zeta}\psi_\zeta \tag{4.63}$$

is proportional to the amplitude of the incoming photons A (introduced in Sec. 4.3.2). Magnons can be flexibly excited and detected by local antennas that interact only with one magnet [19]. With local input at frequency ω_{in}, $\langle \hat{\mathcal{T}}_l(t) \rangle = i e^{-i\omega_{\text{in}} t} (P_1, P_2, \cdots, P_N)^T$,

$$\langle \hat{\mathcal{B}}(t) \rangle = -i \sum_{\zeta} \frac{(\mathscr{P}\psi_\zeta)^T \langle \hat{\mathcal{T}}_l(t) \rangle}{\omega_{\text{in}} - \tilde{\omega}_m - \gamma_\zeta} \psi_\zeta. \tag{4.64}$$

Note that $(\mathscr{P}\psi_\zeta)^T = (\psi_{\zeta,N}, \psi_{\zeta,N-1}, \cdots, \psi_1)$. When an edge state ζ_* exists, say on the right with large $\psi_{\zeta,N}$, the antenna array with controlled phase difference ϕ, i.e. $\langle \hat{\mathcal{T}}_l(t) \rangle = \exp\left[-i\text{Re}\left(\gamma_{\zeta_*}\right)t\right] i P(1, e^{i\phi}, \cdots, e^{i(N-1)\phi})^T$, can excite a large magnetization at the right edge, where it can be detected by the same local antenna.

It is seen that the excitation of magnetization is determined by the eigenvectors ψ_ζ and their eigenvalues ν_ζ. In the following we present the numerical study for the dissipatively-coupled magnet chain with the special attention for superradiant and subradiant modes, i.e. those with the largest and smallest radiation rates, respectively. As before, $a = 1.6$ cm, $b = 0.6$ cm, $r_s = 0.6$ mm, and $\alpha_G = 5 \times 10^{-5}$ [21]. Typically, $\omega_m/c = \sqrt{3}\pi/a$ corresponding to the photon momentum $k = \sqrt{2}\pi/a$, so only the lowest TE$_{10}$ mode contributes. The magnet chain is parallel to the waveguide and shifted from the chiral line to modulate the chirality $\Sigma_R/\Sigma_L = 1, 0.5, 0.25$, where $\Sigma_L/(2\pi) \in (0, 20)$ MHz. We choose $N = 80$ magnetic spheres and $kd = \pi/5$. So $d = a/(5\sqrt{2}) \approx 0.2$ cm, and the total length of the magnon chain is $Nd \approx 18$ cm. While such a long chain is experimentally impractical, the results are not qualitatively different and emphasize our message.

Fig. 4.4 is a plot of the imaginary (Σ_ζ) and real (E_ζ) parts of $\nu_\zeta - \omega_m$ as a function of mode number ζ, scaled by the local dissipation rate $\Sigma_a = \alpha_G \omega_m + (\Sigma_L + \Sigma_R)/2$. The mode numbers $\zeta = \{1, 2, ..., N\}$ are ordered by magnitudes of Σ_ζ. When $\Sigma_R = \Sigma_L$ (non-chiral case) and $\zeta \approx 80$ ($\zeta \lesssim 10$), the decay rates are larger (smaller) than the local Σ_a, indicating superradiance (subradiance). The decay rates of the most-superradiant states $\sim \Sigma_a N/4$ can simply be enhanced by increasing the number of magnets. The decay of the most-subradiant states $\sim \Sigma_a \zeta^2/N^3$ [26–30] are found at the lower band edge. The value of the magnon energy shifts E_ζ in the inset of Fig. 4.4 are enhanced to a peak around the boundary between sub- and superradiance ($\Sigma_\zeta \approx \Sigma_a$). E_ζ and Σ_ζ have not simple functional relationship, which is reflected by the oscillations (peaks) that look erratic for small mode numbers. The energy shift of the most-subradiant states is very small, but it can be as large as $\sim 10\Sigma_a$ for the superradiant ones, roughly proportional to the number of magnets. The largest energy shift $2\pi \times 100$ MHz is still small compared to ω_m, which justifies the on-shell approximation for Σ_L and Σ_R. E_ζ oscillates with ζ between positive and negative values. A chiral coupling with $\Sigma_R/\Sigma_L = 0.5$ and 0.25 does not strongly change the above features, such the decay rates of the most-subradiant states $\sim \Sigma_a \zeta^2/N^3$.

The intensity distributions $|\psi_{\zeta,j}|^2$ of modes $\zeta = 1, 2, 80$ over the chain $j = \{1, 2, \cdots, N\}$ are shown in Fig. 4.5. When $\Sigma_R = \Sigma_L$ for the non-chiral case, the most-superradiant state is enhanced at both edges of the magnon chain (the red solid curve). The most-subradiant states are standing waves $\sim |\sin(\zeta\pi j/N)|$ delocalized over the whole chain, but have small amplitudes at the edges (see the inset of Fig. 4.5). Partially chiral coupling does not affect the amplitude distributions of the most-subradiant states. The symmetric distribution of the most-superradiant states relative to the center of the chain $\Sigma_R = \Sigma_L$
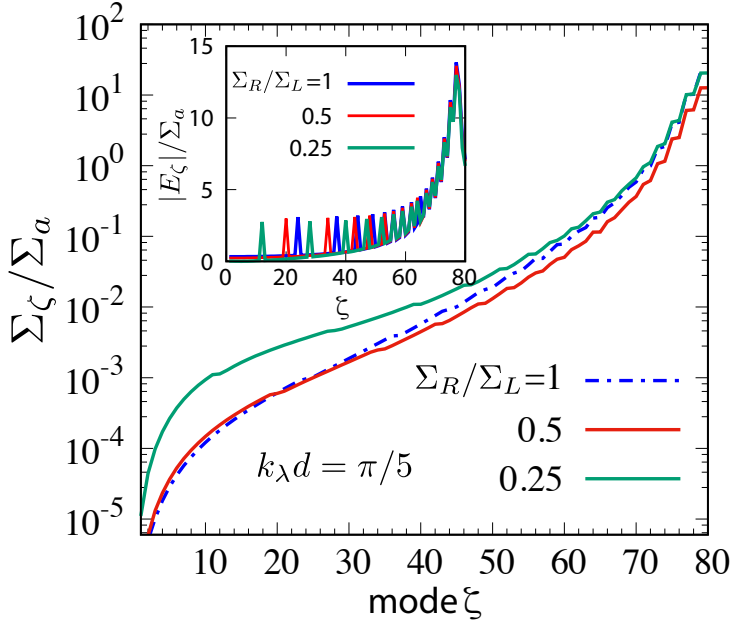
Figure 4.4: Imaginary (Σ_ζ) and real (inset, E_ζ) parts of the eigenvalues ($v_\zeta - \omega_m$) of the non-Hermitian Hamiltonian [Eq. (4.53)], scaled by the individual damping rate Σ_a. $k_\lambda d = \pi/5$ and $N = 80$. $\Sigma_R/\Sigma_L = 1$, 0.5 and 0.25, respectively. E_ζ oscillates as a function of ζ and Σ_ζ in anon-systematic manner.
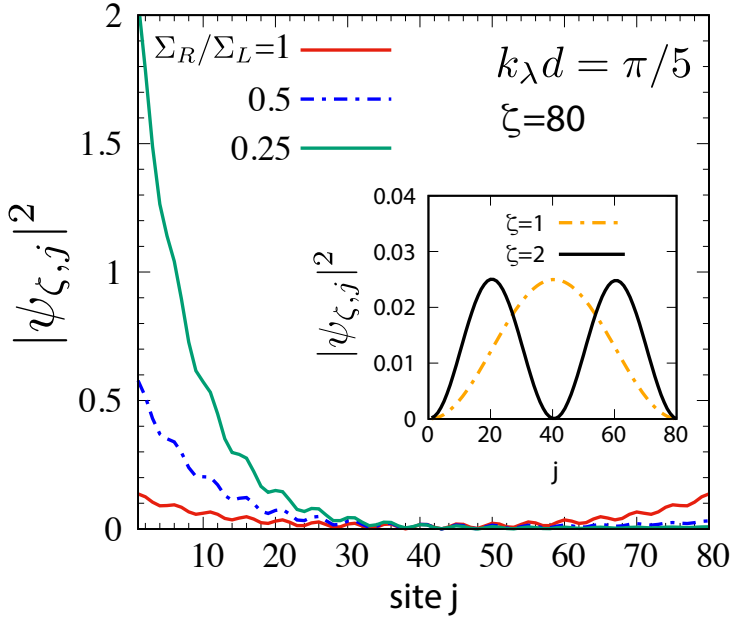
Figure 4.5: Intensity distributions of magnons $\left|\psi_{\zeta,j}\right|^2$ in magnetic spheres labeled by j for the most superradiant and subradiant (inset) states for chiralities $\Sigma_R/\Sigma_L = 1$, 0.5, and 0.25, respectively.

becomes increasingly skewed, i.e., the dynamics is enhanced at one edge only. Particularly, when $\Sigma_R < \Sigma_L$ ($\Sigma_R > \Sigma_L$), the edge state is localized at the left (right) side. When the radiation to the left is stronger than to the right, the magnets on the left side experience more radiation. On the other hand, the magnets in the middle of the chain are part of a standing wave with destructive interference in the average. A larger chirality Σ_R/Σ_L consequently mainly affects the edge states.

4.6. Discussion and Conclusion

In conclusion, we find and report the consequences of chiral and dissipative coupling of small magnets to guided microwaves. We predict a rich variety of physical phenomena, such as directional photon emission and magnon imbalanced pumping and super(sub)radiance of collective magnon modes. Polarization-momentum locking of the electromagnetic field inside a rectangular waveguide and conservation of angular momentum are the physical mechanisms behind chiral magnon-photons interaction. Chirality can be tuned via the positions of the magnetic spheres inside the waveguide and applied static magnetic fields. We develop the theory starting with a single magnet and demonstrate strong radiative damping. Loading the waveguide with two or more magnets causes nonreciprocal tunable coupling between different magnetic spheres. We predict chirality-dependent large magnon amplitudes at the edges of long chains with superradiance. We also reveal subradiant eigenstates, which are standing waves with small amplitude at the edges, that depend only weakly on chirality and therefore scale as different systems without chirality.

The magnetic chain in a waveguide is also a new platform to study non-Hermitian physics [41, 42]. The rich magnon-photon dynamics suggests several lines of future research. Tunable waveguides allow manipulation of the local density of photon states and linewidth for each collective mode [21], while arrangements of the magnetic spheres into rings, lattices or random geometry promise a new "magnon chemistry". Some non-Hermitian Hamiltonians may result in topological phases, a hot topic in condensed matter physics [32, 43]. The non-Bloch-wave behavior of eigenstates of a chiral magnon-photon system can cause a non-Hermitian skin effect and a non-Bloch bulk-boundary correspondence. The non-linear dynamics of a chirally vs. non-chirally coupled magnon-photon system can be accessed by the photon statistics of the waveguide to specify the entanglement of sub- and super-radiant states [30].

4.7. Appendix: Derivation of the S_{21} and S_{11} from scattering theory

For the coupled waveguide and local resonator system as in this research, the Hamiltonian can be divided into two parts, namely the isolated Hamiltonian for each subsystems H_{iso} and their coupling V [44]. In our case, $H_{\text{iso}} = H_{\text{EM}} + H_{\text{M}}$ as in Eqs. 4.6, 4.9 and $V = H_{\text{int}}$ as in Eq. 4.10. Assume the waveguide mode $|k_{\text{in}}\rangle$ as the input state and the total state $|\psi_{\text{out}}\rangle$ as the final output, in general we have the relation [45]

$$|\psi_{\text{out}}\rangle = |k_{\text{in}}\rangle + \frac{1}{\Omega_{k_{\text{in}}} - H_0 + i0^+} V |\psi_{\text{out}}\rangle \equiv T |k_{\text{in}}\rangle. \qquad (4.65)$$

If we define the matrix $T_{ji} = \langle \psi_j | T | \psi_i \rangle$ meaning the transfer from general state i into state j, then the scattering amplitude from input $|k\rangle$ into the output $|k'\rangle$ is

$$T_{k'k} = \delta_{k'k} + \frac{1}{\Omega_k - \Omega_{k'} + i0^+} \langle k' | V T | k \rangle. \tag{4.66}$$

In our special case, as an illustration we assume only one sphere exist in the waveguide and ignore the band index λ, then

$$T_{k'k} = \delta_{k'k} + \frac{1}{\Omega_k - \Omega_{k'} + i0^+} \bar{g}_{k'} T_{mk}. \tag{4.67}$$

Here T_{mk} stands for the transfer from photon state $|k\rangle$ into the magnon state $|m\rangle$ and $\bar{g}_{k'}$ meaning the re-emission of photon $|k'\rangle$ under the cost of radioactive damping of magnon. Thus the amplitude T_{mk} in turn can be expressed as

$$T_{mk} = \frac{1}{\Omega_k - \omega_m + i0^+} \sum_q g_q T_{qk}, \tag{4.68}$$

and the photon-photon scattering can be expressed into the recursive form

$$\begin{aligned}
T_{k'k} = \delta_{k'k} &+ \frac{1}{\Omega_k - \Omega_{k'} + i0^+} \bar{g}'_k \frac{1}{\Omega_k - \omega_m + i0^+} g_k \\
&+ \frac{1}{\Omega_k - \Omega_{k'} + i0^+} \bar{g}_{k'} \frac{1}{\Omega_k - \omega_m + i0^+} \sum_q g_q \frac{1}{\Omega_k - \Omega_l + i0^+} \bar{g}_q T_{mk}.
\end{aligned} \tag{4.69}$$

It is easy to reach the enclosed formula

$$T_{k'k} = \delta_{k'k} + \frac{1}{\Omega_k - \Omega_{k'} + i0^+} \bar{g}_{k'} G(\Omega_k) g_k, \tag{4.70}$$

with $G(\omega) = [\omega - \omega_m - \Sigma(\omega)]^{-1}$ is the magnon's Green function and Σ is the magnon's self-energy, which is exactly the same as the one derived from the equation of motion (Eq. 4.24)

$$\Sigma(\omega) = \sum_q \frac{|g_q|^2}{\omega - \Omega_q + i0^+}. \tag{4.71}$$

Next we want to calculate the scattering matrix element S_{21} and S_{11} describing the transmission and reflection respectively. Define the transmitted $\psi_t(\mathbf{r})$ and reflected $\psi_r(\mathbf{r})$ photon wave at position far away from the magnetic sphere which located at $z = 0$,

$$\begin{aligned}
\psi_t &= \sum_{k'>0} \langle z \to +\infty | k' \rangle T_{k'k} = \langle z \to +\infty | k \rangle + \sum_{k'>0} \frac{\langle z \to +\infty | k' \rangle}{\Omega_k - \Omega_{k'} + i0^+} \bar{g}_{k'} G(\Omega_k) g_k, \\
\psi_r &= \sum_{k'<0} \frac{\langle z \to -\infty | k' \rangle}{\Omega_k - \Omega_{k'} + i0^+} \bar{g}_{k'} G(\Omega_k) g_k.
\end{aligned} \tag{4.72}$$

Using the residual integral one can obtain the scattering matrix with the one magnetic sphere inside waveguide

$$S_{21}(\Omega_k) = 1 - i\frac{1}{v_k}\frac{|g_k|^2}{\Omega_k - \omega_m - \Sigma(\Omega_k)},$$
$$S_{11}(\Omega_k) = -i\frac{1}{v_k}\frac{\bar{g}_{-k}g_k}{\Omega_k - \omega_m - \Sigma(\Omega_k)},$$
(4.73)

which is the same as in Eq. 4.42 and 4.43. With the single magnet self-energy

$$\Sigma(\Omega_k) = -i\frac{1}{2v_k}\left(|g_k|^2 + |g_{-k}|^2\right),$$
(4.74)

it is proved that $|S_{21}|^2 + |S_{11}|^2 = 1$.

Finally the general transfer of various states mediated by the multi-resonators absorption and emission is [46]

$$T_{k'k} = \delta_{k'k} + \frac{1}{\Omega_k - \Omega_{k'} + i0^+}\sum_{m,n} V_{k',m} G_{m,n}(\Omega_k) V_{n,k},$$
(4.75)

$$T_{m,k} = \sum_m G_{m,n}(\Omega_k) V_{n,k},$$
(4.76)

with $G_{m,n}$ is the Green function from resonator n to m describing the remote coupling between them. It can be derived that

$$G(\omega) = \frac{1}{\omega - H + i0^+} \quad \rightarrow \quad G_{m,n}^{-1} = (\omega - \omega_n)\delta_{m,n} - \Sigma_{m,n},$$
(4.77)

with the effective inter-magnet self-energy $\Sigma_{m,n}$ given by Eq. 4.24.

References

[1] T. Yu, X. Zhang, S. Sharma, Y. M. Blanter, and G. E. W. Bauer, *Chiral coupling of magnons in waveguides,* Phys. Rev. B **101**, 094414 (2020).

[2] B. Lenk, H. Ulrichs, F. Garbs, and M. Münzenberg, *The building blocks of magnonics,* Physics Reports **507**, 107 (2011).

[3] A. V. Chumak, V. I. Vasyuchka, A. A. Serga, and et al., *Magnon spintronics,* Nature Phys. **11**, 453.

[4] D. Grundler, *Nanomagnonics around the corner,* Nature Nanotech **11**, 407 (2016).

[5] V. Demidov, S. Urazhdin, G. de Loubens, O. Klein, V. Cros, A. Anane, and S. Demokritov, *Magnetization oscillations and waves driven by pure spin currents,* Physics Reports **673**, 1 (2017).

[6] H. Chang, P. Li, W. Zhang, T. Liu, A. Hoffmann, L. Deng, and M. Wu, *Nanometer-thick yttrium iron garnet films with extremely low damping,* IEEE Magnetics Letters **5**, 1 (2014).

[7] Y. Tabuchi, S. Ishino, A. Noguchi, T. Ishikawa, R. Yamazaki, K. Usami, and Y. Naka-mura, *Coherent coupling between a ferromagnetic magnon and a superconducting qubit,* Science **349**, 405 (2015).

[8] Y. Tserkovnyak, A. Brataas, and G. E. W. Bauer, *Enhanced gilbert damping in thin ferromagnetic films,* Phys. Rev. Lett. **88**, 117601 (2002).

[9] Y. Tserkovnyak, A. Brataas, G. E. W. Bauer, and B. I. Halperin, *Nonlocal magnetiza-tion dynamics in ferromagnetic heterostructures,* Rev. Mod. Phys. **77**, 1375 (2005).

[10] T. Yu, C. Liu, H. Yu, Y. M. Blanter, and G. E. W. Bauer, *Chiral excitation of spin waves in ferromagnetic films by magnetic nanowire gratings,* Phys. Rev. B **99**, 134424 (2019).

[11] J. Chen, T. Yu, C. Liu, T. Liu, M. Madami, K. Shen, J. Zhang, S. Tu, M. S. Alam, K. Xia, M. Wu, G. Gubbiotti, Y. M. Blanter, G. E. W. Bauer, and H. Yu, *Excitation of uni-directional exchange spin waves by a nanoscale magnetic grating,* Phys. Rev. B **100**, 104427 (2019).

[12] T. Yu, Y. M. Blanter, and G. E. W. Bauer, *Chiral pumping of spin waves,* Phys. Rev. Lett. **123**, 247202 (2019).

[13] Y. Kubo, F. R. Ong, P. Bertet, D. Vion, V. Jacques, D. Zheng, A. Dréau, J.-F. Roch, A. Auf-feves, F. Jelezko, J. Wrachtrup, M. F. Barthe, P. Bergonzo, and D. Esteve, *Strong cou-pling of a spin ensemble to a superconducting resonator,* Phys. Rev. Lett. **105**, 140502 (2010).

[14] R. Amsüss, C. Koller, T. Nöbauer, S. Putz, S. Rotter, K. Sandner, S. Schneider, M. Schramböck, G. Steinhauser, H. Ritsch, J. Schmiedmayer, and J. Majer, *Cav-ity qed with magnetically coupled collective spin states,* Phys. Rev. Lett. **107**, 060502 (2011).

[15] D. I. Schuster, A. P. Sears, E. Ginossar, L. DiCarlo, L. Frunzio, J. J. L. Morton, H. Wu, G. A. D. Briggs, B. B. Buckley, D. D. Awschalom, and R. J. Schoelkopf, *High-cooperativity coupling of electron-spin ensembles to superconducting cavities,* Phys. Rev. Lett. **105**, 140501 (2010).

[16] S. Probst, H. Rotzinger, S. Wünsch, P. Jung, M. Jerger, M. Siegel, A. V. Ustinov, and P. A. Bushev, *Anisotropic rare-earth spin ensemble strongly coupled to a supercon-ducting resonator,* Phys. Rev. Lett. **110**, 157001 (2013).

[17] O. O. Soykal and M. E. Flatté, *Strong field interactions between a nanomagnet and a photonic cavity,* Phys. Rev. Lett. **104**, 077202 (2010).

[18] X. Zhang, C.-L. Zou, L. Jiang, and H. X. Tang, *Strongly coupled magnons and cavity microwave photons,* Phys. Rev. Lett. **113**, 156401 (2014).

[19] X. Zhang, C.-L. Zou, N. Zhu, and et al, *Magnon dark modes and gradient memory,* Nat. Commun. **6**, 8914 (2015).

[20] R. W. Sanders, D. Paquette, V. Jaccarino, and S. M. Rezende, *Radiation damping in magnetic resonance. ii. continuous-wave antiferromagnetic-resonance experiments,* Phys. Rev. B **10**, 132 (1974).

[21] B. Yao, T. Yu, Y. S. Gui, and et al, *Coherent control of magnon radiative damping with local photon states,* Commun. Phys. **2**, 161 (2019).

[22] M. A. W. Schoen, J. M. Shaw, H. T. Nembach, M. Weiler, and T. J. Silva, *Radiative damping in waveguide-based ferromagnetic resonance measured via analysis of perpendicular standing spin waves in sputtered permalloy films,* Phys. Rev. B **92**, 184417 (2015).

[23] P. Lodahl, S. Mahmoodian, S. Stobbe, A. Rauschenbeutel, P. Schneeweiss, J. Volz, H. Pichler, and Z. P., *Chiral quantum optics,* Nature **541**, 473 (2017).

[24] C. A. Downing, J. C. L. Carreño, F. P. Laussy, E. del Valle, and A. I. Fernández-Domínguez, *Quasichiral interactions between quantum emitters at the nanoscale,* Phys. Rev. Lett. **122**, 057401 (2019).

[25] M. Harder, Y. Yang, B. M. Yao, C. H. Yu, J. W. Rao, Y. S. Gui, R. L. Stamps, and C.-M. Hu, *Level attraction due to dissipative magnon-photon coupling,* Phys. Rev. Lett. **121**, 137203 (2018).

[26] A. Asenjo-Garcia, M. Moreno-Cardoner, A. Albrecht, H. J. Kimble, and D. E. Chang, *Exponential improvement in photon storage fidelities using subradiance and "selective radiance" in atomic arrays,* Phys. Rev. X **7**, 031024 (2017).

[27] Y.-X. Zhang and K. Mølmer, *Theory of subradiant states of a one-dimensional two-level atom chain,* Phys. Rev. Lett. **122**, 203605 (2019).

[28] M. Moreno-Cardoner, D. Plankensteiner, L. Ostermann, D. E. Chang, and H. Ritsch, *Subradiance-enhanced excitation transfer between dipole-coupled nanorings of quantum emitters,* Phys. Rev. A **100**, 023806 (2019).

[29] P.-O. Guimond, A. Grankin, D. V. Vasilyev, B. Vermersch, and P. Zoller, *Subradiant bell states in distant atomic arrays,* Phys. Rev. Lett. **122**, 093601 (2019).

[30] G. Buonaiuto, R. Jones, B. Olmos, and I. Lesanovsky, *Dynamical creation and detection of entangled many-body states in a chiral atom chain,* New Journal of Physics **21**, 113021 (2019).

[31] M. G. Benedict, A. M. Ermolaev, V. A. Malyshev, I. V. Sokolov, and E. D. Trifonov, *Super-radiance: Multiatomic Coherent Emission (1st ed.)* (CRC Press., 1996).

[32] S. Yao and Z. Wang, *Edge states and topological invariants of non-hermitian systems,* Phys. Rev. Lett. **121**, 086803 (2018).

[33] C. Kittel, *On the theory of ferromagnetic resonance absorption,* Phys. Rev. **73**, 155 (1948).

[34] L. D. Landau and E. M. Lifshitz, *Electrodynamics of Continuous Media* (Butterworth-Heinemann, 1984).

[35] J. D. Jackson, *Classical Electrodynamics, 3rd Edition* (Wiley, 1998).

[36] A. Kamra and W. Belzig, *Super-poissonian shot noise of squeezed-magnon mediated spin transport,* Phys. Rev. Lett. **116**, 146601 (2016).

[37] Y. Cao, P. Yan, H. Huebl, S. T. B. Goennenwein, and G. E. W. Bauer, *Exchange magnon-polaritons in microwave cavities,* Phys. Rev. B **91**, 094423 (2015).

[38] C. W. Gardiner and M. J. Collett, *Input and output in damped quantum systems: Quantum stochastic differential equations and the master equation,* Phys. Rev. A **31**, 3761 (1985).

[39] A. A. Clerk, M. H. Devoret, S. M. Girvin, F. Marquardt, and R. J. Schoelkopf, *Introduction to quantum noise, measurement, and amplification,* Rev. Mod. Phys. **82**, 1155 (2010).

[40] D. Gall, *Electron mean free path in elemental metals,* Journal of Applied Physics **119**, 085101 (2016).

[41] C. M. Bender, D. C. Brody, and H. F. Jones, *Complex extension of quantum mechanics,* Phys. Rev. Lett. **89**, 270401 (2002).

[42] R. El-Ganainy, K. Makris, M. Khajavikhan, and et al, *Non-hermitian physics and pt symmetry,* Nature Phys. **14**, 11 (2018).

[43] Z. Gong, Y. Ashida, K. Kawabata, K. Takasan, S. Higashikawa, and M. Ueda, *Topological phases of non-hermitian systems,* Phys. Rev. X **8**, 031079 (2018).

[44] Y. Xu, Y. Li, R. K. Lee, and A. Yariv, *Scattering-theory analysis of waveguide-resonator coupling,* Phys. Rev. E **62**, 7389 (2000).

[45] J. Sakurai and J. Napolitano, *Modern Quantum Mechanics (2nd ed.)* (Cambridge University Press., 2017).

[46] S. Fan, P. R. Villeneuve, J. D. Joannopoulos, M. J. Khan, C. Manolatou, and H. A. Haus, *Theoretical analysis of channel drop tunneling processes,* Phys. Rev. B **59**, 15882 (1999).

4

5

Enhanced energy transfer in a Dicke quantum battery

If I had an hour to solve a problem and my life depended on the solution,
I would spend the first 55 minutes determining the proper question to ask,
for once I know the proper question,
I could solve the problem in less than five minutes.

Albert Einstein

We theoretically investigate the enhancement of the charging power in a Dicke quantum battery which consists of an array of N two-level systems (TLS) coupled to a single mode of cavity photons. In the limit of small N, we analytically solve the time evolution for the full charging process. The eigenvectors of the driving Hamiltonian are found to be pseudo-Hermite polynomials and the evolution is thus interpreted as harmonic oscillator like behaviour. Then we demonstrate that the average charging power when using a collective protocol is $\sqrt{N}$ times larger than for the parallel charging protocol when transferring the same amount of energy. Unlike previous studies, we point out that such quantum advantage does not originate from entanglement but is due to the coherent cooperative interactions among the TLSs. Our results provide intuitive quantitative insight into the dynamic charging process of a Dicke battery and can be observed under realistic experimental conditions.

5.1. Introduction

Batteries have become ubiquitous in modern technology, supplying power to devices as small as nano-robots and as large as automotive engines. However, the continuing miniaturization technology gradually pushes those traditional batteries into the atomic limit, i.e. the quantum world. This trend, rather than bringing us into an uncontrollable regime, offers the possibility of utilizing quantum properties for investigating and developing more efficient energy manipulations [2–6].

The emerging field of quantum batteries, started by Alicki and Fannes [7], is aimed at searching for adequate protocols based on quantum coherence and entanglement to the efficient charging-discharging energy transfer. In general, a quantum battery is a system possessing discrete energy levels and interacting with external driving and consumption sources in a controllable fashion. The internal energy of a quantum battery is defined as $\text{Tr}[\rho H_B]$, with ρ the density matrix describing the state of the battery and H_B the battery Hamiltonian (see section 5.2). Charging (discharging) of a quantum battery means evolving into a higher (lower) energetic state ρ' by cyclic unitary operations. From the viewpoint that information is a form of energy, research on quantum batteries intrinsically involves using the notions and techniques of quantum information [8]. Questions like whether entanglement plays a role in speeding up the energy transfer and how does entropy (and related concepts) evolve in specific battery systems are under active research. [9–17]

As an answer to these questions, Binder *et al.* suggested that energy can be deposited into an array of N working qubits with speed-up in charging time T such that $T_{\text{global}} = T_{\text{par}}/N$ for the use of a globally entangling charging Hamiltonian compared to a parallel individual protocol [18]. In consequence, the average charging power defined by $\langle P \rangle = \text{Tr}[(\rho' - \rho)H_B]/T$ is N fold stronger for the entangling charging protocol compared to the parallel one. However, such a global entangling operation involves highly non-local interactions, which might be difficult to realize in practice. Le *et al.* therefore designed a practical model consisting of a solid state spin-chain driven under experimentally available resources such as electron spin resonance and exchange interactions [19]. They predict that in the strong coupling regime the time-averaged charging power for an entangling protocol is actually worse than for individual charging. While the instantaneous charging power could be large, the total amount of energy stored in a spin chain is negligibly small. This conflicting scenario leads us to investigate if the enhancement of charging can always be attributed to the shortened passage through the entangled subspace [19].

Another practical setting for global charging is based on the Dicke model [20], which describes an array of two-level systems (TLS) enclosed in a photon cavity whose frequency is on resonance with the Zeeman splitting of those TLSs. A recent paper shows that in the thermodynamic limit (i.e. the number of TLS $N \gg 1$) quantum enhancement of charging power is proportional to $\sqrt{N}$ in the normal phase and N in the superradiant phase [21, 22]. It is argued in Ref. [21] that the cause of such enhancement is the entanglement between TLSs, which is induced by the sharing of photons in the cavity. However, the conclusion from Ref. [23] suggests that there is actually no entanglement generated in the Dicke superradiant phase. Based on this conclusion and the conjecture of Ref. [19] that entanglement may not be the only cause of quantum speed-up, we

investigate in this chapter the question whether for other limits of a Dicke quantum battery there is also a speed-up effect in charging and whether entanglement plays a role in this.

In particular, we analytically prove that in the opposite limit, when the number of TLSs is much smaller than the number of cavity photons ($N/n \ll 1$), there is also an enhancement of charging efficiency. According to experimental practice, we limit the Dicke Hamiltonian to a range where the coupling strength is smaller than the Zeeman splitting of the TLS and thus the rotating wave approximation (RWA) is applied. To the first-order approximation of N/n, the eigenvectors of the driving Hamiltonian are found to be pseudo-Hermite polynomials and the evolution is thus interpreted as harmonic oscillator like behavior. We calculate the time of charging all the TLSs from the ground state to excited state and find $\tau = \frac{\pi}{2g\sqrt{n}}$, independent to the number of TLSs N. Given this universal flipping duration we argue that the power for a collective charging protocol is $\sqrt{N}$ times larger than for an individual charging one. Quite contrary to previous studies [7, 18, 21], there is no entanglement created during such a process. By solving the von Neumann equation, we clearly see that the source of speed-up comes from the coherent but non-entangling cooperative interaction among the spins.

The remaining part of this chapter is organized as follows. In Sec. 5.2 we provide the definitions of fundamental concepts, charging protocols, and specify the Hamiltonian for the system. Next in Sec. 5.3 we diagonalize the driving Hamiltonian and solve the Schrödinger equation. We then derive the boost of the energy transfer efficiency for our Dicke quantum battery. Sec. 5.4 is devoted to investigating the origin of such enhancement and comparing our model with other studies. We provide concluding remarks in Sec. 5.5.

5.2. Model description

The model of a quantum battery, shown in Fig. 5.1, is an array of two level systems enclosed in a photon cavity. Since there is an equivalence between the ground/excited state of two level system to the spin down/up state of Zeeman splitting, we will refer to these TLSs as spins in the following. Without loss of generality, we set the spin down $|\downarrow\rangle$ to be the ground state and initialize the battery system into the state of all spins down $|\psi_0\rangle = |\downarrow,\downarrow,\ldots,\downarrow\rangle$. When applying a magnetic filed B_z the internal Hamiltonian of the battery system reads:

$$H_B = g^*\mu_B B_z S_z \tag{5.1}$$

where $S_z = \sum_{j=1}^{N} \sigma_z^{(j)}$, the index j refers to the jth spin inside the cavity and σ_z denotes the Pauli spin operator in the z-direction. S_z is the total spin operator, counting the Zeeman splitting for all the spins. Working in units of $\hbar = 1$, the battery Hamiltonian (5.1) can be simplified as:

$$H_B = \omega_a S_z \tag{5.2}$$

where the frequency ω_a can be tuned by changing the external magnetic field B_z. The initial energy for such a N-spin battery then corresponds to be $E_0 = \langle\psi_0|H_B|\psi_0\rangle = -\frac{N}{2}\omega_a$ for $S_z = 1/2$, and the energy stored in the battery is given by:

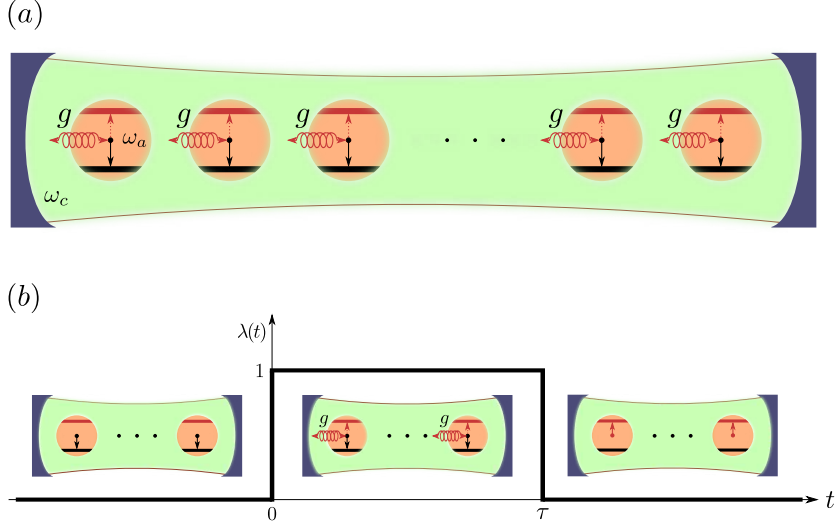$$W(t) = \langle\psi_t|H_B|\psi_t\rangle - \langle\psi_0|H_B|\psi_0\rangle. \tag{5.3}$$

Figure 5.1: (a) Schematic representation of a Dicke quantum battery as an array of identical two level systems with energy splitting $\hbar\omega_a$. The ground state (black bar) and excited state (red bar) are equivalent to the states of spin down and up (see arrows). The batteries are charged inside a single cavity (green background) of photonic mode ω_c and g is the coupling constant among TLSs and cavity photons. (b) Initially the coupling signal λ is set to be 0 and the batteries are prepared in the ground state. The coupling is switched on at time $t = 0^+$ and maintained as constant g for a period of τ. Then we turn off the coupling and the charging process therefore stops. Energy is transferred from cavity photons into the batteries whose final states are expected to be fully charged (all spins up).

In this chapter, we focus on the time required to flip all spins down $\left|\psi_0\right\rangle = \left|\downarrow,\downarrow,\dots,\downarrow\right\rangle$ to all spins up $\left|\psi_\tau\right\rangle = \left|\uparrow,\uparrow,\dots,\uparrow\right\rangle$. So the energy stored in the battery by this process is expected to be:

$$W(\tau) = \left\langle\psi_\tau\right|H_B\left|\psi_\tau\right\rangle - \left\langle\psi_0\right|H_B\left|\psi_0\right\rangle = N\omega_a \tag{5.4}$$

and the average charging power is:

$$P(\tau) = \frac{W(\tau)}{\tau}. \tag{5.5}$$

The cavity, as the charger, is set to stay in a single mode of the quantized electromagnetic field. Its internal Hamiltonian reads $H_c = \omega_c a^\dagger a$, with ω_c the photon frequency and $a^\dagger, a$ the creation and annihilation operators of cavity photons. We assume the cavity has high quality factor and the leakage of photons can be ignored. As the flipping duration is short enough, the relaxation and dephasing effect of TLS can also be safely neglected. Moreover, we assume that by tuning the external magnetic field B_z, the Zeeman splitting of the spins is on resonance with the cavity photons, i.e. $\omega_c = \omega_a$. Originating from magnetic dipole interactions, the coupling between the cavity photons and spins is modeled as the Dicke interaction $H_{\text{int}} = g(a^\dagger + a)(S_+ + S_-)$, where $S_\pm = \sum_{j=1}^{N} \sigma_\pm^{(j)}$ are the (summed) raising and lowering operators and g is the coupling constant. The full Hamiltonian describing the charger-battery system is now given by:

$$H_{\text{Dicke}}(t) = \omega_c a^\dagger a + \omega_a S_z + \lambda(t)g(a^\dagger + a)(S_+ + S_-). \tag{5.6}$$

Here $\lambda(t)$ is a time-dependent coupling signal set to be 1 during the charging period $[0, \tau]$ and 0 otherwise, as illustrated in Fig. 5.1. Before $t = 0$ there is no coupling between photons and spins, and the cavity is assumed to stay in a n-photon Fock state $|n\rangle$. The initial state of total system $|\Psi_0\rangle$ then reads:

$$|\Psi_0\rangle = |\downarrow, \downarrow, \ldots, \downarrow\rangle \otimes |n\rangle \tag{5.7}$$

At $t = 0^+$ the coupling is turned on. Driven by the Dicke Hamiltonian (5.6) energy starts to be transferred from cavity photons to battery spins. The coupling is kept constant during this charging period $t \in [0, \tau]$ and shall be switched off at $t = \tau$. The quantum state of the total system will then be static again with the battery spins expected to be fully flipped up. Similar process of start and pause of swapping has been achieved with high fidelity in recent experiment setup of superconducting quantum circuit with multi qubits inter-connected by the photon cavity [24].

In typical experiment settings, the coupling constant g is much smaller than cavity energy ω_c so that the Dicke interaction can be simplified using the rotating wave approximation. Thus resulting in the Tavis-Cumming Hamiltonian as from Ref. [25]:

$$H = \omega_c a^\dagger a + \omega_c S_z + g(S_+ a + S_- a^\dagger) \tag{5.8}$$

We point out four prominent properties of this charging protocol:

- When the photon frequency is on resonance with Zeeman energy, we have $[H, a^\dagger a + S_z] = 0$, i.e. the "excitation number" is conserved during the evolution. For example if we have 3 spins inside the cavity, the initial state can be denoted as $\left|\frac{3}{2}, -\frac{3}{2}, n\right\rangle$ with $J = \frac{3}{2}$ and $M = -\frac{3}{2}$ standing for the state of three spins down and n the initial photon number. During the evolution this charger-battery system can only evolve into states $\left|\frac{3}{2}, -\frac{1}{2}, n-1\right\rangle$, $\left|\frac{3}{2}, \frac{1}{2}, n-2\right\rangle$, and $\left|\frac{3}{2}, \frac{3}{2}, n-3\right\rangle$, keeping the excitation number $n - \frac{3}{2}$ conserved.

- The coupling term in Eq. (5.8) commutes with the remaining part of Hamiltonian H, meaning that there is no thermodynamic work cost for switching on and off the coupling [13].

- The Tavis-Cummings Hamiltonian is not exactly solvable except for two limiting cases. The first one is when the number of spins N approaches thermodynamic limit. In this situation one can transform the collective spin operators using Holstein-Primakoff transformation which leads to a simplified Hamiltonian of quadratic form [26]. A second case is for the number of spins N much less than the number of photons, $N \ll n$. To the first-order approximation [27], the second case will result in solving a symmetric tridiagonal matrix which can be done analytically.

- The initial Fock state is relatively difficult to prepare in practice. But according to the conclusion of Ref. [13], the same efficiency of energy transfer can be achieved by replacing the Fock state with a coherent state of the same energy.

5.3. Collective Charging of a Dicke Quantum Battery

In this research, we calculate the time of flipping the spins in Schrödinger picture and we analytically solve the matrix representation of the charging Hamiltonian (5.8). Due to the conservation of excitation number, the quantum states of such charger-battery system flipping from $\left|\frac{N}{2}, -\frac{N}{2}, n\right\rangle$ to $\left|\frac{N}{2}, \frac{N}{2}, n-N\right\rangle$ can only evolve within the subspace in which the total spin momentum ($J = N/2$) is preserved. Thus the matrix representation of the Hamiltonian is limited to dimension $N + 1$ instead of 2^N. Taking these states as basis and within the first-order approximation of $N \ll n$, i.e. the strong field of driving photons [28], the charging Hamiltonian is represented as $H = \mathcal{N}_{ex}\mathbb{1} + \tilde{H}$, with $\mathcal{N}_{ex}$ the excitation number and

$$
\tilde{H} = g\sqrt{n}
\begin{pmatrix}
0 & b_1 & & & & & \\
b_1 & 0 & b_2 & & & & \\
& b_2 & 0 & b_3 & & & \\
& & \ddots & \ddots & \ddots & \\
& & & b_{N-1} & 0 & b_N \\
& & & & b_N & 0
\end{pmatrix}
\tag{5.9}
$$

where each element $b_k = \sqrt{N-k+1}\sqrt{k}$ and $k = 1, 2, \ldots, N$. Because the identity matrix commutes with all other operators, the first term of H only adds a common phase factor to the quantum state which does not influence the spin-flip duration. So we can ignore the first term and only include the second part of H (i.e. the symmetric tridiagonal matrix) into the calculation of propagator $U(t) = e^{-i\tilde{H}t}$.

Given the matrix form of $\tilde{H}$ we are now ready to determine analytically the flip duration τ for fully charging the spins:

$$
\begin{pmatrix} 1 \\ 0 \\ \vdots \\ 0 \end{pmatrix} \stackrel{\tau?}{=\!=} e^{-i\tilde{H}\tau} \begin{pmatrix} 0 \\ 0 \\ \vdots \\ 1 \end{pmatrix}.
\tag{5.10}
$$

However, direct substitution of the matrix expression (Eq. 5.9) into the propagator $e^{-i\tilde{H}t}$ results in a cumbersome expression. In practice, we therefore first diagonalize this Hamiltonian such that $\tilde{H} = VDV^\dagger$, with D a diagonal matrix whose elements represent the eigenvalues of $\tilde{H}$, and V a unitary matrix in which each column stands for the corresponding eigenvectors. After that we can write the propagator as $U(t) = Ve^{-iDt}V^\dagger$.

The calculation of eigenvalues and eigenvectors of matrix $\tilde{H}$ (5.9) is straightforward but involves rather technical expressions. Here we therefore only present the final results. The eigenvalues of $\tilde{H}$ are:

$$
D = g\sqrt{n}
\begin{pmatrix}
N & & & & \\
& N-2 & & & \\
& & \ddots & & \\
& & & -N+2 & \\
& & & & -N
\end{pmatrix}.
\tag{5.11}
$$

Disregarding the common factor $g\sqrt{n}$, these eigenvalues form a sequence from N to $-N$ with a consecutive difference of -2. These results coincide with the numerical analysis of the Rabi splitting for Tavis-Cumming Hamiltonian in the large photon limit [29]. The eigenvectors corresponding to eigenvalues $g\sqrt{n}(N-2k)$ ($k=0,1,\ldots,N$) are:

$$V^k = \frac{1}{2^N}\frac{1}{k!\sqrt{\binom{N}{k}}}\begin{pmatrix} x_0^k \\ x_1^k \\ \vdots \\ x_N^k \end{pmatrix},$$ (5.12)

with each of the column entries x_ξ^k ($\xi = 0,1,\ldots,N$) given by:

$$x_\xi^k = \sqrt{\binom{N}{\xi}}P_k(\xi).$$ (5.13)

The characteristic polynomials $P_k(\xi)$ obey the recursion relation:

$$\begin{aligned} P_0(\xi) &= 1 \\ P_1(\xi) &= N - 2\xi \\ P_k(\xi) &= [N - 2\xi]P_{k-1} - (k-1)(N-k+2)P_{k-2}. \end{aligned}$$ (5.14)

They are orthogonal to each other and alternating between even and odd parity. Actually, as the number of spins N approaches the thermodynamic limit, these polynomials converge into the Hermite polynomials. Because $\xi = 0,1,\ldots,N$, we have $N - 2\xi = N, N-1,\ldots,-N$. If we let $N - 2\xi = Nx$, then x goes from 1 to -1 in discrete steps and the recursion relation (5.14) reads:

$$\begin{aligned} P_0(x) &= 1 \\ P_1(x) &= Nx \\ P_k(x) &= NxP_{k-1} - N(k-1)P_{k-2} \end{aligned}$$ (5.15)

with corresponding Rodrigues' formula:

$$P_k(x) = (-1)^k e^{\frac{Nx^2}{2}}\frac{d^k}{dx^k}e^{-\frac{Nx^2}{2}}.$$ (5.16)

Eq. (5.15) is just the scaled version of the standard Hermite polynomials whose Rodrigues' formula is $H_k(x) = (-1)^k e^{x^2}\frac{d^k}{dx^k}e^{-x^2}$. Thus the characteristic polynomials of eigenvectors of $\tilde{H}$ converge into Hermite polynomials if the number of spins approaches the thermodynamic limit. This phenomenon can be understood because Hermite polynomials represent the eigenstates of a quantum harmonic oscillator (QHO) [30]. For an array with finite number of spins, however, the spectrum resembles that of a pseudo-harmonic oscillator with equally spaced eigenvalues and the corresponding eigenvectors (Eq. 5.12) are of the pseudo-Hermite form. One should notice that for QHO the coordinate in eigenvectors is a continuous variable in real space, while the coordinate x in expression (5.15) takes the form of discrete variables in the $(N+1)$-dimensional spin space.
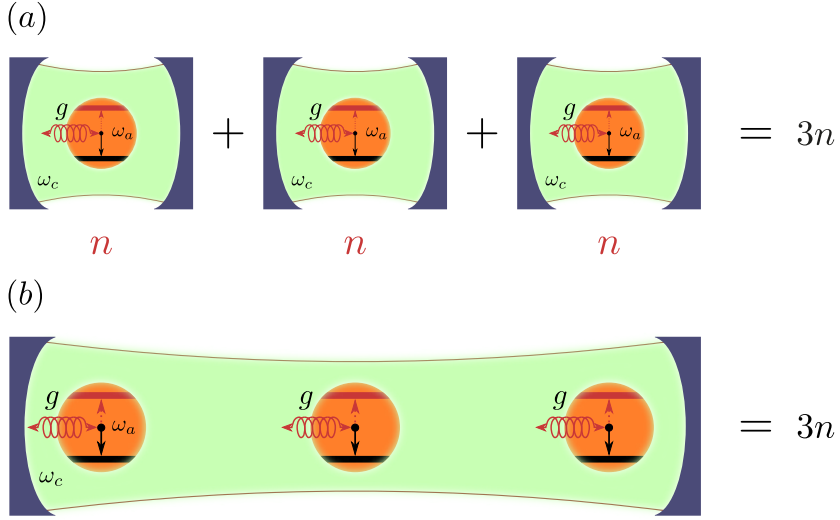
Figure 5.2: (a) Individually charging three spins in a parallel protocol. Each cavity is filled with n photons and in total $3n$ number of photons are used. (b) The three spins are collectively charged inside a single cavity. To make a fair comparison the same amount of photons should be provided as in the parallel protocol.

This could be understood as if the number of spins stays finite, the battery subsystem behaves like a pseudo-harmonic oscillator swinging in quantized energy levels.

Once the form of propagator is known, the time of flipping spins from down to up can be derived by solving the Schrödinger equation. In appendix 5.6 we show that the collective spin dynamics follows a periodic fashion and the duration of flipping all spins from ground to excited state is

$$\tau = \frac{\pi}{2g\sqrt{n}}, \tag{5.17}$$

independent to the number of spins N. However, it is worth mentioning that this periodic evolution of spins is limited to the first-order approximation of the parameter $\epsilon \equiv N/n \ll 1$. The higher order terms diminish in the strong driving field setting [31].

Based on the above analysis, we show that from the aspect of energy transfer there is an enhancement for the charging efficiency in aforementioned charger-battery setup. If the time of flipping N spins equals $\tau = \frac{\pi}{2g\sqrt{n}}$, then the average charging power for collective charging protocol is $\sqrt{N}$ times larger than for the corresponding parallel (individually charging) protocol. Let us set $N = 3$ as an example. The proof can be straight-forwardly extended to arbitrary N spins. First, it is easy to see that the time of flipping three spins in parallel is the same as the time required to flip each spin individually. That is, $\tau_{\text{par}} = \frac{\pi}{2g\sqrt{n}}$ where n denotes the number of driving photons in each cavity (as shown in figure 5.2(a)). Therefore, the total amount of photons for driving 3 spins simultaneously should be summed to be $3n$. In order to make a fair comparison, it is important to make sure that the energy of the charging field in the collective protocol (shown in figure 5.2(b)) equals to the parallel one. That is, in this example the number of photons in collectively charging cavity should set to be $3n$ (instead of n). Thus the time required to flip three spins in a single cavity is given by $\tau_{\text{col}} = \frac{\pi}{2g\sqrt{3n}} = \frac{1}{\sqrt{3}}\tau_{\text{par}}$.

In both protocols, the energy transferred to the 3-spin battery is the same (Eq. 5.4); only the time of charging collectively is $\sqrt{3}$ times faster than the parallel one. As a result, the average charging power for collective protocol is $\sqrt{3}$ times stronger than the corresponding parallel protocol. One can easily extend this result to a N-spin battery as long as the assumption $N \ll n$ is preserved.

5.4. Quantum speed up originating from coherent cooperative interactions

In order to understand the origin of the speedup effect described in previous section, we first calculate the quantum speed limit (QSL) which forms the lower bound of the evolution duration that could possibly be achieved by corresponding Hamiltonian. For the parallel protocol, its energy variance reads $\Delta \tilde{H}_{\mathrm{par}} = N \cdot 2g\sqrt{n}$ and the number of charging photons is nN. According to Refs. [18] and [32], we have the QSL as:

$$\mathfrak{T}_{\mathrm{par}} = \frac{\pi}{2\Delta \tilde{H}_{\mathrm{par}}} = \frac{\pi}{4Ng\sqrt{n}} \tag{5.18}$$

For collective charging, the energy variance for the same number of charging photons is $\Delta \tilde{H}_{\mathrm{col}} = N \cdot 2g\sqrt{nN}$, and the corresponding QSL is:

$$\mathfrak{T}_{\mathrm{col}} = \frac{\pi}{2\Delta \tilde{H}_{\mathrm{col}}} = \frac{\pi}{4Ng\sqrt{nN}} = \frac{1}{\sqrt{N}}\mathfrak{T}_{\mathrm{par}} \tag{5.19}$$

We see that due to the collective effect, the quantum speed limit has also been pushed down by a factor of $\frac{1}{\sqrt{N}}$. This analysis agrees with the discussion in Ref. [33], stating that the speed limit for parallel driving is $\sqrt{N}$ times larger than that for the collective one. Together with the previous result of $\tau_{\mathrm{col}} = \frac{1}{\sqrt{N}}\tau_{\mathrm{par}}$, we conjecture that the coherent cooperative effect among N spins inside the cavity leads to a shortcut of duration by factor $\frac{1}{\sqrt{N}}$ for all time related phenomena.

By taking partial trace of the density matrix of the collectively charged spins, we can calculate and plot the development of entanglement during the evolution. As shown in Fig. 5.3, no entanglement develops during the flipping process. Upon detailed numerical inspection, one finds that all spins process exactly in step, i.e. follow the same evolution. This result differs from the conclusion of Ref. [21], which states that long-range entangling interactions among the spins will be formed due to the mediation of the common photon field inside the cavity. We have thus found an example where it is not the globally entangling operations that lead to the enhancement of charging. This raises the question what is the source of quantum speed-up in our model, if there is no entanglement involved.

To answer this question we symbolically solve the von Neumann equation with Hamiltonian Eq. (5.8):

$$\begin{aligned}
\frac{\mathrm{d}a}{\mathrm{d}t} &= i[H, a] = -i\omega_c a - igS_- \\
\frac{\mathrm{d}\sigma_z^{(j)}}{\mathrm{d}t} &= i[H, \sigma_z^{(j)}] = ig(a^\dagger \sigma_-^{(j)} - a\sigma_+^{(j)}).
\end{aligned} \tag{5.20}$$
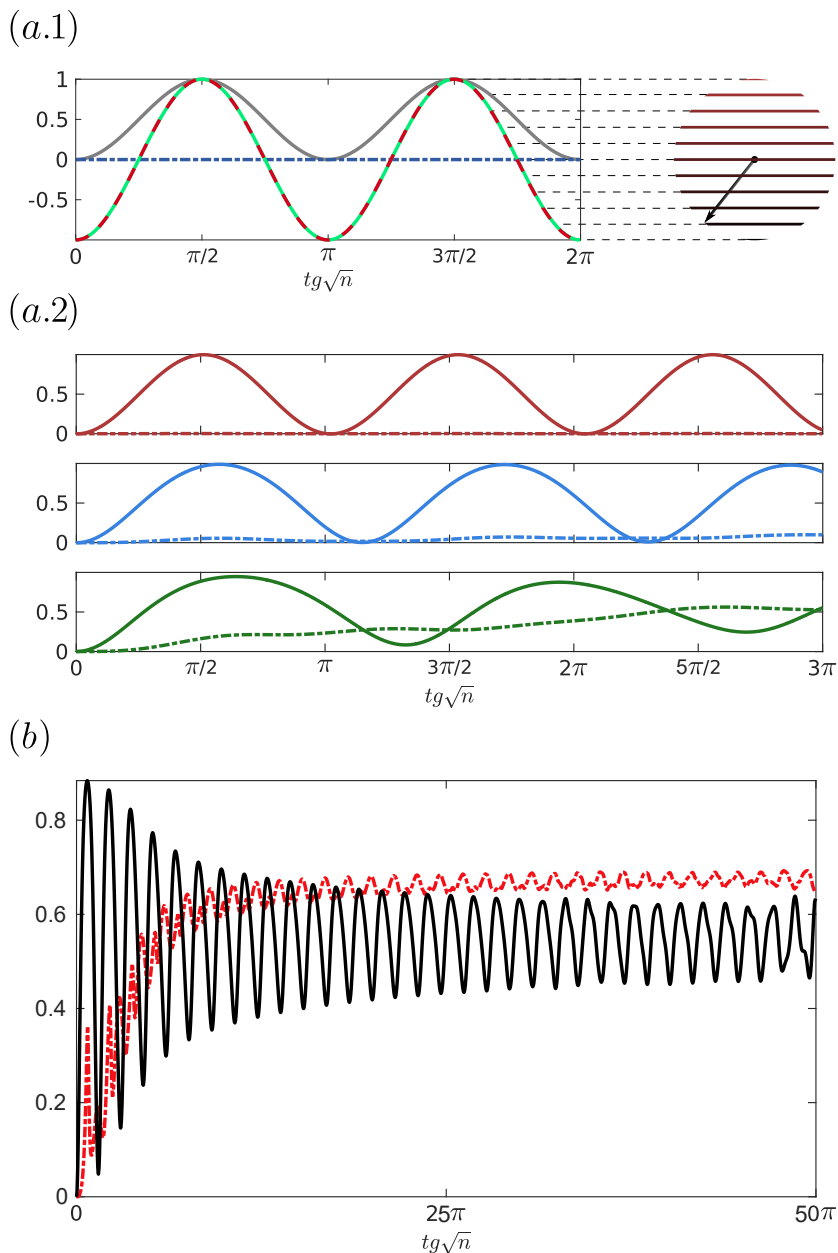
$(a.1)$

$(a.2)$

(b)

Figure 5.3: (a.1) The evolution of 10 spins with 10^4 driving photons under the charging Hamiltonian Eq. (5.8). The gray curve stands for the energy deposited into each battery $\frac{W(t)}{N\omega_a}$ (in dimensionless units), which evolves periodically as the spins are consistently flipped from down to up and vice-versa. We take the Von Neumann entropy of the first spin from reduced density matrix as a measure for the amount of entanglement of the batteries. This indicator (blue dotted line) stays 0 meaning that there is no entanglement being created during the process. The overlapping green and red curves depict the evolution of $\cos\theta_j$, with θ_j the angle between $\langle s_j \rangle$ and the z^+ axis for the jth spin (shown as the right sphere). Here the red curve stands for the first spin, i.e. $j = 1$ and the green one represents for another randomly picked spin out of the batteries. This overlap means all spins in the cavity evolve exactly in step. (a.2) From top to bottom these three subplots indicate the charging of 10 spins with 100, 20, and 12 photons respectively. As before, solid curves refer to the deposited energy on each spin and the dotted line stands for the amount of entanglement. As the number of cavity photons shrinks, entanglement shows up and the spins cannot be fully charged. Such a result suggests that the requirement of $N/n \ll 1$ can be reached as long as the photons outnumber the spins by an order of magnitude. (b) The supplementary plot for the evolution of 100 spins driven by 90 photons. As time progresses, dynamical equilibrium between the photons and spins will be formed as indicated in Ref. [34].

Here $j = 1, 2, \ldots, N$ numbers the spins inside the cavity. Solving the dynamic equation for operator $a(t)$ one finds that:

$$a(t) = -ig \int_{-\infty}^{t} e^{i\omega_c(t'-t)} S_-(t') dt'$$

$$a^\dagger(t) = ig \int_{-\infty}^{t} e^{-i\omega_c(t'-t)} S_+(t') dt'. \tag{5.21}$$

Substituting these expressions back into Eq. (5.20) we obtain the equation of motion for a single spin:

$$\frac{d\sigma_z^{(j)}}{dt} = -g^2 \Big[\sigma_-^{(j)}(t) \int_{-\infty}^{t} e^{-i\omega_c(t'-t)} S_+(t') dt'$$

$$+ \sigma_+^{(j)}(t) \int_{-\infty}^{t} e^{i\omega_c(t'-t)} S_-(t') dt' \Big]. \tag{5.22}$$

Eq. (5.22) shows that by integrating out the photon field, the effective force applied on an arbitrary spin j is proportional to $\int_{-\infty}^{t} e^{i\omega_c(\tau-t)} S_\pm(\tau) d\tau$. We thus see that the interactions between the spins mediated by cavity photons act cooperatively, leading to an evenly distributed enhancement of the driving force on each of the battery spins. Since numerical calculation shows that all spins follow the same evolution in time, we can replace $S_\pm$ in Eq. (5.22) with $S_\pm = \sum_{j=1}^{N} \sigma_\pm^{(j)} = N\sigma_\pm$ leading to the spin dynamics:

$$\frac{d\sigma_z}{dt} = -Ng^2 \Big[\sigma_-(t) \int_{-\infty}^{t} e^{-i\omega_c(t'-t)} \sigma_+(t') dt'$$

$$+ \sigma_+(t) \int_{-\infty}^{t} e^{i\omega_c(t'-t)} \sigma_-(t') dt' \Big]. \tag{5.23}$$

This final form explicitly shows that the coupling strength of each spin has been increased by $\sqrt{N}$. With this in mind, it is easy to understand that all the time-related phenomena that depend linearly on the coupling strength would be accelerated by a factor of $\sqrt{N}$.

As argued by Binder *et al.*, quantum speed up originates from two different sources. One is the reduction of path length between initial and final state in projected Hilbert space following the geodesic curve. Another is the enhanced driving energy felt by each local spin. Focusing on the fact that all spins follow the same evolution as if they are charged individually, we realize that the path length of evolution is the same for both protocols. This means that the collective protocol which does not create entanglement among spins also cannot drive them through the geodesic in projected Hilbert space [35]. This explains that the speed up we observe in this research is $\sqrt{N}$-fold instead of N-fold because the Tavis-Cumming Hamiltonian only increases the energy per spin but does not shorten the length of passage in the projected Hilbert space.

5.5. Summary and conclusion

We have studied the energy transfer efficiency of an ideal Dicke quantum battery within the limit $N/n \ll 1$. Under the constraint of full charging, we predict a $\sqrt{N}$-fold boost of

the charging power for a collective protocol compared to the parallel one. Using the matrix representation of the driving Hamiltonian we have analytically solved the eigenenergies and eigenstates for this charger-battery system. We find that the collective dynamics of spins mimics the process of swinging a pseudo-pendulum in quantized and finite-dimensional energy levels. We then apply these tools to the unitary evolution equation of the spins and demonstrate the existence of a universal flipping time for an arbitrary number of spins. Based on this, we show a boost of the averaged charging power for a collective charging protocol with evenly distributed driving forces.

Contrary to previous studies (see e.g. Refs. [18, 21]) which require multi-particle entanglement as the key part of quantum speed up, in our model there is no entanglement generated for the collective charging protocol. However, it is the coherent cooperative interactions inside the cavity that lead to increased coupling strength for each spin. Such effect results in the lowering of the quantum speed limit by a factor $\frac{1}{\sqrt{N}}$. In conclusion, for our Dicke battery the boost of charging power arises from the enhanced driving forces exerted on each spin, and not from a shortened path length in the projected Hilbert space.

Although the Dicke battery presented here only shows 'half' the amount of speed up (factor $\sqrt{N}$ instead of N), it exhibits a scalable quantum advantage for faster energy transfer. Moreover, by cutting-edge development of cavity spintronics this battery setup is ready to be implemented in practice. For instance, nitrogen-vacancy (NV) centers are well suited for studying spin dynamics. NV spins can be optically implanted, initialized, and read out [36]. As shown in Ref. [37], the implantation of a few NV spins into the L3 photonic crystal cavity for coherent manipulations has already been realized. And the coupling of an ensemble of NV spins to a frequency tunable superconductor resonator has also been reported [38].

Future work could focus on adding entangling interactions between the spins in order to further explore the remaining $\sqrt{N}$ factor of speedup. Another interesting line of research is to include spin decay and the injection of photons, which leads to a non-Hermitian quantum mechanical system [39]. By careful tuning such that the rate of injecting photons matches the decay rate of spins, this system allows for a transition into the regime of parity and time reversal symmetry, i.e. $\mathscr{PT}$ symmetry [40, 41]. Within $\mathscr{PT}$ symmetry, the eigenvalues of the non-Hermitian Hamiltonian become real and several exceptional properties such as the increase of coupling strength and the decrease of the quantum speed limit would be expected [42, 43].

5.6. Appendix: The universal flip duration

Equipped with the eigenvalues (5.11) and eigenvectors (5.12) of $\tilde{H}$, we can now replace the propagator $e^{-i\tilde{H}\tau}$ with $Ve^{-iD\tau}V^\dagger$. Substituting the expression of D and V one finds the integrated Schrödinger equation

$$\begin{pmatrix} 1 \\ 0 \\ \vdots \\ 0 \end{pmatrix} \overset{\tau?}{=\!=\!=} Ve^{-iD\tau}V^\dagger \begin{pmatrix} 0 \\ 0 \\ \vdots \\ 1 \end{pmatrix}. \tag{5.24}$$

can be rephrased into two algebraic equations with even and odd number of spins respectively:

Case I: For odd numbers of spins $N = 2m + 1$, the algebraic equation corresponding to Eq. (5.24) is

$$\sum_{k=0}^{m} \frac{2 \binom{2m+1}{k}}{2^{2m+1}} (-1)^k \sin(2m+1-2k)g\sqrt{n}\tau \stackrel{\tau?}{=\!=} \pm 1. \tag{5.25}$$

One can see that if $\tau = \frac{\pi}{2g\sqrt{n}}$, then

$$(-1)^k \sin(2m+1-2k)g\sqrt{n}\tau = (-1)^m$$

holds such that the left-hand side of (5.25) becomes:

$$(-1)^m \sum_{k=0}^{m} \frac{2 \binom{2m+1}{k}}{2^{2m+1}} = (-1)^m = \pm 1.$$

So in case that N is odd, the flip duration $\tau = \frac{\pi}{2g\sqrt{n}}$.

Case II: For even number of spins $N = 2m$, the algebraic equation corresponding to Eq. (5.24) is given by

$$\sum_{k=0}^{m-1} \frac{2 \binom{2m}{k}}{2^{2m}} (-1)^k \cos(2m-2k)g\sqrt{n}\tau + (-1)^m \frac{\binom{2m}{m}}{2^{2m}} \stackrel{\tau?}{=\!=} \pm 1. \tag{5.26}$$

Similarly as the odd-spin case above, for $\tau = \frac{\pi}{2g\sqrt{n}}$

$$(-1)^k \cos(2m-2k)g\sqrt{n}\tau = (-1)^m$$

holds such that the left-hand side of (5.26) becomes:

$$(-1)^m \sum_{k=0}^{m-1} \frac{2 \binom{2m}{k}}{2^{2m}} + (-1)^m \frac{\binom{2m}{m}}{2^{2m}} = (-1)^m = \pm 1$$

Thus in case that N is even, the flip duration is given by $\tau = \frac{\pi}{2g\sqrt{n}}$.

Thus we conclude that the time required to flip all the spins is $\tau = \frac{\pi}{2g\sqrt{n}}$, independent to the number of spins N. This result is derived based on the Tavis-Cummings charging Hamiltonian, it is valid under the assumption that the number of photons saturates the number of spins [31, 44].

References

[1] X. Zhang and M. Blaauboer, *Enhanced energy transfer in a dicke quantum battery,* arXiv e-prints , 1812.10139 (2018).

[2] A. Crescente, M. Carrega, M. Sassetti, and D. Ferraro, *Charging and energy fluctuations of a driven quantum battery,* New Journal of Physics **22**, 063057 (2020).

[3] F. Caravelli, G. Coulter-De Wit, L. P. García-Pintos, and A. Hamma, *Random quantum batteries,* Phys. Rev. Research **2**, 023095 (2020).

[4] F. Barra, *Dissipative charging of a quantum battery,* Phys. Rev. Lett. **122**, 210601 (2019).

[5] J. Liu, D. Segal, and G. Hanna, *Loss-free excitonic quantum battery,* The Journal of Physical Chemistry C **123**, 18303 (2019).

[6] S. Ghosh, T. Chanda, and A. Sen(De), *Enhancement in the performance of a quantum battery by ordered and disordered interactions,* Phys. Rev. A **101**, 032115 (2020).

[7] R. Alicki and M. Fannes, *Entanglement boost for extractable work from ensembles of quantum batteries,* Phys. Rev. E **87**, 042123 (2013).

[8] J. Goold, M. Huber, A. Riera, L. del Rio, and P. Skrzypczyk, *The role of quantum information in thermodynamics—a topical review,* Journal of Physics A: Mathematical and Theoretical **49**, 143001 (2016).

[9] V. Giovannetti, S. Lloyd, and L. Maccone, *The role of entanglement in dynamical evolution,* Europhys. Lett. **62**, 615 (2003).

[10] A. Borras, C. Zander, A. R. Plastino, M. Casas, and A. Plastino, *Entanglement and the quantum brachistochrone problem,* Europhys. Lett. **81**, 30007 (2008).

[11] E. M. dos Santos and E. I. Duzzioni, *Elucidating dicke superradiance by quantum uncertainty,* Phys. Rev. A **94**, 023819 (2016).

[12] I. Henao and R. M. Serra, *Role of quantum coherence in the thermodynamics of energy transfer,* Phys. Rev. E **97**, 062105 (2018).

[13] G. M. Andolina, D. Farina, A. Mari, V. Pellegrini, V. Giovannetti, and M. Polini, *Charger-mediated energy transfer in exactly solvable models for quantum batteries,* Phys. Rev. B **98**, 205423 (2018).

[14] G. M. Andolina, M. Keck, A. Mari, M. Campisi, V. Giovannetti, and M. Polini, *Extractable work, the role of correlations, and asymptotic freedom in quantum batteries,* Phys. Rev. Lett. **122**, 047702 (2019).

[15] G. M. Andolina, M. Keck, A. Mari, V. Giovannetti, and M. Polini, *Quantum versus classical many-body batteries,* Phys. Rev. B **99**, 205437 (2019).

[16] S. Julià-Farré, T. Salamon, A. Riera, M. N. Bera, and M. Lewenstein, *Bounds on the capacity and power of quantum batteries,* Phys. Rev. Research **2**, 023113 (2020).

[17] X.-M. Zhang, Z.-W. Cui, X. Wang, and M.-H. Yung, *Automatic spin-chain learning to explore the quantum speed limit,* Phys. Rev. A **97**, 052333 (2018).

[18] F. C. Binder, S. Vinjanampathy, K. Modi, and J. Goold, *Quantacell: powerful charging of quantum batteries,* New Journal of Physics **17**, 075015 (2015).

[19] T. P. Le, J. Levinsen, K. Modi, M. M. Parish, and F. A. Pollock, *Spin-chain model of a many-body quantum battery,* Phys. Rev. A **97**, 022106 (2018).

[20] R. H. Dicke, *Coherence in spontaneous radiation processes,* Phys. Rev. **93**, 99 (1954).

[21] D. Ferraro, M. Campisi, G. M. Andolina, V. Pellegrini, and M. Polini, *High-power collective charging of a solid-state quantum battery,* Phys. Rev. Lett. **120**, 117702 (2018).

[22] C. Emary and T. Brandes, *Chaos and the quantum phase transition in the dicke model,* Phys. Rev. E **67**, 066203 (2003).

[23] E. Wolfe and S. F. Yelin, *Certifying separability in symmetric mixed states of n qubits, and superradiance,* Phys. Rev. Lett. **112**, 140402 (2014).

[24] Z. Wang, H. Li, W. Feng, X. Song, C. Song, W. Liu, Q. Guo, X. Zhang, H. Dong, D. Zheng, H. Wang, and D.-W. Wang, *Controllable switching between superradiant and subradiant states in a 10-qubit superconducting circuit,* Phys. Rev. Lett. **124**, 013601 (2020).

[25] O. O. Soykal and M. E. Flatté, *Strong field interactions between a nanomagnet and a photonic cavity,* Phys. Rev. Lett. **104**, 077202 (2010).

[26] T. Holstein and H. Primakoff, *Field dependence of the intrinsic domain magnetization of a ferromagnet,* Phys. Rev. **58**, 1098 (1940).

[27] M. Kozierowski, A. A. Mamedov, and S. M. Chumakov, *Spontaneous emission by a system of n two-level atoms in terms of the su(2)-group representations,* Phys. Rev. A **42**, 1762 (1990).

[28] S. M. Chumakov, A. B. Klimov, and J. J. Sanchez-Mondragon, *General properties of quantum optical systems in a strong-field limit,* Phys. Rev. A **49**, 4972 (1994).

[29] I. Chiorescu, N. Groll, S. Bertaina, T. Mori, and S. Myiashita, *Magnetic strong coupling in a spin-photon system and transition to classical regime,* Phys. Rev. B **82**, 024413 (2010).

[30] R. Shankar, *Principles of Quantum Mechanics* (Springer US, New York, 1994).

[31] M. Kozierowski, S. M. Chumakov, J. Światlowski, and A. A. Mamedov, *Collective collapses and revivals in spontaneous emission of a partially inverted system of two-level atoms: Analytical solution,* Phys. Rev. A **46**, 7220 (1992).

[32] V. Giovannetti, S. Lloyd, and L. Maccone, *Quantum limits to dynamical evolution,* Phys. Rev. A **67**, 052109 (2003).

[33] F. C. Binder, *Work, Heat, and Power of Quantum Processes,* Ph.D. thesis, University of Oxford (2016), section 3.6.

[34] O. O. Soykal and M. E. Flatté, *Size dependence of strong coupling between nanomagnets and photonic cavities,* Phys. Rev. B **82**, 104413 (2010).

5

[35] A. Carlini, A. Hosoya, T. Koike, and Y. Okudaira, *Time-optimal quantum evolution,* Phys. Rev. Lett. **96**, 060503 (2006).

[36] G. de Lange, Z. H. Wang, D. Ristè, V. V. Dobrovitski, and R. Hanson, *Universal dynamical decoupling of a single solid-state spin from a spin bath,* Science **330**, 60 (2010).

[37] T. Schröder, M. Walsh, J. Zheng, S. Mouradian, L. Li, G. Malladi, H. Bakhru, M. Lu, A. Stein, M. Heuck, and D. Englund, *Scalable fabrication of coupled nv center - photonic crystal cavity systems by self-aligned n ion implantation,* Opt. Mater. Express **7**, 1514 (2017).

[38] Y. Kubo, F. R. Ong, P. Bertet, D. Vion, V. Jacques, D. Zheng, A. Dréau, J.-F. Roch, A. Auffeves, F. Jelezko, J. Wrachtrup, M. F. Barthe, P. Bergonzo, and D. Esteve, *Strong coupling of a spin ensemble to a superconducting resonator,* Phys. Rev. Lett. **105**, 140502 (2010).

[39] C. M. Bender, D. C. Brody, and H. F. Jones, *Complex extension of quantum mechanics,* Phys. Rev. Lett. **89**, 270401 (2002).

[40] Y.-L. Liu, R. Wu, J. Zhang, Şahin Kaya Özdemir, L. Yang, F. Nori, and Y.-X. Liu, *Controllable optical response by modifying the gain and loss of a mechanical resonator and cavity mode in an optomechanical system,* Phys. Rev. A **95**, 013843 (2017).

[41] C. M. Bender and S. Boettcher, *Real spectra in non-hermitian hamiltonians having PT symmetry,* Phys. Rev. Lett. **80**, 5243 (1998).

[42] D. Zhang, X.-Q. Luo, Y.-P. Wang, T.-F. Li, and J. Q. You, *Observation of the exceptional point in cavity magnon-polaritons,* Nature Communications **8**, 1368 (2017).

[43] C. M. Bender, D. C. Brody, H. F. Jones, and B. K. Meister, *Faster than hermitian quantum mechanics,* Phys. Rev. Lett. **98**, 040403 (2007).

[44] B. Yao, Y. S. Gui, J. W. Rao, S. Kaur, X. S. Chen, W. Lu, Y. Xiao, H. Guo, K. P. Marzlin, and C. M. Hu, *Cooperative polariton dynamics in feedback-coupled cavities,* Nature Communications **8**, 1 (2017).

5

Curriculum Vitæ

Xiang ZHANG

21-11-1987   Born in Jiangxi, China.

Education

2004–2008   B.Sc. in Nuclear Engineering
Harbin Engineering University, Harbin, China

2008–2011   M.Sc. in Nuclear Science and Technology
Thesis: *Temperature dependent nuclear data interpolation*
Tsinghua University, Beijing, China

2013-2015   M.Sc. in Theoretical Physics
Thesis: *Minimal output entropy for a fermionic Gaussian system*
Katholieke Universiteit Leuven, Leuven, Belgium

2016–2021   Ph.D. in Theoretical Physics
Thesis: *To be defined*
Delft University of Technology, Delft, Netherlands
Promoter: Prof. Yaroslav Blanter
Co-promoter: Dr. Miriam Blaauboer

Awards

2015   Cum Laude

List of Publications

5. **X. Zhang**, G. E. W. Bauer, and T. Yu. *Unidirectional Pumping of Phonons by Magnetization Dynamics.* Phys. Rev. Lett. **125**, 077203 (2020).

4. T. Yu, **X. Zhang**, S. Sharma, Y. M. Blanter, and G. E. W. Bauer. *Chiral coupling of magnons in waveguides.* Phys. Rev. B **101**, 094414 (2020).

3. T. Yu, Y. X. Zhang, S. Sharma, **X. Zhang**, Y. M. Blanter, and G. E. W. Bauer. *Magnon Accumulation in Chirally Coupled Magnets.* Phys. Rev. Lett. **124**, 107202 (2020).

2. B. Yao, T. Yu, **X. Zhang**, W. Lu, Y. Gui, C. M. Hu, and Y. M. Blanter. *The microscopic origin of magnon-photon level attraction by traveling waves: Theory and experiment.* Phys. Rev. B **100**, 214426 (2019).

1. **X. Zhang** and M. Blaauboer. *Enhanced energy transfer in a Dicke quantum battery.* arXiv: 1812.10139.